

ALMA MATER STUDIORUM UNIVERSITÀ DI BOLOGNA

---

---

FACOLTÀ DI SCIENZE MATEMATICHE FISICHE E NATURALI  
DOTTORATO DI RICERCA IN FISICA, XXII CICLO  
SETTORE SCIENTIFICO-DISCIPLINARE DI AFFERENZA: FIS/04

Tesi di dottorato

**The topological trigger system of the  
TOF detector for the ALICE experiment  
at the LHC**

DR. ALESSANDRO SILENZI

Relatore:

Chiar.mo Prof.

**Maurizio Basile**

Coordinatore:

Chiar.mo Prof.

**Fabio Ortolani**

---

---

Bologna, Italy, 2010



ALMA MATER STUDIORUM UNIVERSITÀ DI BOLOGNA

---

FACOLTÀ DI SCIENZE MATEMATICHE FISICHE E NATURALI  
DOTTORATO DI RICERCA IN FISICA, XXII CICLO  
SETTORE SCIENTIFICO-DISCIPLINARE DI AFFERENZA: FIS/04

Tesi di dottorato

**The topological trigger system of the  
TOF detector for the ALICE experiment  
at the LHC**

**Dr. Alessandro Silenzi**

Relatore:

Chiar.mo Prof.

**Maurizio Basile**

Coordinatore:

Chiar.mo Prof.

**Fabio Ortolani**

**Keywords:** ALICE, TOF, PID, Trigger, FEE

---

Bologna, Italy, 2010



*I suppose it is tempting, if the only tool  
you have is a hammer, to treat  
everything as if it were a nail.*

*Abraham Maslow*



# Contents

<b>Preface</b>	<b>1</b>
<b>1 Relativistic Heavy Ion Physics</b>	<b>3</b>
1.1 Quantum Chromodynamics . . . . .	3
1.1.1 Chiral Symmetry . . . . .	4
1.1.2 Confinement and Asymptotic Freedom . . . . .	5
1.2 QCD boiling point . . . . .	6
1.2.1 QCD phase diagram . . . . .	6
1.2.2 QGP dynamics . . . . .	8
1.2.3 Lattice QCD calculations . . . . .	10
1.3 Experimental Observables for ALICE . . . . .	14
1.3.1 Kinematic Probes and chemical probes . . . . .	15
1.3.2 Jets . . . . .	23
1.3.3 Photons . . . . .	24
1.3.4 Dileptons . . . . .	25
1.3.5 Heavy quarks and quarkonia . . . . .	26
1.3.6 Proton-proton physics . . . . .	26
1.4 Results from the SPS . . . . .	28
1.5 Recent results and open issues from RHIC . . . . .	32
1.5.1 Energy density and multiplicity measurements . . . . .	32
1.5.2 Thermalization . . . . .	33
1.5.3 Binary scaling and high $p_T$ suppression . . . . .	33
1.5.4 Hadron production . . . . .	38
1.5.5 Open issues and needs from future experiments . . . . .	41
<b>2 ALICE experiment</b>	<b>43</b>
2.1 The experimental design . . . . .	43
2.2 ALICE setup . . . . .	46
2.2.1 Magnet . . . . .	46
2.3 mid-rapidity Tracking System . . . . .	47

2.3.1	Inner Tracking System . . . . .	47
2.3.2	Time Projection Chamber . . . . .	49
2.3.3	TPC design considerations . . . . .	49
2.4	Particle identification system . . . . .	51
2.4.1	Transition-Radiation Detector (TRD) . . . . .	51
2.4.2	Time-Of-Flight Detector (TOF) . . . . .	52
2.4.3	High-Momentum Particle Identification (HMPID) . . . . .	52
2.4.4	Photon Spectrometer (PHOS) . . . . .	53
2.4.5	Electromagnetic Calorimeter (EMCal) . . . . .	54
2.4.6	Forward Muon Spectrometer . . . . .	54
2.4.7	Forward rapidity detectors . . . . .	55
2.5	Trigger and Data acquisition . . . . .	56
2.5.1	Trigger system . . . . .	56
2.5.2	Data Acquisition (DAQ) System . . . . .	58
2.5.3	High-Level Trigger (HLT) . . . . .	58
2.6	LHC Machine complex . . . . .	58
2.6.1	Luminosity determination . . . . .	60
2.6.2	ALICE luminosity constraints . . . . .	60
2.7	Radiation damage . . . . .	61
<b>3</b>	<b>The Time-Of-Flight Detector</b>	<b>63</b>
3.1	Time-Of-Flight technique . . . . .	63
3.2	The Detector . . . . .	64
3.2.1	Time signal from an RPC . . . . .	66
3.2.2	The Multigap RPC technology . . . . .	66
3.2.3	MRPC Efficiency and resolution . . . . .	73
3.3	Front-end electronics . . . . .	74
3.4	Readout electronics . . . . .	77
3.4.1	TRM . . . . .	77
3.4.2	CPDM . . . . .	81
3.4.3	LTM . . . . .	81
3.4.4	DRM . . . . .	82
3.5	Auxiliary Control System . . . . .	83
3.6	Clock and TTC system . . . . .	85
3.6.1	Clock and TTC distribution schema . . . . .	85
3.6.2	Measurement procedure . . . . .	87
3.6.3	Calibration of the patch cords length . . . . .	89
3.6.4	Reference crates measurement . . . . .	89
3.7	Uncertainty sources in TOF measurement . . . . .	92

3.8	Trigger system . . . . .	93
3.8.1	Trigger electronics . . . . .	93
<b>4</b>	<b>Physics Trigger capabilities of the TOF detector</b>	<b>101</b>
4.1	TOF trigger for cosmic rays . . . . .	101
4.1.1	Noise estimation . . . . .	102
4.1.2	Main trigger for the 2009 cosmic run . . . . .	106
4.1.3	Cosmic Rays Physics trigger . . . . .	107
4.1.4	2009 Cosmic Run Statistics . . . . .	108
4.1.5	Results . . . . .	108
4.2	Trigger latency tuning with beam dump . . . . .	111
4.3	Ultra peripheral collisions . . . . .	112
4.4	$pp$ Minimum bias . . . . .	114
4.5	Jet trigger study . . . . .	115
4.5.1	Topological jet selection . . . . .	117
4.5.2	Multiplicity jet selection . . . . .	118
	<b>Conclusions</b>	<b>119</b>
	<b>Bibliography</b>	<b>121</b>



# Preface

High energy physics is the most systematic effort ever done to find the Universe **fundamental building blocks** and acquire knowledge about their **interactions**. The recently started research program of the Large Hadron Collider (LHC) aims both the issues of the field.

Four detectors/experiments have been built to measure the particle outcome of the collision in the LHC: ATLAS<sup>1</sup>, LHCb<sup>2</sup>, CMS<sup>3</sup> and ALICE<sup>4</sup>. The first goal of the LHC is to find the missing building block of the Standard Model: the Higgs scalar boson, that was postulated, and up to now lacks of experimental evidence.

The further goals of the LHC is to explore the TeV energy scale looking for evidences of supersymmetrical particles, extra-dimensions and dark matter particles.

Besides the explorative goals, the LHC physics program will investigate the two open issues in the Standard Model: the CP violation of the electro-weak interaction and the behavior of a state of nuclear matter called Quark Gluon Plasma (QGP).

The QGP is a highly dense and hot state where the constituents of the nucleons are free to move out of the QCD<sup>5</sup> confinement. The ALICE experiment has been designed to cope with the experimental conditions and observables of a QGP reaction. One of the main assets of the ALICE experiment with respect to the other LHC experiments is the particle identification. The large Time-Of-Flight (TOF) detector is the main particle identification detector of the ALICE experiment. The overall time resolution better than 80 ps allows the particle identification over a large momentum range (up to 2.5 GeV/c for  $\pi$ /K and 4 GeV/c for K/p). The TOF makes use of the Multi-gap Resistive Plate Chamber (MRPC), a detector with high efficiency, fast response and intrinsic time resolution better than 40 ps. Quite impressively, this per-

---

<sup>1</sup>ATLAS: A Toroidal LHC Apparatus.

<sup>2</sup>LHCb: LHC beauty.

<sup>3</sup>CMS: Compact Muon Solenoid

<sup>4</sup> A Large Ion Collider Experiment. The four main experiments of the LHC project are here listed in the anti-clockwise direction along the LHC. There are two small experiments: LHCf, devoted to the study of observables related to astroparticle physics and TOTEM that will measure the total cross section.

<sup>5</sup>QCD: Quantum Chromo-Dynamics, the gauge theory of the color interaction between quarks and gluons.

forming detector is made out of rather cheap materials: honeycomb plates, printed circuit boards, glass, paint and fishing line.

Profiting the fast response of the MRPC detector the TOF embeds a highly segmented trigger system that already provided a topologic event selection in the 2009 cosmic run.

This thesis work, developed with ALICE-TOF Bologna group, is organized in four chapters,

**Chapter 1** describes the theoretical framework of the relativistic heavy-ion physics, the description of the QGP formation and a subset of the experimental observables measured in the previous heavy-ion-physics experiments.

**Chapter 2** introduces the ALICE experiment and its detectors. In this chapter, the technical requirements of a heavy-ion experiment at the energy scale of LHC will be emphasized.

**Chapter 3** describes the Time-Of-Flight detector, detailing its components with special attention to the trigger hardware and auxiliary control system, since large part of the Ph.D. work has been devoted to the implementation of these systems.

**Chapter 4** describes the results obtained through the use of the TOF trigger in the 2009 cosmic run, the noise rate expected and the control system used. In this final chapter the capabilities of the TOF trigger system are presented in various event classes for  $pp$  and PbPb collisions using several event selection algorithms.

# Chapter 1

## Relativistic Heavy Ion Physics

The well-established Standard Model is a major success of human understanding of nature. The predictions derived from this model have been put under test for years with success. Amongst these predictions, the long-searched state of nuclear matter called Quark-Gluon Plasma (QGP) has been under study from long time in heavy ion physics. This state of matter, foreseen by the Quantum Chromodynamics (QCD), is a state of asymptotically free particles as energy density tends to infinity. The ordinary state of hadronic matter is bound in mesons and baryons, so there should be a point or a region in the phase space where the state changes from bound to plasma.

Big Bang Cosmology predicts that in the first instants of the universe ( $10^{-5}s$ ) a dense, quickly expanding QGP condensed in the ordinary matter. The study of heavy ion collisions is also the only tool to exploit an elementary particle system phase transition. In this chapter, a theoretical outlook for this research will be addressed.

### 1.1 Quantum Chromodynamics

Quantum Chromo-Dynamics is the gauge theory describing color interactions between quarks and gluons. It constitutes a fundamental theory within the Standard Model  $U(1)_Y \times SU(2)_L \times SU(3)_C$ , responsible for the  $SU(3)_C$  portion.

The theory states that a quark holds a color of threefold variety, therefore an “up” quark is presented as a color triplet  $(u_r, u_g, u_b)$  interacting with eight bosonic fields corresponding to the eight Gell–Mann generators of  $SU(3)_C$  group. Since its formulation, a large body of experimental evidence of QCD has been collected. This brought attention to the two fundamental properties of QCD: confinement and asymptotic freedom.

As the Electro-weak forces reconnects with Coulomb’s law at low momentum trans-

fer, the QCD should reconnect with nuclear forces, a promising approach to this theoretical issue is Chiral Perturbation Theory.

### 1.1.1 Chiral Symmetry

The Standard Model associates the breaking of an internal symmetry of nature at low energy with the attribution of masses. In the  $m_q \rightarrow 0$  approximation, QCD has a symmetry:

$$\mathcal{L}_{(m_q \rightarrow 0)} = -\frac{1}{4}G^{\mu\nu}G_{\mu\nu} + i\bar{q}_L \not{D}q_L + i\bar{q}_R \not{D}q_R \quad (1.1)$$

Where  $G$  is the gluon tensor and  $q$  is the flavor multiplet of quark fields,  $R$  and  $L$  indicates the right-handed or left-handed component. This Lagrangian density is symmetric for the group:

$$U(1)_V \times U(1)_A \times SU(N_f)_L \times SU(N_f)_R \times SU(3)_C \quad (1.2)$$

with  $U(1)_V$  vector baryon number conservation symmetry,  $U(1)_A$  is the axial counterpart of  $U(1)_V$ , and  $SU(N_f)_L \times SU(N_f)_R$  are chiral symmetry groups for flavors and  $SU(3)_C$  is the gauge symmetry of the QCD. This symmetry is spontaneously broken into the flavor symmetry group  $SU(N_f)$  by quark masses; The chiral symmetry breaking originates  $(N_f^2 - 1)$  Goldstone bosons, i.e. the pion triplet in the  $N_f = 2$  case.

The spontaneous symmetry breaking of chiral symmetry is related to the existence of a non-zero expectation value for the vacuum of the axial symmetry ( $\langle Q_A|0\rangle \neq 0$ ). It is useful to define a chiral condensate as:

$$\langle \bar{q}(x)q(x) \rangle = \lim_{\epsilon \rightarrow 0} \langle \bar{q}(x^0 + \epsilon, \vec{x})q(x^0, \vec{x}) \rangle = -\lim_{\epsilon \rightarrow 0} \langle \mathcal{T} \bar{q}(x^0, \vec{x})q(x^0 + \epsilon, \vec{x}) \rangle = -G(x, x^+) \quad (1.3)$$

where  $q$  is the quark field,  $G$  is the propagator of the quark from  $x^0$  to  $x^0 + \epsilon$  and  $\mathcal{T}$  is the time-order product. The connection between spontaneous chiral symmetry breaking and non-vanishing chiral condensate can be highlighted by introducing a pseudoscalar operator  $P(x) \equiv \bar{q}(x)\gamma_5 q(x)$  and calculating the (equal time) commutator with the axial charge  $[Q_A, P] = -\bar{q}(x)q(x)$  at the ground state, holds the relation that if  $\langle Q_A|0\rangle \neq 0$  then  $\langle \bar{q}(x)q(x) \rangle \neq 0$ .

The pseudo-scalar operator  $P$  applied to the vacuum state returns a pion (massless Goldstone pseudoscalar boson  $P|0\rangle = |\pi\rangle$ ). This equation can be used to explicit a relation between the decay constant for the pion and the chiral condensate.

$$\langle 0|A^\mu|\pi\rangle = ip^\mu f e^{-ip \cdot x} \quad (1.4)$$

where  $f = 92 \text{ MeV}$  is the pion decay constant in the chiral limit,  $A^\mu$  is the axial current. the connection between quark masses and pions masses can be addressed

with the GOR ( Gell-Mann, Oakes and Renner) relation:

$$m_\pi^2 f^2 = -(m_u + m_d) \langle \bar{q}q \rangle \quad (1.5)$$

from this relation one derives the chiral condensate expectation value  $\langle \bar{q}q \rangle = -(240 \text{ MeV})^3$ . This condensate is a measure of spontaneous chiral symmetry breaking. The non-zero pion mass reflects the explicit symmetry breaking by the small quark masses. The chiral symmetry is broken at low temperature (for the ordinary hadronic matter) but is expected to be restored in the high temperature regime created in heavy-ion collisions.

### 1.1.2 Confinement and Asymptotic Freedom

Confinement is the term employed to define the experimental observation that quarks and gluons are observable only as colorless baryons ( $qqq$ ) and mesons ( $q\bar{q}$ ). The QCD explanation is that the non-abelian nature of  $SU(3)_C$  originates a dependence to the momentum transferred  $Q^2$  of the coupling constant.

$$\alpha_S(Q^2) \approx \frac{12\pi}{(33 - 2n_f) \ln(\frac{Q^2}{\Lambda_{QCD}^2})} \quad (1.6)$$

where  $Q$  is the 4-momentum transferred,  $n_f$  is the number of flavors and  $\Lambda_{QCD}$  is the QCD energy scale ( $\simeq 200 \text{ MeV}$ ).

It is possible to consider the coupling constant  $\alpha_S$  in two intervals:

$\alpha_S \ll 1$  for large values of  $Q$ , so *quarks* and gluons are weakly coupled, the asymptotic freedom terminology derives from this equation:

$$\lim_{Q^2 \rightarrow \infty} \alpha_S = 0 \quad (1.7)$$

$\alpha_S \simeq 1$  for small values of  $Q$  it is possible to write a potential for a  $q\bar{q}$  pair as

$$V_{q\bar{q}}(r) \sim \sigma r \quad \text{con} \quad \sigma \simeq (425 \text{ MeV})^2 \quad (1.8)$$

taking into account the energy of the bound  $q\bar{q}$  system, it is possible to simplify the picture stating that the system of quarks separated at a  $1 \text{ fm}$  have enough energy to create a new  $q\bar{q}$  pair. The  $\alpha_S > 1$  don't allow a perturbative approach to QCD.

QCD asymptotic freedom is a phenomenological aspect derived by the non-abelian nature of color interaction; confinement is an aspect depending on both

the non-abelian nature of QCD and the masses of quarks. Top quarks are heavy enough ( $m_t \sim 170 \text{ GeV}$ ) to have  $\alpha_S(300 \text{ GeV}^2) \simeq 6 \cdot 10^{-2}$ , therefore are not confined.

The relativistic heavy ion physics program is to explore the properties of nuclear matter in complex and dynamically evolving systems of finite size and under extreme conditions of density and temperature. Even prior to the identification of quantum chromodynamics (QCD) as the underlying theory of strong interactions, it was suggested that new phases of nuclear matter could arise in high density and/or temperature domains. When QCD became the correct theory of strong interactions, it was argued that quarks and gluons would be deconfined under such conditions and moreover that QCD implies a phase transition that is accessible to experimental evidence at an energy density superior to the predicted threshold for QGP creation.

## 1.2 QCD boiling point

The search for experimental evidences of the creation of a deconfined phase is strictly connected to a theoretical issue: what is the nature of the transition between the confined and deconfined state? The answer to this question is strictly related to the predictions for the observables in a QGP creation experiment. If QCD at high temperature experiences a phase transition then a discontinuity in the observables should emerge.

### 1.2.1 QCD phase diagram

The methods of statistical mechanics applied to QCD systems are the tool used to search an equation of state for nuclear matter in the extreme conditions. From the graph in figure 1.1, it is possible to consider that a transition toward QGP can be achieved raising both temperature and the density.

The state of nuclear matter can be plotted as the QCD phase diagram in Fig. 1.1 as a function of the temperature  $T$  and of the chemical potential  $\mu_B$ <sup>1</sup>. The phase diagram shows the course in  $T$  and  $\mu_B$  taken in the last 30 years from the ordinary hadronic matter to the perfect fluid discovered at the Relativistic Heavy Ion Collider (RHIC). Lattice QCD calculations at non-zero chemical potential suggest the existence of a tri-critical point  $(\mu_{B,c}, T_c)$ , such that the transition<sup>2</sup> is no longer

<sup>1</sup> In thermodynamics the chemical potential  $\mu$  measures the amount of change of the system internal energy  $U$  after introducing an additional particle

$$\mu = \frac{\partial U}{\partial N}$$

The baryo-chemical potential  $\mu_B$  is the chemical potential for one baryon.

<sup>2</sup> A phase transition is classified according to the discontinuity of the free energy  $F$  as a function

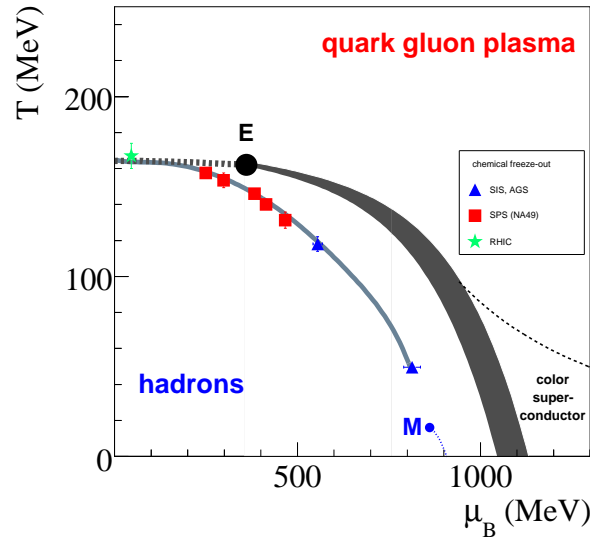


Figure 1.1: The phase diagram for hadronic matter as a function of  $\mu_B$  and  $T$ . Ordinary nuclear matter, QGP and Superconducting color condensate are plotted.

first-order for  $\mu_B < \mu_{B,c}$  and  $T > T_C$ . However, such a critical point is foreseen to be at baryon densities well above those obtained in heavy-ion collisions at the RHIC. The nature of the transition for low values of the baryo-chemical potential depends dramatically on the number of quark flavors and on the light quark masses, especially on the  $s$  mass. It is still unclear whether the transition shows discontinuities for realistic values of the light quark masses, or whether it is a crossover. Recent calculations [Fod04, Eji04] indicate that the transition is a crossover for values of  $\mu_B \leq 400$  MeV.

At low temperatures and high values of the chemical potential, nuclear matter consists of an interacting and degenerate highly compressed Fermi gas of quarks. The interaction among the quarks can be attractive in specific combinations of colors states, leading to the formation of quark-quark pairs which determine a color superconducting phase.

In the early universe, the transition from QGP to hadrons occurred at vanishing chemical potential and high temperatures during the rapid expansion and cooling; on the other hand, in the neutron stars the QGP state is supposed to be formed

---

of the temperature  $T$ . The free energy is defined as follows:

$$F = U - TS$$

where  $U$  is the internal energy and  $S$  is the entropy of the thermodynamical system. A  $n$ -th order phase transition implies that  $\partial^n F / \partial T^n$  is discontinuous while  $\partial^{n'} F / \partial T^{n'}$  with  $n' < n$  is continuous.

for high values of the baryo-chemical potential and temperature close to zero, due to gravitational collapse. In both cases the deconfined phase of hadronic matter appears to play a crucial role. It is this region of high  $T$  and low  $\mu_B$  to be investigated with relativistic heavy-ion collisions.

## 1.2.2 QGP dynamics

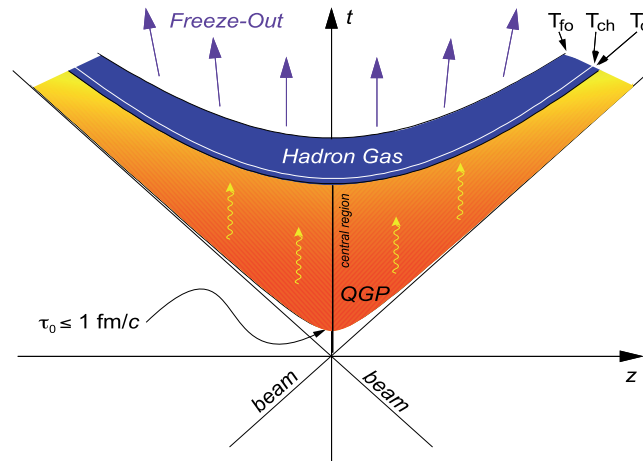


Figure 1.2: A graphic rendition of a AA collision in  $z$  and  $t$ .  $T_C$ ,  $T_{fo}$  and  $T_{ch}$  are the critical, freeze-out and chemical freeze-out temperatures respectively.

### QGP evolution

The evolution in time of a high-energy heavy-ion collision as pictured in Fig. 1.2 can be summarized as follows:

1. the two Lorentz-contracted nuclei collide: matter in an ultra-relativistic nucleus is believed to behave as a Color Glass Condensate [McL01];
2. pre-equilibrium ( $t < 1\text{fm}/c$ ): partons scatter among each other and give rise to an abundant production of deconfined quarks and gluons;
3. thermalization and QGP: ( $t \in [1, 10] \text{fm}/c$ ): matter reaches equilibrium, QGP forms: the degrees of freedom here are those of quarks and gluons;
4. mixed phase: the system, while expanding, begins to convert into a hadron gas;

5. hadronization: ( $t \sim 20$  fm/c): quarks and gluons are again confined into hadrons;
6. chemical freeze-out: inelastic interactions between hadrons cease, relative abundances are fixed;
7. thermal freeze-out: elastic interactions between hadrons cease, kinematical spectra are fixed.

### Past experiments

The determination of the energy density reached in the stages mentioned above is not straightforward; the most used definition was given by Bjorken in 1983[Bjo83]:

$$\epsilon = \frac{1}{Ac\tau_F} \frac{dE_T}{dy} \quad (1.9)$$

where  $A$  is the transverse area of the interaction region,  $dE_T/dy$  is the transverse energy per rapidity unit at mid-rapidity (i.e. an experimentally accessible quantity) and  $\tau_F$  is the formation time of secondary particles. Such formula gives an estimate for the energy density in a central Au-Au collision at  $\sqrt{s} = 200$  GeV per nucleon of about  $15 \text{ GeV}/\text{fm}^3$ . It has to be pointed out that this value refers to the the initial energy density, i.e. the one available when secondary particles are formed but matter is not thermalized. A more relevant quantity for the purposes of studying QGP is obtained by inserting in Eq. 1.9 a realistic guess for the thermalization time instead of  $\tau_F$ , i.e.  $\tau_{Therm} \sim 1$  fm/c. This leads to an energy density of about  $5 \text{ GeV}/\text{fm}^3$  still larger than the critical energy density of  $1 \text{ GeV}/\text{fm}^3$  ( in the relativistic equation of state  $\epsilon \approx 1 \text{ GeV}/\text{fm}^3$  corresponds to  $T = 170$  MeV). The above considerations represent a simplified picture of how the transition to QGP can be realized in a laboratory; however these calculations are meant just to show the possibility of realizing QGP in laboratory. In the past 30 years other experiments has been performed on heavy ion collisions with much lower energies than  $\sqrt{s_{NN}} \simeq 5.5$  TeV of ALICE. The first experiment aimed to the search of a deconfined phase was performed at BEVALAC (1975-1985), the Berkeley University ion accelerator using beams of Nb at  $\sqrt{s_{NN}} \simeq 0.2$  GeV The next target experiments are dated 1986 at the AGS (Alternating Gradient Synchrotron) Brookhaven National Laboratory (BNL)  $\sqrt{s_{NN}} \simeq 5$  GeV with beams of  $^{28}\text{Si}$  and at SPS (Super Proton Synchrotron )at CERN, with  $^{16}\text{O}$  and  $^{32}\text{S}$  beams at  $\sqrt{s_{NN}} \simeq 20$  GeV. A second generation of experiments has been developed starting from 1993-1994 at AGS ( $^{197}\text{Au}$  at  $\sqrt{s_{NN}} \simeq 4.6$  GeV) and at SPS ( $^{208}\text{Pb}$  at  $\sqrt{s_{NN}} \simeq 17.2$  GeV). In the year 2000 BNL built a dedicated Collider: the Relativistic Heavy-Ion Collider (RHIC), that allowed a boost in the energy available for the interaction. This hosts four experiments (BRAHMS,

PHENIX, PHOBOS and STAR) studying Au-Au collisions at  $\sqrt{s_{NN}} \simeq 200$  GeV. A collective paper published by these four collaborations suggests that the original conception of the QGP as a non-interacting gas of gluons and quarks should be dropped; the attainment of thermalization in the very short timescale of the collision highlights the entity of the interactions among the constituents since the earliest stages of the collision. Some authors suggest to re-label quark gluon plasma as “strongly interacting QGP” sQGP or “quark gluon colored world” QGCW. The original name QGP will be used in this thesis as its use is wide spread in literature.

Table 1.1: Comparison of characteristic AA collision parameters at SPS, RHIC and LHC(prediction).

	Parameter	SPS	RHIC	LHC
$\sqrt{s_{NN}}$ (GeV)		17	200	5500
$\tau_0^{QGP}$ (fm/c)	Thermalization time	1	0.2	0.1
T/ $T_C$	Reaction Temperature / $T_C$	1.1	1.9	3.0 – 4.2
$\epsilon$ (GeV/fm <sup>3</sup> )	Energy density	3	5	15 – 60
$\tau_{QGP}$ (fm/c)	QGP life time	$\leq 2$	2 – 4	$\geq 10$
$\tau_{fo}$ (fm/c)	<i>freeze-out</i> time	$\sim 10$	20 – 30	30 – 40
$V_{fo}$ (fm <sup>3</sup> )	<i>freeze-out</i> Volume	$\sim 10^3$	$\sim 10^4$	$\sim 10^5$

### 1.2.3 Lattice QCD calculations

Relatively simple models (e.g. the MIT Bag Model) provide qualitative arguments to identify both the critical temperature  $T_C \sim 170$  MeV and the critical energy density  $\epsilon_C \sim 1$  GeVfm<sup>-3</sup>. It is however necessary to study the phases of quark matter using QCD, as it is generally considered to be the correct theory for interactions of quarks and gluons. Furthermore, equilibrium and phase transitions involve quarks and gluons interacting over a large distance, implying the use of non-perturbative physics. Lattice QCD aims to calculate nuclear matter conditions using a space-time lattice approximation. The main results of this field of theoretical physics are summarized here.

**Critical Temperature:** the predicted transition between hadronic matter and a QGP phase occurs at a temperature of  $T_c = 175 \pm 15$  MeV for  $\mu_B = 0$ .

The precise value of the transition temperature depends on the treatment of quarks in the calculation. The influence of a non-zero chemical potential has also been studied and it has been found that the effect is small for the values of  $\mu_B$  observed at RHIC ( $\mu_B \sim 50$  MeV) and will be even smaller at the LHC energies.

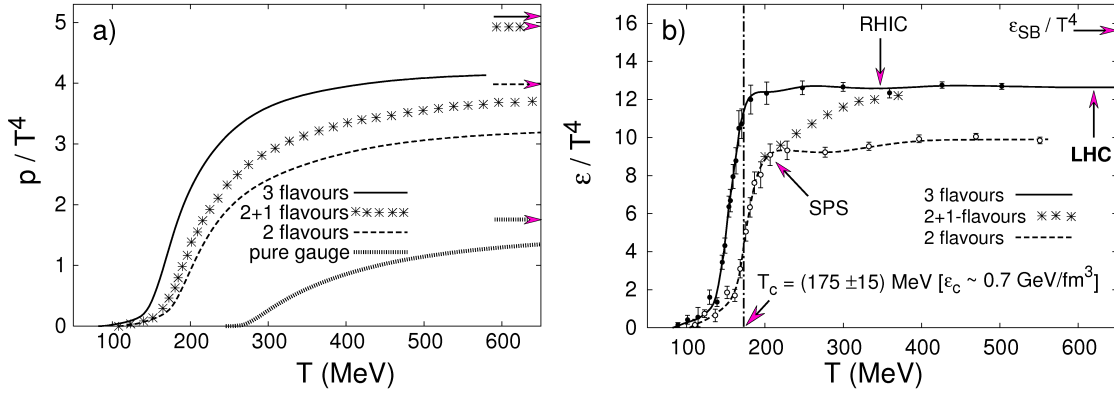


Figure 1.3: Pressure and energy density as a function of temperature

**Non-Ideal phase:** the transition is of second order in the limit of 2-flavor QCD (two quarks with zero masses) and of first order for 3-flavor QCD (three quarks with zero masses). More realistic calculations, incorporating the s quark mass, indicate that the transition is most likely of the crossover type at zero chemical potential. This is reflected for example in the behavior of the energy density  $\epsilon$  as a function of the temperature  $T_c$  shown in Fig.1.3(b); it can be seen that the transition is not of first order because this would indicate a discontinuity of  $\epsilon$  at the critical temperature  $T_c$ . Lattice calculations have intrinsic systematic errors due to the use of a finite lattice cutoff and to the use of quark masses which are eventually infinite (“quenched QCD”). The crossover occurs in a small range of temperatures, thus the “phase transition” will still exhibit as a sudden modification in the observables e.g. a rapid rise of the energy density  $\epsilon$  in the temperature interval of only about 20 MeV. The critical energy density estimated in the 2-flavor QCD picture is  $\epsilon_C \simeq 0.3 \div 1.3$  GeVfm<sup>-3</sup>. In the limit of massless non-interacting particles, each bosonic degree of freedom contributes  $\pi^2/30 T^4$  to the energy density; each fermionic degree of freedom contributes 7/8 of this value. The corresponding Stefan-Boltzmann limit of the energy density  $\epsilon_{SB}$  for the case of 2-flavor QGP is then:

$$\epsilon_{SB} = \left[ \underbrace{2_f \cdot 2_s \cdot 2_q \cdot 3_c \cdot \frac{7}{8}}_{quarks} + \underbrace{2_s \cdot 8_c}_{gluons} \right] \frac{\pi^2}{30} T^4 = \frac{37\pi^2}{30} T^4 \quad (1.10)$$

considering the flavor, spin, quark/antiquark and color contributions for quarks. and spin and color for gluons. The rapid rise of the energy density  $\epsilon$  in a restricted temperature interval can be interpreted in comparison to classical gases where the heat capacity changes when the number degrees of freedom changes. In this case the number of degrees of freedom from 3, in the pion gas, to 37 of the deconfined phase with two flavors. In Fig. 1.3 it is also visible that the saturated values of energy density at high temperatures are still below the expected value given by the Stefan-Boltzmann limit; this indicates residual interactions among the quarks and gluons in the QGP phase. Also the pressure  $p_{SB}$  of a gas of non-interacting quarks and gluons can be determined in the Stefan-Boltzmann limit at  $\mu_B \sim 0$ :

$$p_{SB} = \left[ \underbrace{2(N_f + 1)}_{gluons} + \underbrace{\frac{7}{2} N_c N_f}_{quarks} \right] \frac{\pi^2}{90} T^4 \quad (1.11)$$

where  $N_c$  is the number of colors and  $N_f$  the number of flavors; In Fig. 1.3 the ratio  $p/T^4$  saturates for values of temperature  $T \sim 2T_c$  at a value below the SB limits. In the picture also thermodynamical quantities which characterize the system created in the early stages of heavy-ion collisions at the SPS, RHIC are indicated. This suggest a non ideal behavior in the gas considered in Lattice QCD calculation.

**Chirality Restoration:** in most calculations, the deconfinement transition is also accompanied by a chiral symmetry restoration. The chiral condensate is calculated as a function of temperature  $T$  and baryon density  $\rho$  (ref. §1.1.1), obtaining (for example in the limit of low  $T$  and low  $\rho$ ):

$$\frac{\langle \bar{q}q \rangle_{T,\rho}}{\langle \bar{q}q \rangle_0} \sim 1 - aT^2 - b\rho \quad (1.12)$$

with  $\langle \bar{q}q \rangle_0$  is the vacuum condensate at  $T = 0$  and  $\rho = 0$ ; a and b are two positive constants. From the latter relation we see, in a qualitative way, that in high temperature and density regime, the chiral condensate goes to zero, suggesting a possible restoration of the chiral symmetry. Lattice calculations

found that in the QGP phase, where the particles are deconfined, the chiral condensate goes to zero (Fig 1.4) and that both deconfinement and chiral symmetry restoration occur at approximately the same temperature. As a consequence the position and width of the masses of the light vector mesons ( $\rho, \omega$  and  $\phi$ ) may change [Pis82].

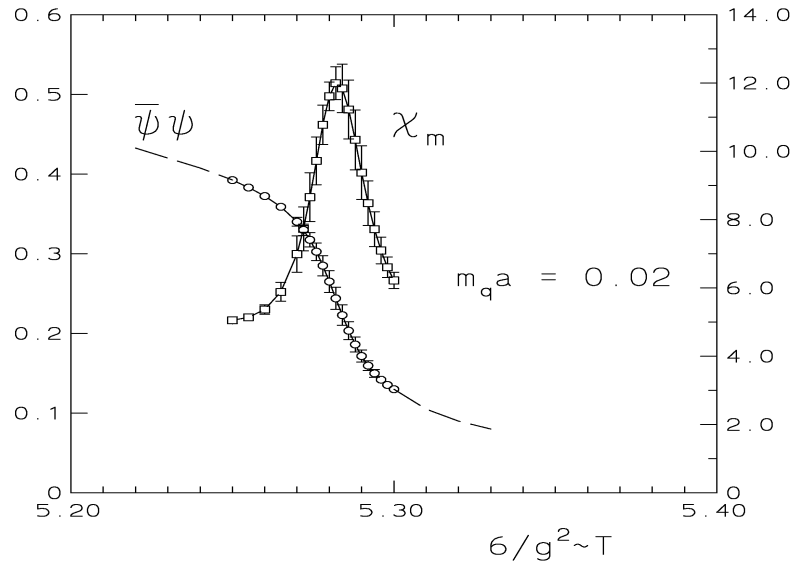


Figure 1.4: The chiral condensate  $\langle \bar{\psi}\psi \rangle$  and the corresponding susceptibility in 2-flavor lattice QCD as function of  $\beta = 6/g^2 \sim T$ , for a quark mass which scales with temperature as  $m_q = 0.08T$ . (From [Kar022])

**Heavy-quark potential** Another important result of lattice QCD is the calculation of the potential between two quarks as a function of the temperature. In the Quark Gluon Plasma, it goes to a constant at long distances, confirming the deconfinement. With increasing temperature the potential flattens towards smaller values and the confinement is lost; indeed, the  $q\bar{q}$  separation decreases as the temperature increases (Fig. 1.5).

The results of lattice calculations suggest to consider the QGP as a weakly coupled medium, characterized by the coupling constant  $\alpha_S(T) \propto 1/\log(2\pi T/\Lambda_{QCD})$ . Thus confirming the evidence of deconfinement found at SPS and the perfect fluid behavior highlighted by RHIC data. In the next section we will discuss the experimental observables available for the experiments.

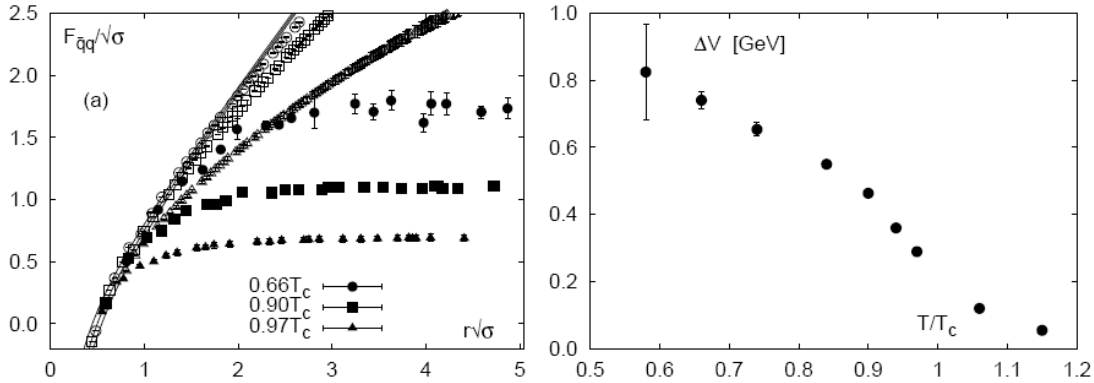


Figure 1.5: Heavy-quark potential for 3-flavor QCD versus the quark-antiquark separation. The different points correspond to lattice calculations with different temperatures.  $\sigma$  is the string tension (From [Kar06]).

### 1.3 Experimental Observables for ALICE

In order to characterize the system produced in heavy-ion collisions as a state of matter, it is necessary to establish if concepts such as temperature, chemical potential and flow velocity can be defined and the system can be described by an experimentally determined equation of state. Additionally, the experiments should be able to provide information on the physical characteristics of the transition, such as the critical temperature, the order of the phase transition and the sound velocity. While at very high temperature ( $T \gg T_c$ , currently experimentally unobtainable) the QGP may behave as made of weakly interacting particles, in the transition region near  $T_c$ , the degrees of freedom of the system may be more complex. The experimental results from the AGS, SPS and RHIC have contributed to the theoretical understanding of the thermodynamic and hydrodynamic properties of the hot strongly interacting matter and of the propagation of partons through such matter. However, the complexity of heavy-ion collisions still lead to a patchwork of theories and models to treat the collision evolution.

It is possible to divide the experimental probes in basically two classes:

**E-W probes:** the study of electroweak products of the collision (essentially dileptons and photons) allows to employ the absence of interactions (in the final state) with the evolving strongly interacting matter. Since these probes are not strongly interacting, they allow to study particles produced in the first stages of the collision bearing the imprints of the bulk properties of these stages. The drawback of this kind of study is the low statistics and the high background

from hadron decays.

**Hadrons:** On the other side, one may focus on the more abundant hadrons, which are affected by final state interactions. It becomes then crucial to distinguish between partonic and hadronic final state interactions and to distinguish both from initial state interactions.

In this section the main heavy-ion observables that will be measured by the ALICE experiment will be discussed, as well as the most significative results obtained by the heavy-ion programs at SPS and RHIC.

### 1.3.1 Kinematic Probes and chemical probes

The average charged-particle multiplicity per rapidity unit (rapidity density  $dN_{ch}/d\eta$ ) is the most fundamental and straightforward observable: it is directly related to the energy of the collision and to the properties of the medium produced in the collision, like the degree of transparency, the number gluons in the initial state. Another important observable is the transverse energy per rapidity unit  $dE_T/d\eta$ , which determines how much of the total initial energy is converted in particles produced in the transverse direction. A prior estimation of the particle multiplicity expected in the experiment is fundamental in the design of the detector, because it can be used to define the granularity of the detectors. Both charged-particle multiplicity and transverse energy cannot be easily extracted from QCD calculation (i.e. starting from the QCD lagrangian) because they include soft processes which are dominant at large distance scale where perturbative QCD fails. As a consequence, there is not a safe estimate of the multiplicity which will be measured at the LHC, even after RHIC data. Before RHIC, extrapolations from SPS at  $\sqrt{s} = 20 \div 200$  GeV mostly overestimated the result. Now that RHIC data are available, extrapolations from  $200 \div 200$  5500 GeV are still difficult.

Since the aim of studying heavy-ion collisions is to discover new effects which are not present in proton-proton collision, it is then appropriate to compare the multiplicities achieved in proton-proton and nucleus-nucleus collisions. This can be quantitatively done introducing the number of participants  $N_{part}$  in the collision which is 2 in  $pp$ , about  $2A$  for central  $AA$  collisions and varies with the centrality. Dividing the multiplicity by  $N_{part}$  gives a measure of how efficient are  $AA$  collisions for each subcollision: Fig. 1.6 shows the extrapolation of  $N_{ch}/(0.5N_{part})$  in proton-proton and nucleus-nucleus collisions from SPS and RHIC. An approximate prediction for the LHC taken directly from the plot is  $dN_{ch}/d\eta \sim 13 \times A_{eff} = 13 \times 170 \sim 2200$  ( $A_{eff}$  is the atomic number effectively considered taking into account centrality cuts): this value is currently an upper limit of the most believed estimations, which

are of the order of 1000 – 2000 particles per rapidity unit. It should be noticed that this value is much lower than the first predictions available at the time when ALICE was designed ( 2000 ÷ 8000 charged particles per rapidity unit).

## Particle Spectra

Most of the particles produced in heavy-ion collisions ( $\sim 99\%$ ) are soft hadrons originated in the late stage of the collision evolution during the hadronic freeze-out. Particle spectra are relevant because they carry indirect information about the early stages of the collision. At the hadronization also called chemical freeze-out the particles decouple from the collision region, move outward and are detected. Spectral shapes can be modified after the chemical freeze-out because rescattering processes among hadrons are expected to occur. Chemical and kinetic freeze-out stages can be studied through short-lived resonances (e.g.  $\rho$ ,  $K^*$ ,  $\Delta$ ). These resonances are produced in the chemical freeze-out and decay before the kinetic freeze-out is reached: the  $\rho$  meson for example has a width  $\Gamma \sim 150$  MeV corresponding to a decay length of  $c\tau \sim 1.3$  fm, smaller than the expected time interval between chemical and kinetic freeze-out (such time scale depends upon the model considered and is of the order of tens of fm). The hadronic decay products of the resonances suffer rescattering processes inside the medium. Therefore it is important to compare hadronic and leptonic decays of resonances to understand better the hadronic rescattering stage. The particle spectra at a given beam energy can be reproduced by a model based on a superposition of local thermal motion and global collective expansion [Lee90] [Hei04]; the model is characterized by an initial state defined by the initial energy density and the initial baryon density. The shape of the spectrum is described by three parameters: the particle mass, the freeze-out temperature  $T$  and the surface velocity at freeze-out  $v_\perp$ . Thermal radiation produces a transverse momentum spectrum [Hag83]:

$$\frac{1}{m_T} \frac{dN}{dm_t d\eta} \propto e^{\frac{m_T}{T}} \quad (1.13)$$

where  $m_T$  is the transverse mass ( $m_T = \sqrt{m^2 + p_T^2}$ ) and  $T$  is the freeze-out temperature. So a direct measurement of  $T$  at freeze-out is the slope of  $\frac{1}{m_T} \frac{dN}{dm_t d\eta}$  in logarithmic scale. Therefore, it is important to know the mass of a particle to have a precise transverse mass instead of the transverse momentum  $p_T$ . At high transverse momenta, the slope of all hadrons is the same as masses can be considered negligible:

$$T_{plot} = T \sqrt{\frac{1 - \langle v_\perp \rangle}{1 + \langle v_\perp \rangle}} \quad (1.14)$$

For non-relativistic transverse momenta, there is a contribution of the collective flow on top of the thermal motion depending on the rest mass of the hadron:

$$T_{plot,i} = T + m_i \langle v_{\perp} \rangle^2 \quad (1.15)$$

where  $m_i$  is the hadron mass. Eq. 1.14 and 1.15 show that the spectra are steeper at high  $p_T$  and become flatter at low  $p_T$ . In order to measure such a change in slope, an experiment must cover the entire low- $p_T$  range, from the smallest  $p_T$  which can be measured to about  $3 \text{ GeV}/c$ . At larger  $p_T$  the slope is no longer described by the collective flow picture. Some results on particle spectra from the SPS and RHIC experiments are reported in Sections 1.4 and 1.5.

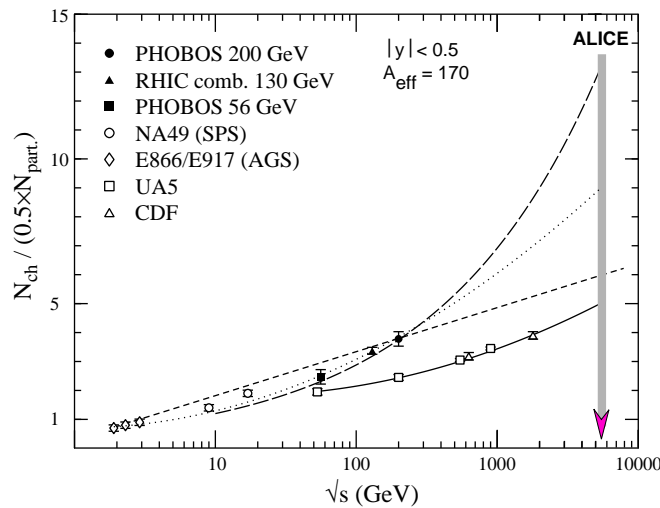


Figure 1.6: Average charged hadron multiplicity per participant pair versus  $\sqrt{s_{NN}}$  in several setups. In the plot several polynomial fits in  $\ln s_{NN}$  are shown.

## Flow

Flow is a collective phenomenon which affects almost all particles produced in a given collision. At low energy it is mainly due to the nucleons in the incoming nuclei and the theoretical interpretations involve the compressibility of nuclear matter or mean field effects. At higher energies, nucleon contributions are negligible at mid-rapidity, where parton effects are expected to be dominant; in this regime, the collective pattern is explained from a theoretical point of view with hydrodynamic models, which are based on the equation of state of the flowing medium provided that the mean free path of particles is much smaller than the system size (see for

example [Hei04, Huo03, Kol03] for a review of the hydrodynamical description of heavy-ion collisions). In the following subsections the different patterns of collective flow (radial and anisotropic) are introduced, as well as the main methods developed in order to do such measurements in heavy-ion collisions.

**Radial flow** In central collisions the overlap region of two spherical nuclei is symmetric in azimuth. This implies an isotropic production of the outgoing particles on the transverse plane. Under such conditions, pressure gradients may intervene resulting in an azimuthally symmetric collective flow of the final state particles, which is called radial flow. This effect is superimposed onto the random thermal motion, thus is observable by studying the transverse momentum distributions of the various particle species (see §1.3.1).

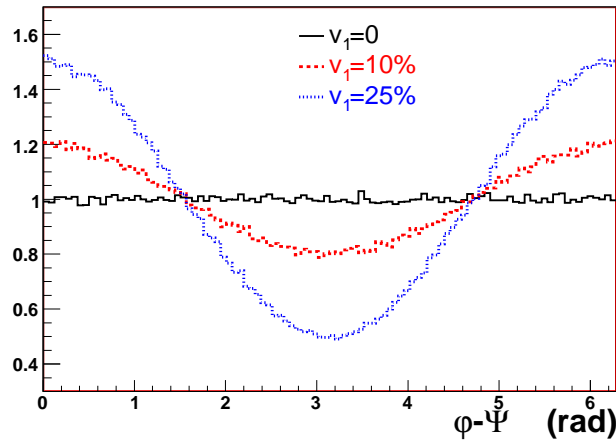


Figure 1.7: Plot of momentum over average momentum as function of  $\phi - \Psi_{RP}$ .

**Anisotropic flow** In non-central heavy-ion collisions, an initially asymmetric overlap region is created. Due to pressure gradients, this almond shaped region tends to assume a more spherical shape as the system expands; if the initially produced particles scatter enough in the overlap region, then the spatial anisotropy is converted into a momentum anisotropy which can be detected even in the later stages of the collision evolution. This will not happen if the particles are not subject to rescattering or if the rescattering is too weak to equilibrate the system before the anisotropy is lost in the expansion of the medium. The momentum anisotropies are described with respect to the reaction plane, which is the plane given by the beam axis and the line connecting the centers of the two colliding nuclei or equivalently is

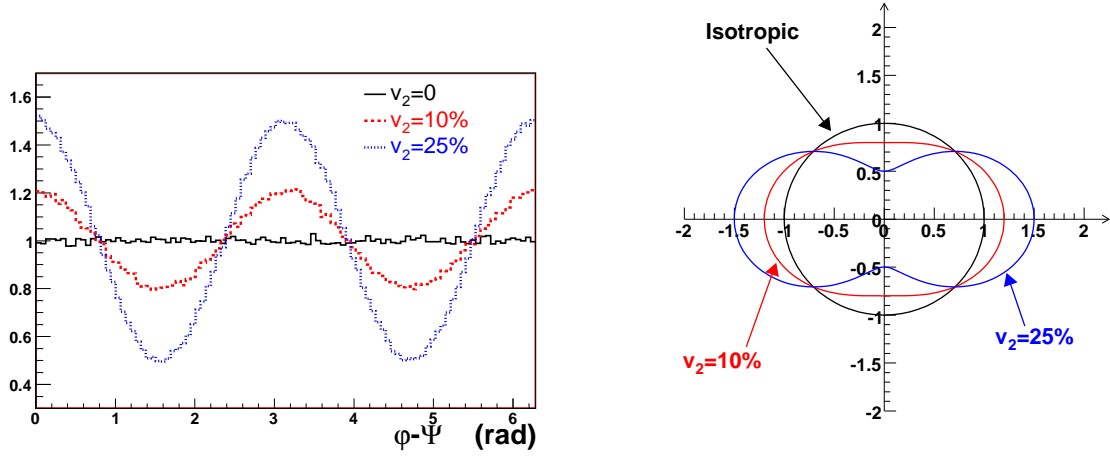


Figure 1.8: Right panel: Plot of the momentum over average momentum as a function of  $\phi - \Psi_{RP}$ . Left panel: Same plot in polar coordinates.

the plane parallel to the beam axis oriented in the direction of the impact parameter of the collision. Hence, the particle azimuthal distribution is parametrized by a Fourier expansion

$$dN/d\phi = N_0 \left\{ 1 + \sum_i 2v_i \cos(i(\phi - \Psi_{RP})) \right\}, \quad (1.16)$$

where  $\phi$  is the azimuthal angle on the transverse plane,  $\Psi_{RP}$  is the azimuthal angle of the reaction plane and  $v_i$  are Fourier coefficients, such parameters can be obtained by:

$$v_i = \langle \cos(i(\phi - \Psi_{RP})) \rangle. \quad (1.17)$$

The first coefficient of the series,  $v_1$ , is called directed flow, while the second coefficient,  $v_2$ , is called elliptic flow. Directed flow quantifies a preferential emission direction along the reaction plane and it is thought to be due to pressure which builds up between the two nuclei. The  $\phi - \Psi_{RP}$  distribution is plotted in Fig.1.7 for different values of the parameter  $v_1$ . According to Fig. 1.7 a non-zero  $v_1$  implies a favored emission along the reaction plane, implying a favored emission angle. This effect cannot be seen at mid-rapidity for symmetric collisions, where there is no reason why pressure should favor one direction rather than the opposite.

At colliders with ultra-relativistic energies, at the early stages of non-central collision, the spectator neutrons which do not take part to the interaction may be bounced off each other in the transverse plane by the pressure established at mid-

rapidity. Since they do not take part to the interaction, they go on towards the forward-rapidity zones where  $v_1$  of the spectator neutrons can be measured.

On the other hand, the elliptic flow  $v_2$  has maxima either in the reaction plane or the perpendicular to the reaction plane (out-of-plane flow,  $v_2 < 0$ ). This pattern reflects the geometrical anisotropy of the interaction region created in symmetric collisions, thus  $v_2$  can be observed at mid-rapidity. The  $\phi - \Psi_{RP}$  distribution is shown in Fig. 1.8 for different values of the parameter  $v_2$ . For  $v_2 = 0$  there is not elliptic flow and the azimuthal distribution is flat as expected. The azimuthal distribution gets more and more peaked at  $\phi - \Psi_{RP} = 0, \pi$ , as  $v_2$  increases. The azimuthal anisotropy with non-zero  $v_2$  is visualized in Fig. 1.8, where the curves represent the profile of the expansion on the transverse plane. The  $x$  axis in the figure is the direction given by the reaction plane. As expected, the emission is isotropic for  $v_2 = 0$ , while for  $v_2 > 0$  the particles are preferentially emitted along the reaction plane. As the matter expands faster in the shorter axis of the overlap region, the spatial asymmetry decreases and thus also the buildup of flow anisotropies ceases and the elliptic flow saturates: elliptic flow is inevitably a self-limiting phenomenon. Saturation may be reached if the time required for the particles to scatter among themselves and transfer the anisotropy to momentum space is shorter than the kinetic freeze-out time. If the initial energy density is sufficiently high, elliptic flow saturates before chemical freeze-out starts. Also the hexadecupole coefficient can be used as a probe of ideal fluid behavior. It is argued that  $v_4(p_t, \eta) = 1/2v_2(p_t, \eta)^2$  [Bor06] for fast particles within ideal fluid dynamics predictions. The experimental value for  $v_2^2/v_4$ , found by the STAR experiment [Ada04] at RHIC is a factor of 2 to 3 higher than the predicted 0.5. A possible explanation is that the equilibrium is not reached at RHIC, and therefore higher values of  $v_4$  are related to the expected deviations from ideal fluid behavior [Bha05].

**Methods of anisotropic flow measurements** In order to perform accurate measurements of anisotropic flow, various procedures were developed, starting from the determination of the estimate of the reaction plane with its error, to the measurement of  $v_n$  with its experimental error.

**Determination of the event plane** The first step is to calculate for each event an estimator of the reaction plane. This estimator is called event plane, and its azimuthal angle is denoted by  $\Phi_R$ . The difference  $\Psi_{RP} - \Phi_R$  depends on the angular resolution of the apparatus, on the magnitude of flow and on the number of particles used for its calculation. The event flow vector  $Q_n$  can be introduced for each harmonic  $n$  of the anisotropic flow [Oll97]:

$$Q_x = \sum_i w_i \cos(n\phi_i) = Q_n \cos(n\Phi_R) \quad (1.18)$$

$$Q_y = \sum_i w_i \sin(n\phi_i) = Q_n \sin(n\Phi_R) \quad (1.19)$$

where the sum runs over all the particles,  $\phi_i$  is the azimuthal angle of each particle and  $w_i$  is a weight selected in order to maximize the resolution. The event plane angle  $\Psi_{RP}$  can be derived from the equations above, measuring the two components of the flow vector. Repeating this procedure for all the events, one should find that the reconstructed event plane has an isotropic azimuthal distribution after proper corrections for instrumental and acceptance effects. This is also a useful check for the analysis.

**Resolution on the event plane** There is a circular reasoning behind the determination of the event plane, i.e. events with uniform azimuthal distribution can have non-zero  $v_i$ , this is particularly true for low multiplicity events due to statistics. The most common procedure to derive the event-plane resolution is to divide each event in two sub-events, assuming that each sub-event maintains the same flow properties as the whole event. The event plane may vary within a given event because it can be calculated rejecting those particles whose flow one wants to measure, in order to avoid auto correlations.

Other methods to determine the coefficients  $v_n$  are not based on the event plane measurement, but rather on azimuthal correlations between pairs of particles [Wan91] or on multi-particle correlations [Bor01]. The latter is also called cumulant method and is less sensitive to contamination due to non-flow effects which remain hidden in the standard methods. Non-flow effects are azimuthal anisotropies mainly originating from two- or four-particle correlations; these effects are superimposed to the effective flow pattern, which is thus biased. Anisotropic flow measurements will be important at the LHC because the initial energy densities will be so high that elliptic flow is expected to saturate well before hadronization: this could be an indication that the QGP thermalized early and can be described as an ideal fluid with an equilibrium equation of state. It is possible to derive properties, such as pressure and energy density, of the matter at the time the anisotropy developed, by comparing the  $v_2$  for different types of hadrons. Theoretical calculations [Hir05, Kol00] as well as extrapolation from lower energies predict  $v_2$  values of about 5% ÷ 10% at the LHC for semi-peripheral events. If they are indeed that large, flow measurement should be feasible; nevertheless, non-flow effects such as correlations due to mini-Jets are expected to be much larger at the LHC than RHIC and to bias the flow signal. ALICE is well suited for such measurements, since with its barrel detectors and its forward zero degree calorimeter it is able to measure both  $v_1$  and  $v_2$ .

### Particle correlations

Since the system created in heavy-ion collisions exhibits a collective behavior, the properties of the fireball immediately before the thermal freeze-out, such as the size or the phase space density, can be assessed through interferometric measurements. The studied quantity is for example the two-particle correlation function:

$$C(p_1, p_2) = \frac{d^6 N}{dp_1^3 dp_2^3} \bigg/ \frac{d^3 N}{dp_1^3} \frac{d^3 N}{dp_2^3} \quad (1.20)$$

It represents the probability of measuring two particles with four-momenta  $p_1$  and  $p_2$  in the intervals  $p_1 + \delta p_1$  and  $p_2 + \Delta p_2$  respectively. The correlation function depends on the emitting source, as it appears in the following definition for spin-0 particles:

$$C(K, q) = 1 + \frac{|\int d^4 x S(x, K) \exp(ix \cdot q)|^2}{\int d^4 x S(x, K + q/2) \int d^4 x S(x, K - q/2)} \quad (1.21)$$

where  $K = (p_1 + p_2)/2$ ,  $q = p_1 - p_2$  and  $x^\mu$  is the space-time four-vector. Here  $S(x, K)$  is the emission function, i.e. the probability to emit a particle of momentum  $K$  from the position  $x$ . The aim of particle interferometry is to learn as much as possible about this emission function: this is not an easy task, first of all because the correlation function depends on the square of Fourier transform of  $S(x, K)$ , therefore the phase of  $S(x, K)$  remains inaccessible. In addition, since the detected identical particles are on their mass shell, the condition  $q \cdot K = 0$  must be verified. This implies that only three of the four components of the four-momentum  $q$  can be determined independently. Usually three spatial components in the so-called *out-side-long* coordinate frame are adopted: *longitudinal* ( $z$ -axis) direction parallel to the beams, *outward* ( $x$ -axis) given by the direction of transverse pair momentum, and *sideways* perpendicular to the above two (in the direction of the  $y$ -axis).  $C(K, q)$  can be then parametrized in terms of the radius parameters  $R_o, R_s$  and  $R_l$ , also called HBT (Hanbury-Brown-Twiss) radii. They are related to the dimension of the fireball. Such a kind of measurements requires good statistics, thus pions and kaons are often used due to their abundance. It is unclear how large the fireball, and thus the HBT radii, will be at the LHC. If the system volume at freeze-out is proportional to the particle multiplicity, then the product  $R_o R_s R_l$  should increase linearly with  $dN/d\eta$ . With the expected multiplicities at the LHC  $(dNch/dy)_{LHC} \sim 1400 \div 3000$  and with the measured value from RHIC  $(dNch/dy)_{RHIC} \sim 650$  one would obtain an increase of the correlation radii by a factor  $[(dNch/dy)_{LHC}/(dNch/dy)_{RHIC}]^{1/3} \sim 1.3 \div 1.7$ . This would result in radii of the order of 8 to 12 fm. However, larger radii (e.g.  $R_l \simeq 15 fm$ ) cannot be firmly ruled out at present. RHIC data suggest an increase in phase-space density at freeze-out, meaning that correlation radii may increase by less than the factor derived above. Measuring the HBT radii it is possible to access

the total lifetime of the system: a larger value or  $R_o^2 - R_s^2$  was indeed proposed as a signal for QGP formation but so far SPS and RHIC data do not show such a signal. The current situation for femtoscopy is that measurements are not yet well understood and theoretical expectations for the LHC are currently still open.

### 1.3.2 Jets

In hadronic collisions, hard scatterings with high momentum transfer occur between some partons involved in the collision; those which instead are not taking part in the hard scattering give origin to the so called “underlying event”. The energetic partons just created undergo a cascade of branching processes which degrade their energies and momenta. This stage lasts until the partons, together with the remnants of the incoming projectiles, fragment into colorless hadrons giving rise to the hadronization phase. This final state is characterized by the presence of clusters of hadrons close in the phase space with high transverse energy and generated by the hard processes at the parton level. QCD calculations predict at the LHC energies for Pb-Pb collisions  $\sim 30$  hard partons per event with transverse energy  $E_T > 10$  GeV and still  $3 \times 10^{-3}$  partons per event with transverse energy  $E_T > 100$  GeV. Besides, the production cross-section for mini-Jets with  $E_T > 5$  GeV is pretty high ( $\sim 30\%$  of the total inelastic cross-section), thus hard processes will be more important at the LHC than at RHIC in understanding the dynamics of the evolution of the system. The estimated number of Jets with  $E_T > 100$  GeV produced in the ALICE central barrel in one month of data taking at average luminosity  $\mathcal{L} = 5 \times 10^{26} \text{ cm}^{-2}\text{s}^{-1}$  is  $10^6$ . Jets are interesting not only because they are connected to hard scatterings occurring in the initial stage of a nucleus-nucleus collision, but also because the high  $E_T$  partons initially produced in such scatterings travel along the nuclear medium before fragmenting into ordinary hadrons. Thus, Jets bring information about the possible in-medium effects involving hard partons. The main nuclear effect which produces the usually called “jet quenching” effect is the energy loss of high  $p_T$  quarks and gluons. Recent calculations suggest that the dominant energy-loss mechanism is radiative rather than collisional [Wan95]. According to these studies, partons radiate gluons and the parton energy loss grows quadratically with the in-medium path length. Some of the expected consequences for the “jet quenching” effect are the following:

- Reduction of the high- $p_T$  particle yield.
- Reduction in the ratio  $\bar{p}/p$  due to the different energy loss of quarks and gluons and to the different contributions of gluons in hadron species.
- Dependence on the impact parameter of the collision: Jet quenching should

be larger in central collisions.

- Two back-to-back Jets with high momentum are not likely to be reconstructed because, due to parton energy loss, Jets with a longer path in the nuclear medium become softer and are thus rejected from the jet algorithms.
- The  $p_T$  spectra of jets made of charm and beauty reveal possible medium modifications of the heavy quark fragmentation functions.

The observables in an heavy-ion collision have to be considered as the sum over the effects in the QGP and the nucleon collisions at the boundary of the ion-ion collision (corona). Therefore the in-medium effect experimental evidences should always be superimposed with a medium-less (nucleon-nucleon) observable. Thus the importance of pp reference data.

### 1.3.3 Photons

Photons are produced at various stages of a heavy-ion collision:

1. In the first stage of the collisions ‘prompt’ photons mainly originate from parton-parton scatterings. This stage is common for both nucleon-nucleon and nucleus-nucleus collisions. The photon production decreases as an inverse power of  $p_t$  but increases with the center-of-mass energy. Photons with  $p_T$  up to several hundreds GeV/ $c$  are expected to be detected at the LHC.
2. During the quark gluon plasma phase (expected to be reached at a temperature of  $\sim 1$  GeV at the LHC) photons are emitted from quarks which undergo collisions with other quarks and gluons of the medium. These photons have an exponentially suppressed spectrum extending up to several GeV.
3. The system then expands and cools. At the hadronization (reached at a temperature of  $\sim 150 \div 200$  MeV), photons are produced either in the scattering of  $\pi$ ,  $\rho$  and  $\omega$  and so on or in resonances and  $\pi^0$  decays. This mechanism survives until the resonances cease to interact. The energy of these photons ranges from a few hundred MeV to several GeV.
4. Once the kinetic freeze-out is also reached, the photon production is mainly due to resonance decays and the spectrum extends up to few hundred MeV.

The main task of photon analysis is to distinguish thermal photons emitted during phases (2) and (3) from the background because one is interested in understanding the properties of the QGP phase and to see whether the system has thermalized or not. One of the experimental difficulties is to extract the background photons

produced by  $\pi^0 \rightarrow \gamma\gamma$  decay channel. An electromagnetic calorimeter requires a good segmentation to separate  $\gamma$  from this background. On the other hand, photons emitted in phase (1) are not easily subtracted and a precise comparison with the proton-proton collisions is needed. Thermal effects can be studied at low energies where the photon production rate is expected to show an excess if the system is thermalized. Higher energy photons, above 20 GeV, are usually produced in association with a recoil Jet: in this kinematic regime thermal effects can be studied analyzing photon-hadron correlations and the shape of the correlation functions. Reliable tests of the thermal photon production are obtained only comparing proton-proton collisions (no thermal effects), proton-nucleus collisions (nuclear effects but no thermal effects) and nucleus-nucleus collisions (both nuclear and thermal effects).

### 1.3.4 Dileptons

As well as photons, dileptons are an interesting tool to determine the properties of the matter produced in heavy-ion collisions because they do not have strong interactions with the medium. The production stages for dileptons are similar to those of photons, i.e. there are prompt dileptons coming from initial hard scatterings, then thermal dileptons are radiated from the QGP and in the final part of the collision evolution, dileptons are produced in meson decays after the chemical freeze-out. The study of dileptons can be divided in kinematic domains:

**Low mass region:** in the dilepton mass range below pair mass  $\sim 1.5$  GeV, thermal dilepton spectra are dominated by decays of resonances like  $\rho$ ,  $\omega$  and  $\phi$ . Medium effects are predicted to occur and to modify the shapes of these resonances. The  $\rho$  meson is particularly interesting due to the large width of  $\sim 150$  MeV that corresponds to a lifetime comparable to  $\tau_{QGP}$  and because of its decay in  $l^+l^-$  is unaffected by the hadronic final state. Several medium effects are expected to affect the production of  $\rho$  mesons[Rap00, Bro91].

**Intermediate mass region:** at masses  $\sim 1.5 \div 2$  GeV there is a prompt contribution to the continuum dominated by semi-leptonic decays of heavy-flavor mesons and by Drell-yan processes ( $\bar{q}q \rightarrow l^-l^+$ ). It is therefore possible to study heavy quark properties, such as their energy loss, through their semi-leptonic channel, as already done at RHIC. Thermal dileptons are expected to be in this region.

**High mass region:** the high mass of the lepton pair spectrum is dominated by  $J/\psi, \psi', \Upsilon, \Upsilon'$  and  $Z^0$  decays. The capability to measure the  $Z^0$  is useful in studies of Jet quenching effect in Pb-Pb collisions where a Jet is produced opposite to a  $Z^0$  or a  $\gamma$ .

### 1.3.5 Heavy quarks and quarkonia

Heavy quarks are produced early after the collision in hard parton scatterings, typically in the following processes:

$\bar{q}q \rightarrow \bar{Q}Q$ , where  $q(\bar{q})$  is a light (anti-)quark belonging to the incoming nucleus and  $Q(\bar{Q})$  is the heavy (anti-)quark.

$gg \rightarrow \bar{Q}Q$ , which is a gluon fusion process and gluons are distributed in the incoming nuclei.

The momentum transfer for such processes has to be larger than  $2m_Q$ , thus heavy quarks are produced on short timescale of the order of  $\sim 1/m_Q$ ; on the other hand, their relatively long lifetime allows them to survive during the QGP phase and to be affected by its presence. However once the quark gluon plasma is formed, the presence of free color charge is expected to screen the binding color potential, leading to the dissolution of quarkonium states because the binding energies are of the order of few MeV and are comparable in size to the mean energies ( $\sim 3T_c$ ) of the plasma. The first states to be suppressed are the less bound, namely the  $\psi'$  and the  $\chi_c$ , followed by the  $J/\psi$ . Also the  $\Upsilon$  family should follow a similar suppression pattern. Heavy quark and quarkonia are one of the experimental probes to investigate the plasma state before freeze-out occurs.

### 1.3.6 Proton-proton physics

With its excellent tracking and particle identification over a broad momentum range (100 MeV/c  $\div$  100 GeV/c), its good secondary vertex determination capability, its low magnetic field and low material budget, ALICE will be a competitive experiment also in proton-proton physics, especially in the low  $p_T$  domain. The interest in pp physics is not only driven by the requirement that a benchmark for heavy-ion collisions is mandatory, but also by the curiosity to explore  $pp$  collisions in a new energy domain.

**Proton-proton collisions as baseline for heavy-ion collisions** There are several reasons why proton-proton measurements are needed as a reference for nucleus-nucleus collisions. The observables to be studied for such purposes are presented below in an incomplete list:

*Particle multiplicities:* differences in particle multiplicities in  $pp$  and A-A are related to different parton distributions in the nucleon with respect to the nuclear case (shadowing effect) in part due to saturation of parton densities at small- $x$ .

*Jets*: models predict that the presence of in-medium parton energy loss affects Jets produced in A-A with respect to those in  $pp$ .

*Slopes of transverse mass*: transverse mass slopes in A-A and  $pp$  are expected to be different because in the nuclear case collective effects like transverse flow should take place.

*Particle yields and ratios*: in A-A they give information on the chemical equilibrium and have to be compared to the same yields and ratios in  $pp$ . Different ratios of momentum spectra at high  $p_T$  in A-A and  $pp$  may indicate that in the nuclear case different contributions of quarks and gluons to the energy loss occur.

*Strangeness enhancement*: this effect has been seen in heavy-ion collisions with respect to  $pp$  at energies between 2 GeV and 10 GeV. It was also observed that the ratio  $K^+/\pi^+$  decreases towards RHIC energies. This ratio at the LHC energies will reveal new mechanisms governing strangeness production.

*Heavy quark and quarkonia production cross sections*: in order to understand clearly the quarkonia suppression and heavy quark energy loss in A-A, their yields must be compared to the ones in  $pp$  collisions.

*Dileptons*: nuclear effects occurring in A-A are expected to affect the dileptons coming from resonance decays; these effects can be revealed only comparing the same dilepton spectra in the  $pp$  case.

*Photons*: photon energy spectra in  $pp$  are needed to estimate the background to thermal photons in A-A.

It must be said that  $pp$  and Pb-Pb data will be collected at different beam energies, therefore the extrapolation from  $pp$  to nucleus-nucleus collisions will not be a straightforward task.

**ALICE contribution to proton-proton physics** ALICE will profit of the its very low  $p_T$  threshold (0.1 GeV/c) and the small radiation length. Several different aspects of QCD, like particle multiplicities, particle spectra, baryon production, strangeness production, Jets, photon production and diffractive physics, low Bjorken  $x$ , will be studied.

## 1.4 Results from the SPS

The experimental program based on heavy-ion collisions started in 1986 at the CERN SPS. The experiments dedicated to Pb-Pb collisions were NA44, NA45/CERES, NA49, NA50, NA52/NEWMASS, WA97/NA57 and WA98. The experiments dedicated to the physics of S nuclei were NA34, NA35, NA80 and NA38. Finally, the most recent experiment, NA60, studied In-In collisions. NA60 is a second generation experiment designed to answer specific questions still open after the previous programs. The NA60 experimental apparatus consists of the muon spectrometer inherited from NA50 and a new tracker system in the target region. This section is dedicated to reviewing the most relevant results obtained during the CERN SPS heavy-ion program.

### $J/\psi$ suppression

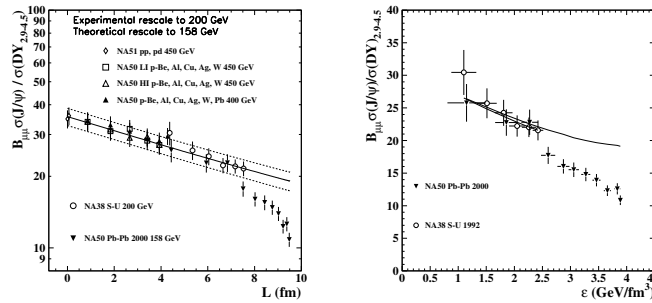


Figure 1.9: Ratio  $J/\psi$  and Drell-Yan cross sections versus  $L$  (left panel) and  $\epsilon$  (right panel)[Ale05].

The suppression of the  $J/\psi$  yield in heavy-ion collisions, predicted by Matsui and Satz [Mat86], is one of the most interesting signals of the formation of a deconfined state of quarks and gluons in relativistic heavy-ion collisions.  $J/\psi$  and  $\psi'$  mesons are detected by NA50 and NA60 through the leptonic decays to a pair of muons: this technique has the advantage that leptons do not have strong interactions with particles produced at hadronization. In order to study quantitatively the suppression pattern of the  $J/\psi$ , the  $J/\psi$  production yield is usually measured with respect to the production of Drell-Yan muons ( $B_{\mu\mu} \sigma(J/\psi) / \sigma(DY)$ ). This ratio is insensitive to experimental efficiencies and furthermore the Drell-Yan process scales linearly with the number of binary nucleon-nucleon collisions. The  $J/\psi$  suppression has been studied as a function of the centrality of the collision using three centrality estimators directly measurable, namely transverse energy, forward energy and

particle multiplicity. The results were also expressed as a function of three calculated variables which better describe the system created in the collision: the average length  $L$  of nuclear matter traversed by the  $c\bar{c}$ -state, the energy density  $\epsilon$ , averaged over the whole transverse area of the collision and the number of participants  $N_{part}$ . They are calculated starting from measured centrality estimators using the Glauber model [Gla70]. Fig. 1.9 shows the  $J/\psi$  production yield over Drell-Yan as a function of  $L$  for different collision systems. The same  $J/\psi$  yield is plotted in the right panel of Fig. 1.9 as a function of the energy density, for S-U and Pb-Pb. These plots clearly show that Pb-Pb peripheral collisions with  $L < 7$  fm and  $\epsilon < 2.3$  GeV/fm<sup>3</sup> exhibit a  $J/\psi$  production yield in agreement with the behavior observed in p-A reactions and presently understood as due to  $J/\psi$  absorption in ordinary nuclear matter. For more central collisions, a departure from the normal nuclear absorption curve was observed ( ‘‘anomalous suppression’’ ) without saturation even in the most central Pb-Pb collisions. S-U data and other lighter systems closely match the absorption curve determined by p-A points. A second analysis technique introduced by NA60 overcomes the problem of the low Drell-Yan statistics by studying the measured  $J/\psi$  without any normalization to the production of Drell-Yan muons. In this approach, the observed  $J/\psi$  centrality distribution is directly compared to the theoretical distribution expected in case normal nuclear absorption is the only suppression mechanism. This analysis is feasible in NA60 thanks to the vertex detector which allows the selection of the  $J/\psi$  coming from the primary interaction; the achieved invariant mass resolution on the  $J/\psi$  is  $\sim 70$  MeV/ $c^2$ , smaller than the one achieved by NA50 without vertex detector,  $\sim 100$  MeV/ $c^2$ . NA50 was based on multiplicity measurements and did not allow the detection of direct  $J/\psi$ , especially for peripheral events. Hence, the normalization to Drell-Yan processes was needed. The result is shown in Fig. 1.10, where the ratio between the measured and the expected  $J/\psi$  yield is plotted as a function of the number of participants. The observed pattern indicates that an anomalous suppression is already present in In-In collisions, setting in at  $N_{part} \sim 80$  with a saturation for more central events. The data from the previous experiments NA38 and NA50 also reported in Fig. 1.10 are obtained with the standard analysis based on the normalization to Drell-Yan production, differently from NA60 which measures direct  $J/\psi$ .

### The $\rho$ spectral function

In the low mass sector ( $m < m_\phi$ ) the CERES experiment has studied the production of dielectron pairs in nucleus-nucleus collisions [Aga05]. An excess has been observed and well established in the dielectron mass distribution in the low mass region but the lack of statistics and a poor mass resolution did not allow a clear discrimination between the various theoretical explanations. Fig. 1.11 shows the opposite-sign,

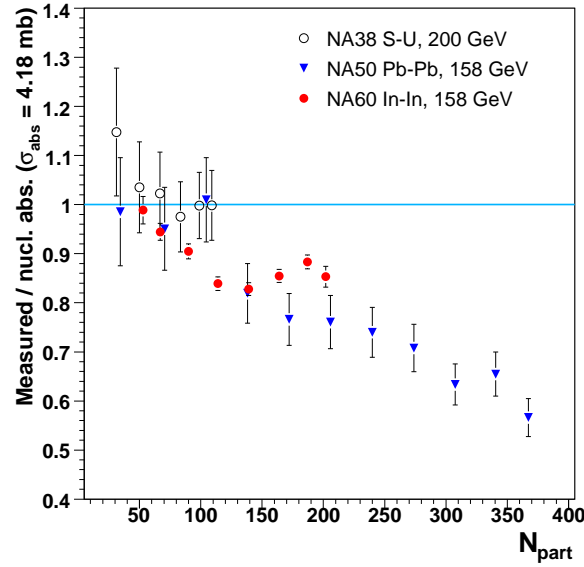


Figure 1.10: Ratio between measured  $J/\psi$  yield and the absorption curve as a function of  $N_{part}$  for S-U, Pb-Pb and In-In collisions. Taken from [Arn07].

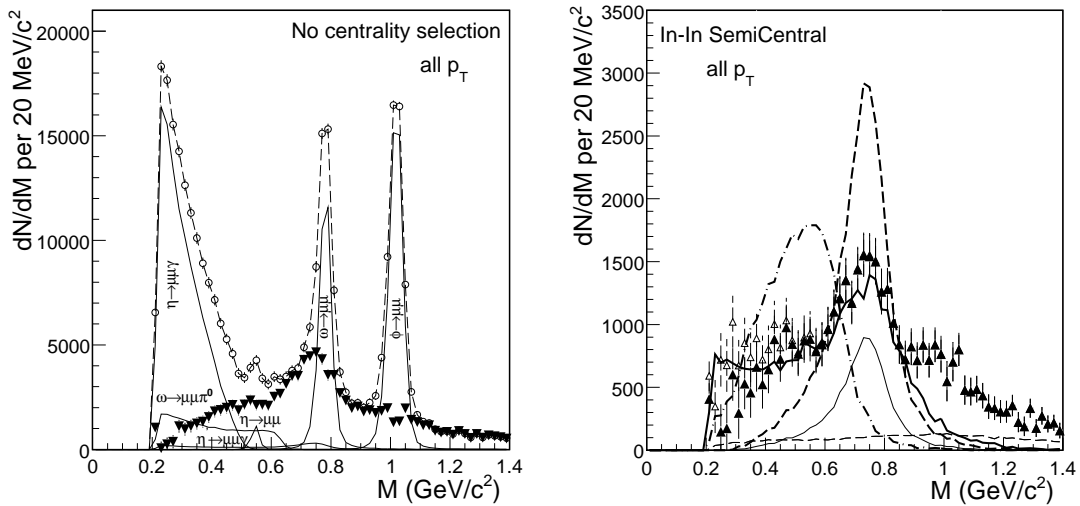


Figure 1.11: Combinatorial background (dashed), signal fake matches (dashed-dotted) and resulting signal (lower histogram with error bars). Right: comparison of the excess mass spectrum for the semi-central bin to model predictions, such as unmodified  $\rho$  (dashed), in-medium broadening  $\rho$  (thick solid), in-medium moving  $\rho$  (dashed-dotted). [Foe09].

background and signal dimuon mass spectra as measured by NA60, integrated over all collision centralities. The excess is isolated using a novel procedure and the result is plotted in Fig. 1.11 (right) for semi-central In-In collisions. The comparison with theoretical models indicates that the excess shape is consistent with a broadening of the  $\rho$  meson rather than a mass shift of the  $\rho$  [Foe09].

### Particle spectra

As already mentioned, the particle yields as a function of the transverse momentum reveal the dynamics of the collision, characterized by the temperature and the transverse flow velocity of the system at the kinetic freeze-out.

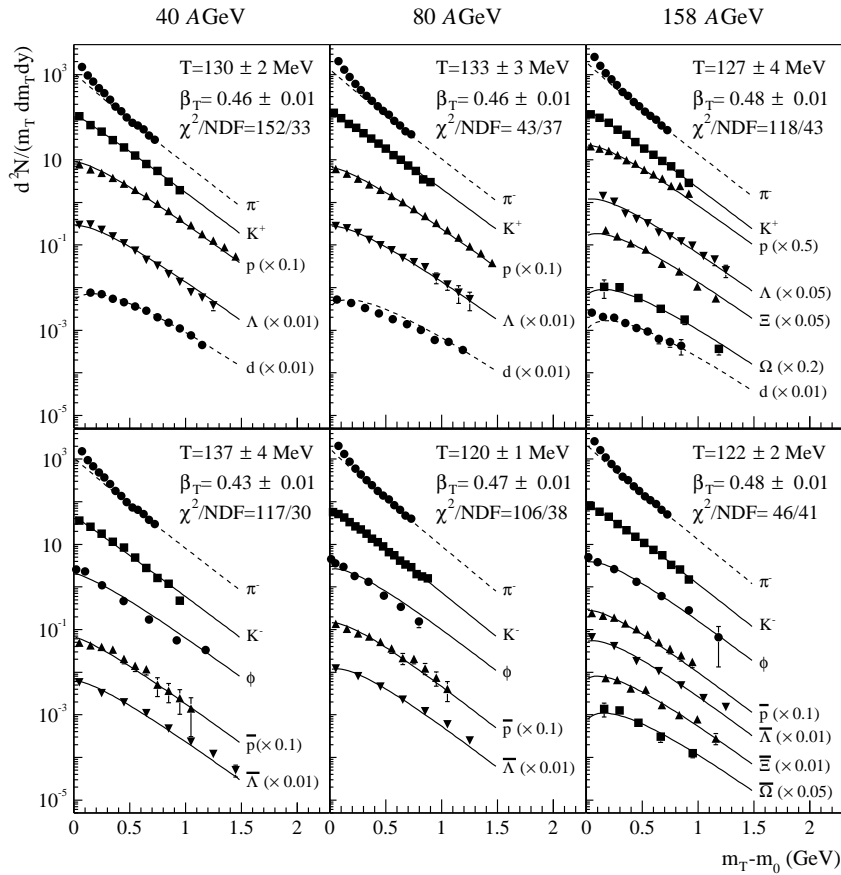


Figure 1.12: Positively and negatively charged hadron spectra from central Pb-Pb collisions at 40, 80 and 158 GeV per nucleon (left to right), measured by the NA49 Collaboration. The results of the fits based on the hydrodynamic model are reported in the figure.[Lee90, Hei04]

Fig. 1.12 shows the transverse mass distributions for positively and negatively

charged hadrons produced in central Pb-Pb collisions at 40, 80 and 158 GeV per nucleon, measured by the NA49 Collaboration [Lee03]; the lines are a fit based on the hydrodynamically inspired model introduced in §1.3.1. The  $m_T$  spectra are compatible with radial flow, with similar temperature  $T \sim 130 \text{ MeV}$  and transverse flow velocity  $v_\perp \sim 0.45$  at the different energies. The spectra for  $\Xi$  and  $\Omega$ , which are measured only at 158 GeV, do not show indications of early freeze-out.

## 1.5 Recent results and open issues from RHIC

All the four experiments at RHIC have been successful in providing information on the dynamics of heavy-ion collisions in a new regime of very high energy densities. The theory-experiment comparison indicates that central Au-Au collisions at RHIC produce a unique form of strongly interacting matter. In order not to go too far from the main subject of this thesis, only the main results obtained by the PHENIX, STAR, PHOBOS and BRAHMS experiments at RHIC will be presented in this section.

### 1.5.1 Energy density and multiplicity measurements

The energy density achieved at RHIC is well beyond the energy density required by Lattice calculations  $\sim 15 \text{ GeV}/\text{fm}^3$ . Most of bulk properties, in contrast with the predictions made before the RHIC start, show only very modest with centrality and beam energies.

This is shown for example in Fig. 1.13, where it is clear that the measured multiplicities per participant as a function of the center-of-mass-energy are not reproduced by the sharp curve predicted by factorized pQCD: hence, some mechanisms must be present at RHIC energy to reduce the particle production. One possible explanation is given by the Color Glass Condensate (CGC) picture [McL01], which describes the initial state at small- $x$  of hadrons as well as heavy nuclei. In this model the small- $x$  gluon density begins to saturate because of the competition of gluon fusion ( $gg \rightarrow g$ ) and gluon splitting ( $g \rightarrow gg$ ) processes. There is a critical momentum scale  $Q_s$ , (with  $Q_s \gg \Lambda_{QCD}$  and also called CGC saturation scale), depending on both the longitudinal parton momentum fraction  $x$  and the atomic number  $A$ , which controls the occupation number of gluons inside a nucleon. For transverse momenta  $p_T < Q$ , the transverse gluon phase space density is saturated. It has been conjectured that saturation in nuclei occurs at higher  $Q_s$  or equivalently at higher  $x$  (at fixed  $Q_s$ ) compared to single protons, and that the Color Glass Condensate may explain the so called nuclear shadowing effect. Fig. 1.14 confirms that the CGC reasonably reproduces the experimental data and could be considered as the initial

state of a nucleus-nucleus system, from which the subsequent QGP evolves.

### 1.5.2 Thermalization

The measured yields and spectra of different hadron species are consistent with thermal emission from a strongly expanding source. The transverse momentum spectra for identified particles from the STAR experiment are reported in Fig.1.15; a fit to the spectra shows that the system seems to freeze-out with a temperature and expansion velocity similar to that observed at the SPS energies. The obtained fit parameters for the 0-5% Au-Au events are  $T = 89 \pm 10 \text{ MeV}$  and  $\beta_s = 0.84 \pm 0.07$ . The strangeness production is consistent with predictions based on a complete chemical equilibrium reached at a chemical freeze-out temperature of  $163 \pm 5 \text{ MeV}$  and a baryo-chemical potential  $\sim 25 \text{ MeV}$  [STA05]. This result is compatible with the QGP transition temperature predicted by lattice QCD calculations. The scaling of the elliptic flow  $v_2$  with eccentricity (see Fig. 1.16) for low  $p_T$  ( $p_T < 1 \text{ GeV}/c$ ) shows that  $v_2$  is strongly connected with the spatial asymmetry of non-central collisions and therefore indicates that a high degree of collectivity is built up at a very early stage of the collision. Hydrodynamic models, based on an ideal fluid, on a early thermalization ( $\tau_{therm} \leq 1 \text{ fm}/c$ ) and on a high initial energy density ( $\epsilon \geq 10 \text{ GeV}/\text{fm}^3$ ), reproduce reasonably well the measured  $v_2(p_T)$  of pions, kaons and protons. This is an evidence for the formation of a strongly interacting matter that thermalizes very rapidly. Nevertheless, the hydrodynamic calculations have not succeeded yet in explaining the emitting hadron source from measured HBT correlations. Hence, currently there is not a consistent picture of the space-time dynamics of reactions at RHIC.

### 1.5.3 Binary scaling and high $p_T$ suppression

One of the tasks of RHIC experiments is to understand if the particle yield in d-Au and Au-Au can be considered as the result of independent collisions between the point-like constituents of the nucleons. If this happens, the production should scale with  $pp$  yield with a coefficient,  $N_{coll}$ , which is the average number of binary nucleon-nucleon inelastic collisions. This is the reason why the scaling law for point-like processes is also called binary (or  $N_{coll}$ ) scaling. In order to establish whether the binary scaling has occurred or not, d-Au data must be used at first, since they do not have final state effects due to the medium. Nuclear medium effects, either in the initial or final state scaling, can modify the expected scaling: these modifications can be quantitatively estimated by measuring the *nuclear modification factor* RAA,

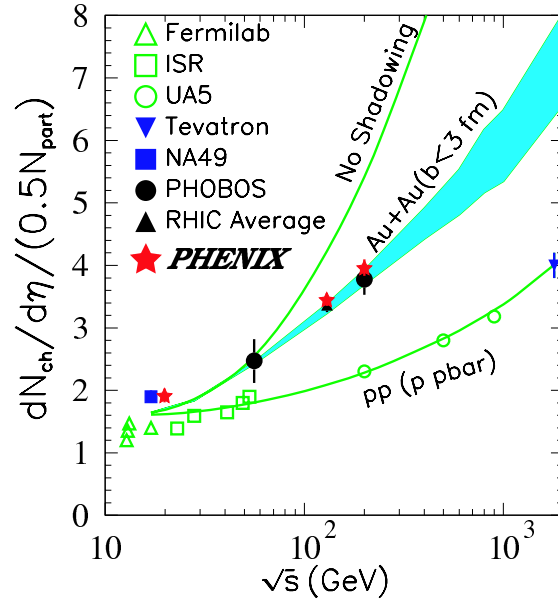


Figure 1.13: Measured mid-rapidity charged particle densities, scaled by the calculated number of participant nucleons, for central collisions at SPS and RHIC, plotted as a function of the center of mass energy. Results from  $p\bar{p}$  and  $pp$  collisions are shown for comparison.[PHE05]

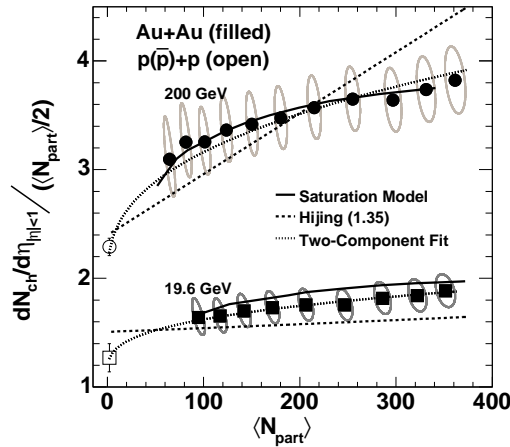


Figure 1.14: Pseudorapidity density of charged particles at midrapidity divided by the number of participant pairs as a function of the number of participants. Data are shown for Au-Au at 19.6 GeV and 200 GeV center of mass energies.  $pp$  data measured at 200 GeV and interpolated to 19.6 GeV are also shown. The ellipses represent the 90% C.L. systematic errors.[Bac05]

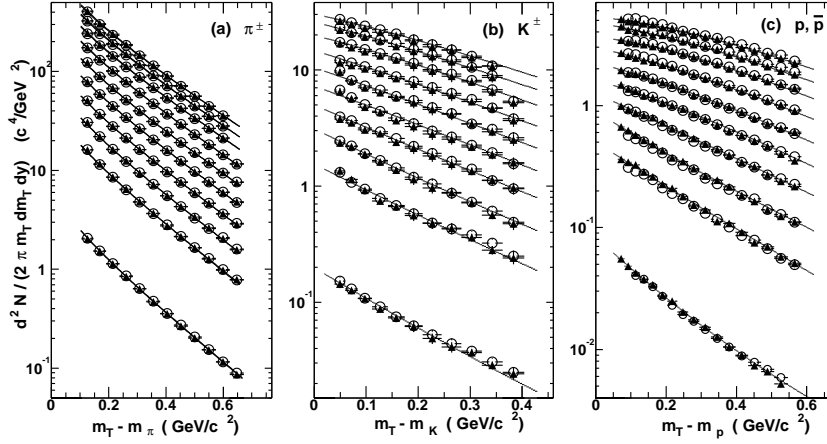


Figure 1.15: Invariant yield as function of transverse mass for  $\pi^\pm$ ,  $K^\pm$  and inclusive  $p$  and  $\bar{p}$  at mid-rapidity ( $|y| < 0.1$ ) for pp (bottom) and Au-Au events at  $\sqrt{s_{NN}} = 200$  GeV from 70-80% (second bottom) to the 0-5% centrality bin (top). The curves shown are Bose-Einstein fits for  $\pi$  and hydrodynamic-based (blast-wave) model fits for  $K$  and  $p$ . [STA04t]

defined as follows:

$$R_{AA} = \frac{dN_{AA}^P}{\langle N_{coll} \rangle \times dN_{NN}^P} \quad (1.22)$$

where  $dN_{AA}^P$  is the yield of a point-like process in nucleus nucleus collision and  $dN_{NN}^P$  is the yield for the same process in nucleon-nucleon collision. Alternatively, the central to peripheral ratio  $R_{CP}$  is used:

$$R_{CP} = \frac{dN^{centr} / \langle N_{coll}^{centr} \rangle}{dN^{per} / \langle N_{coll}^{per} \rangle} \quad (1.23)$$

where  $dN^{centr}$  and  $dN^{per}$  are the differential yields of the studied process for central and peripheral collisions respectively. The two quantities  $R_{AA}$  and  $R_{CP}$  can be measured also in d-Au collisions. If the yield of the process scales with the number of collisions ( $N_{coll} \propto A^{4/3}$ ), we expect  $R_{AA} = 1$  and  $R_{CP} = 1$ . The above definitions are valid only for hard point-like scatterings, which guarantee the validity of the factorization theorem in the calculation of the cross section. Therefore, the cross sections in pp, pA or AA collisions are proportional to the number of possible point-like encounters and the cross sections in pA or AA, compared to pp, scale with the number of binary nucleon-nucleon collisions. On the other hand, the soft regime is characterized by a scaling of the cross sections in pA or AA, compared to pp, with the number of participants ( $N_{part} \sim A$  in case of pA collisions and  $N_{part} \sim 2A$  in

case of AA collisions). In this case, we expect for Au-Au collisions:

$$R_{AA} = \frac{\langle N_{part} \rangle dN_{NN}}{\langle N_{coll} \rangle \times dN_{NN}^P} = \frac{2 \times 197}{197^{4/3}} \simeq 0.34 \quad (1.24)$$

which is compatible with the plots on  $R_{AA}$  measured at RHIC reported in the following (Fig 1.19). Hard scattering is considered the dominant process for particle production with  $p_T > 2$  GeV/c at mid-rapidity in pp collisions at RHIC. Indeed, as can be observed in Fig. 1.17, the spectra for pp collisions exhibit an asymptotic power law, due to hard scattering processes, with increasing  $x_T$  ( $x_T = 2p_T/\sqrt{s}$ ). The transition region from hard to soft physics at RHIC lies in the  $p_T$  region of about 2 GeV/c. The binary scaling does not hold in the soft physics regime, due to additional scattering processes, and  $R_{AA} < 1$ . Therefore, in order to look for a possible breaking of the binary scaling, only the hard momentum region has to be considered, as shown in Fig 1.18.

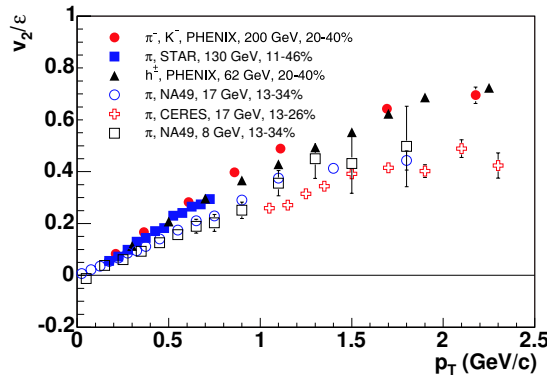


Figure 1.16:  $v_2(p_T)$  normalized by the eccentricity  $\epsilon$  as a function of  $p_T$ , for midcentral collisions at RHIC (filled symbols) and SPS (open symbols). Dividing by  $\epsilon$  makes a uniform comparison between different nuclei and different centrality selections.[Bac05]

Fig 1.19 shows the  $R_{AA}$  of particles produced at mid-rapidity in d-Au collisions as a function of the transverse momentum  $p_T$  (left panel for STAR and right panel for PHENIX): it is clear that the binary scaling is not respected in d-Au collisions, indeed an enhancement is observed at intermediate  $p_T$ . This behavior, known as Cronin effect [Ant79], is generally attributed to the influence of multiple scattering before the hard collisions.

At large rapidities in the deuteron direction, a suppression of high- $p_T$  hadrons has been observed by the BRAHMS collaboration: this pattern suggests a depletion of small- $x$  gluons in the colliding Au nucleus and is in qualitative agreement with the

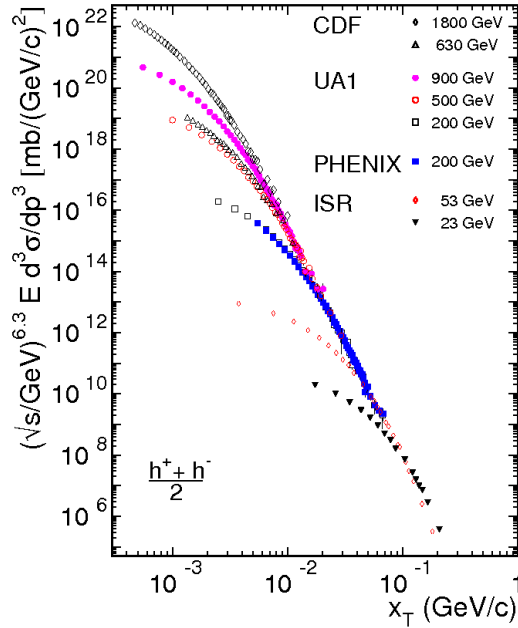


Figure 1.17:  $\sqrt{s}^{6.3} (\text{GeV}) \times E \times d^3\sigma/dp^3$  versus  $x_T = 2p_t/\sqrt{s}$  at mid rapidity for  $pp$  collisions for different  $\sqrt{s}$  and experiments.

predictions of gluon saturation models. The  $R_{AA}$  of  $\pi^0$  (Fig.1.19) for central Au-Au collisions at RHIC is well below 1 over the entire measured  $p_T$  range, revealing that the  $\pi^0$  yields are strongly suppressed relative to the expected yields given by the binary scaling. In contrast, the peripheral yields show little or no suppression. The observed suppression of hadron yields in central collisions can be efficiently described by perturbative QCD calculations incorporating parton energy loss in a thin and dense medium. The magnitude of such suppression needs to assume that the initial gluon density when the collective expansion begins is more than a order of magnitude greater than that in the ordinary nuclear matter ( $dN_g/d\eta \sim 1000$ )[Wan95]. Also the initial energy density is required to be above the one present in nuclear matter ( $\epsilon_0 \sim 15 \text{ GeV}/\text{fm}^3$  compared to  $\epsilon_{nucl} \sim 0.17 \text{ GeV}/\text{fm}^3$ ). These values are consistent with those obtained with  $dE_T/d\eta$  measurements and with the predictions from hydro models. The magnitude of the suppression at high  $p_T$  reported for Au-Au collisions in Fig. 1.19 ( $R_{AA} \sim 0.25$ ) is in qualitative agreement with a simple argument based on the assumption that only the jets emitted on the surface of the fireball and directed outward can be triggered, while those emitted inside the fireball and directed inward are lost due to medium effects. Therefore, the number of triggered Jets should be proportional to the surface of the medium rather than to its volume.

We should then expect for Au-Au collisions:

$$R_{AA} = \frac{R^2}{R^3} \sim \frac{A^{2/3}}{A} \sim 0.2 \quad (1.25)$$

where  $R \propto A^{1/3}$  is the nucleus or the “fireball” radius. Another important result is the confirmation that high- $p_T$  hadrons result from hard scatterings followed by Jet fragmentation. Since a hard-scattered parton fragments into multiple particles within a restricted angular region (jet), one would expect to observe angular correlations between hadrons in the jets: this is visible in Fig. 1.20, where the peak at  $\Delta\Phi = 0$  (near side) represents the correlation between hadrons in the same Jet, while the broader peak at  $\Delta\Phi = \phi$  (away side) reflects the correlation between hadrons in one jet and hadrons produced in the opposite jet. The away side correlation peak is absent in case of central Au-Au collisions; on the contrary, peripheral Au-Au, d-Au and pp collisions exhibit the same shape of the back-to-back peak. This leads to the suggestion that, if the correlation is the result of Jet fragmentation, the suppression in Au-Au collisions is due to final state interactions of hard-scattered partons or of their fragmentation products in the dense medium. In this scenario, the hard hadrons (and thus the near-side peak) are the ones produced in hard parton scatterings occurring on the surface of the collision region and outward. On the contrary, partons exiting inward lose part of their energy crossing the dense matter and do not form the away-side peak. Another confirmation of the parton energy loss mechanism is the plot in the right panel of Fig. 1.20, where the dihadron correlation is shown with two different orientations of the trigger hadron with respect to the reaction plane (direction of the impact parameter of the collision): parallel to it (in-plane) or orthogonal to it (out-of-plane). The suppression of the away-side peak depends strongly on the relative angle between the trigger hadron and the reaction plane: for an out-of-plane trigger hadron, the correlated opposite jet must cross a longer path than in the reaction plane, leading to correspondingly larger energy loss.

#### 1.5.4 Hadron production

The process of hadronization, to date not well understood, includes the dressing of the quarks from their bare masses and the confinement of the quarks into colorless hadrons. The hadron production in the soft region ( $p_T \leq 2 \text{ GeV}/c$ ) is reasonably described by hydrodynamics, while in the hard region ( $p_T \geq 5 \text{ GeV}/c$ ) hydrodynamics should fail and fragmentation should dominate. The intermediate- $p_T$  regime ( $p_T \in [2, 5] \text{ GeV}/c$ ) is particularly interesting since it represents the transition between soft and hard production mechanisms. The jet fragmentation dominates in the high- $p_T$  range, but it is still not clear the intermediate- $p_T$  region, where also the coalescence mechanism is supposed to occur. The quark recombination or coalescence

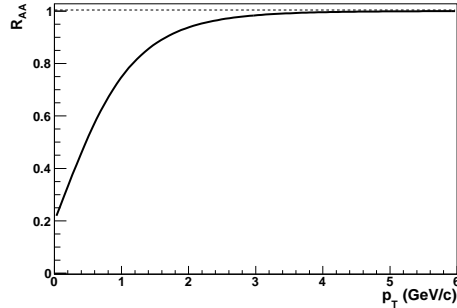


Figure 1.18: Schematic representation of the RAA as a function of the transverse momentum in case of no medium effects occur. For  $p_T \geq 2$  GeV/c the binary scaling holds.

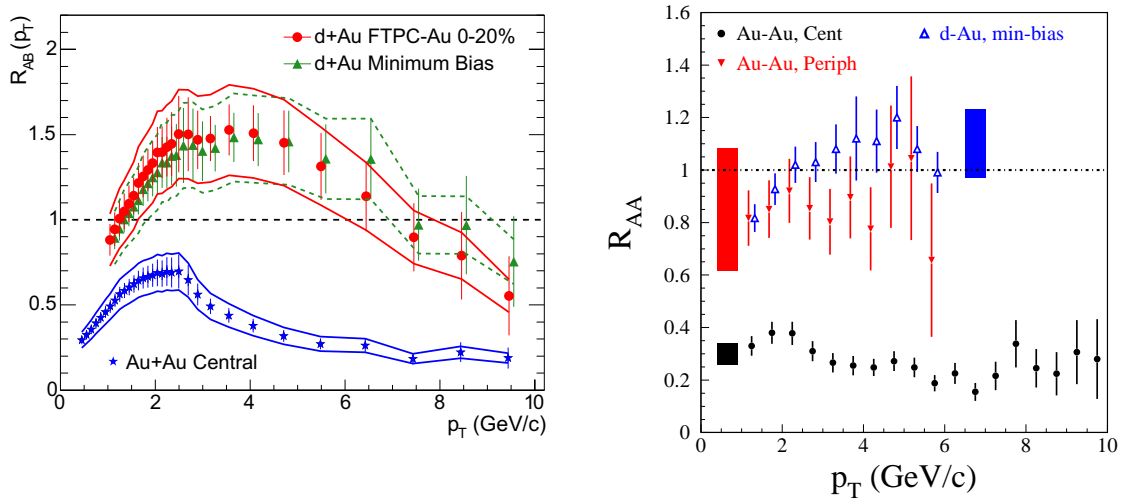


Figure 1.19: Left: binary-scaled ratio  $R_{AB}(p_T)$  of charged hadron yields from 200 GeV Au-Au and d+Au relative to pp collisions from STAR [STA05]. Right: the same ratio for  $\pi^0$  for central (0-10%) and peripheral Au-Au collisions and d-Au minimum bias collisions from PHENIX.[PHE05]

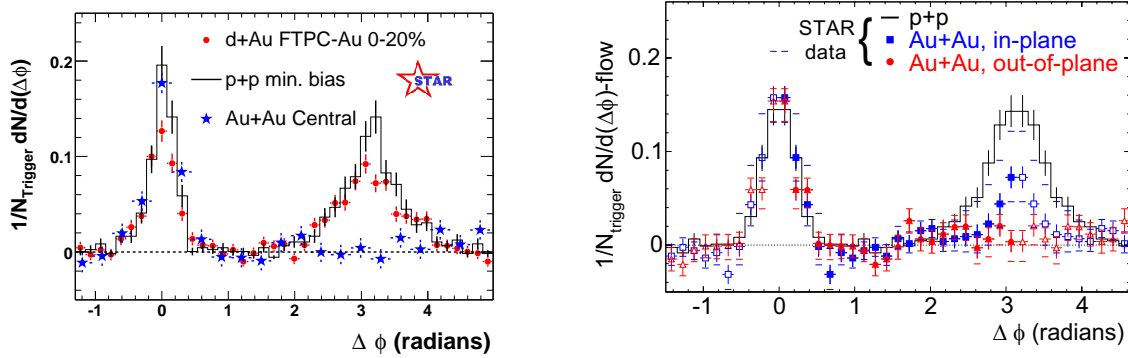


Figure 1.20: Dihadron azimuthal correlations at high  $p_T$ . Left panel shows correlations for pp, central d-Au and central Au-Au collisions (background subtracted) from STAR. Right panel shows the background-subtracted high  $p_T$  dihadron correlation for different orientations of the trigger hadron relative to the Au-Au reaction plane.[STA05]

models assume that quarks in a densely populated phase space combine together to form the final-state hadrons. It is indeed in the intermediate- $p_T$  regime that it was observed at RHIC a large enhancement of baryons and antibaryons relative to pions. Although there are several models based on the quark recombination or coalescence [Fri05] which try to describe the ratio  $p(\bar{p})/\pi$ , the anomalous enhancement remains a puzzle. According to such models, baryons at moderate  $p_T$  would be enhanced relative to mesons because their transverse momentum is the sum of 3 quarks rather than 2. Furthermore, recombination predicts that the collective flow of final-state hadrons should follow the collective flow of their constituent quarks, which is somewhat observed in RHIC data at intermediate  $p_T$ , as discussed in the following. At present, no theoretical framework provides a complete understanding of hadron formation in the intermediate- $p_T$  regime: on one side, baryons have a large  $v_2$  (typically 20%) indicative of strong collective motion, on the other side the near-angle correlation between particles is characteristic of jet fragmentation. One possible solution to this unclear issue can be provided by the measurement of  $v_2/n_q$ . Fig. 1.21 shows  $v_2/n_q$  as function of the transverse momentum per valence quark  $p_T/n_q$  and the transverse kinetic energy per valence quark  $KE_T/n_q = (m_T - m)/n_q$  for  $p_T/n_q > 1$  GeV/c. The existence of a common scaling for all the species of particle strongly support a collective motion on quark basis. An experimental measurement supporting the recombination models is also the  $R_{CP}$  of  $\phi$  meson: present data show that follows the pattern of  $K_S^0$  as well as  $\pi$  although its mass is more similar to the proton's or  $\Lambda$ 's. Also the first measurement of  $\phi$  elliptic flow  $v_2$  from

STAR shows that at intermediate  $p_T$   $v_2$  favors the number of constituent quark scaling.

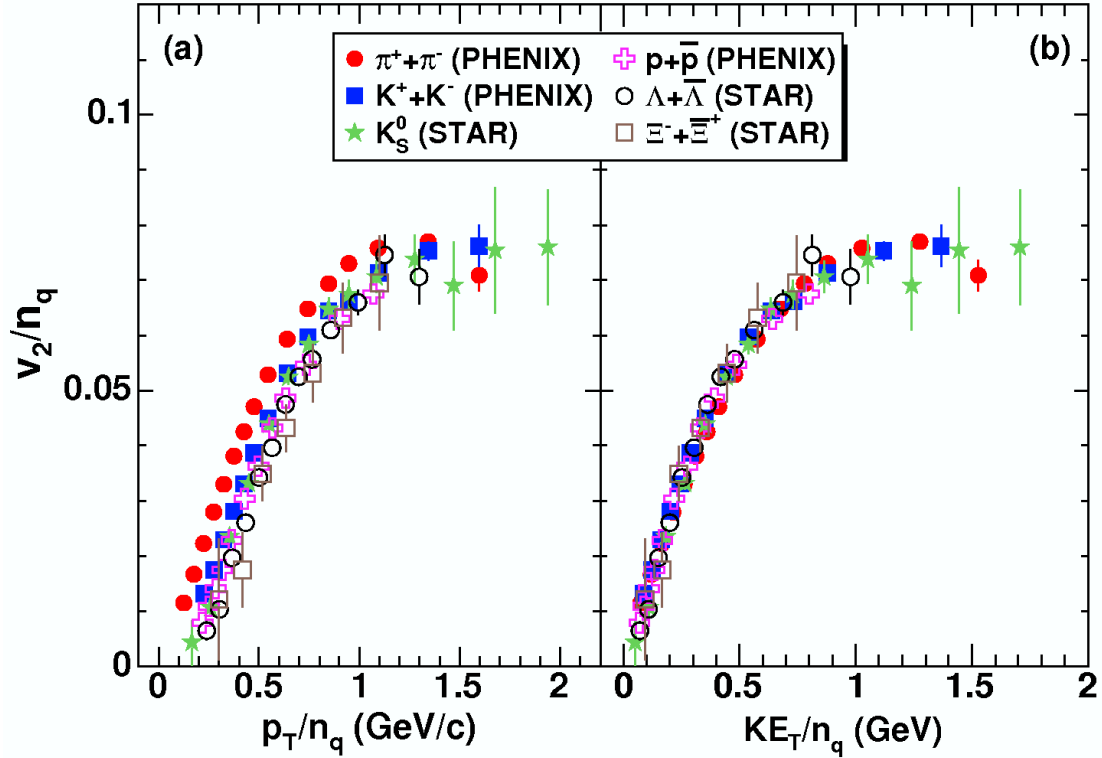


Figure 1.21:  $v_2/n_q$  as a function of  $p_T/n_q$  (left panel) and  $KE_T/n_q$  (right panel), where  $n_q$  is the number of constituent quarks. Data are from PHENIX Minimum Bias Au-Au collisions at  $\sqrt{s} = 200$  GeV, for  $p_T/n_q > 1$  GeV/c.

### 1.5.5 Open issues and needs from future experiments

The interesting results obtained so far by RHIC still reveal that a complete theoretical framework able to describe the fundamental properties of the matter produced is not achieved. In order to reach such a goal, also on the experimental side several measurements which can quantitatively test the theoretical predictions are needed. The main prospects for the short term RHIC measurements and for a longer time scale (LHC, RHIC upgrade) are briefly summarized in the following:

- Establish whether or not the  $v_2$  scaling is really existing.

- Measure open charm yields and flow to understand the collective properties of the matter including heavier quarks and to study the relative contributions of coalescence and fragmentation in the charmed hadron production.
- Find probes which can be used as thermometers for the early stages of the collisions, well before the chemical freeze-out.
- Measure yields and spectra of various heavy quarkonium species, including the  $\Upsilon$  states.
- Test the fundamental QCD symmetries (chiral, CP,...) in the strongly interacting matter.
- Extend at the LHC and GSI the models which work at RHIC and quantitatively compare the predictions with the experimental measurements.

# Chapter 2

## ALICE experiment

In the previous chapter a subset of observables in the relativistic heavy ion physics program was introduced. The ALICE detector at LHC is the cutting edge of the experiments in this field. The most recent developments in relativistic heavy ion physics are made at RHIC, a collider at the BNL laboratory. This collider hosts four detectors (STAR, PHENIX, PHOBOS and BRAHMS) specialized in particular observables; in ALICE however the idea is to create a single detector able to measure all the observables that characterize QGP. In the next section the design and details of ALICE will be covered

### 2.1 The experimental design

LHC will collide Pb nuclei at  $\sqrt{S_{NN}} = 5.5$  TeV,  $\sim 27$  times larger than that achieved at RHIC; the predictions for the multiplicity in central Pb-Pb collisions at the LHC at the time of ALICE design were defined in a wide range from 2000 to 6000 charged particles per rapidity unit at mid-rapidity (see Chapter 1). The ALICE detector was consequently designed to cope with a multiplicity of 8000 charged particles per rapidity unit. This very high multiplicity guarantees a safety margin. The interaction rate for Pb-Pb collisions at the nominal luminosity of  $\mathcal{L} \sim 10^{27} \text{cm}^{-2} \text{s}^{-1}$  is  $R = \mathcal{L} \times \sigma \sim 8000 \text{s}^{-1}$ , where the cross section for minimum bias collisions is  $\sigma \sim 8b$ . Such a rate allows the use of slow but high-granularity detectors, like the time projection chamber and the silicon drift detectors. The main requirements for a heavy-ion experiment are an efficient tracking system within a large acceptance and a good particle identification in a wide momentum region. An efficient online trigger system is also required for specific analyses, for example those involving high- $p_T$  electrons and rare processes. Tracking is performed in ALICE with detectors mostly using three-dimensional hit information in a moderate magnetic field. The choice of a low magnetic field allows the reconstruction of low-momentum particles. This

is desirable for several reasons: the study of collective effects related to the presence of the QGP, the measurement of rare process cross sections (like heavy quark production) down to low  $p_T$ , the reconstruction of the decay products of low- $p_T$  hyperons and the selection of the soft conversions and Dalitz decays like  $\pi^0 \rightarrow e^+e^-\gamma$  in the lepton-pair spectrum. The best choice for the field strength corresponds to the maximum field the magnet (the L3 Magnet) can produce,  $B=0.5$  T, because it guarantees a good momentum resolution even at high momenta. Thus, ALICE will run at the highest field most of the time. Nevertheless, a program at lower magnetic field,  $B=0.2$  T, is foreseen since this value corresponds to the maximum reconstruction efficiency at low momentum. A good particle identification system is needed to identify hyperons, vector mesons (e.g.  $\phi \rightarrow K^-K^+$ ), heavy-flavor mesons through their hadronic decays (i.e.  $D^0 \rightarrow K^-\pi^+$ ,  $D^+ \rightarrow K^-\pi^+\pi^+$ ,  $D_s^+ \rightarrow K^-K^+\pi^+$ ) and to carry out analyses with identified particles, like the measurements of azimuthal anisotropies  $v_2$ , particle spectra and ratios, HBT correlations. Hadron identification is performed in the full acceptance of the ALICE central barrel ( $|\eta| \leq 0.9$ ) for all the expected momentum spectra; at higher momenta the particle identification is provided in a restricted acceptance (both in  $\eta$  and  $\varphi$ ) and possibly with reduced momentum resolution.

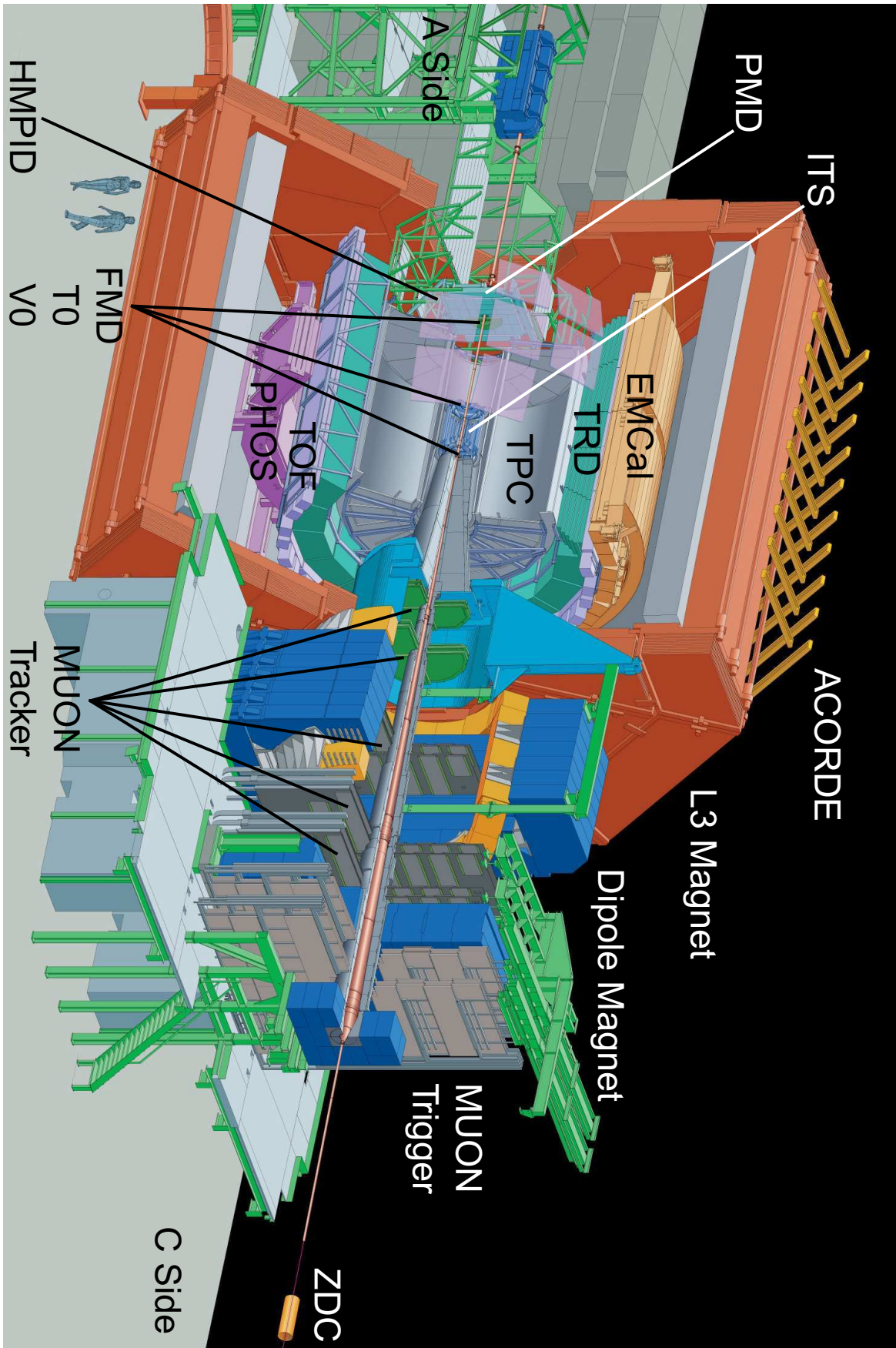


Figure 2.1: 3d Rendering of ALICE.

## 2.2 ALICE setup

The ALICE layout is shown in Fig.2.1 It consists of a central barrel covering the full azimuthal angle in  $|\eta| \leq 0.9$  and several forward systems. The central system is embedded in a magnetic field  $B \leq 0.5T$ . The central detectors are, in the order from the interaction vertex outside, the Inner Tracking System (ITS) with six layers of silicon detectors, the Time Projection Chamber (TPC) which is the main tracking detector, the Transition Radiation Detector (TRD) for electron identification and the Time Of Flight detector (TOF). Two other detectors with smaller acceptance (both in  $\eta$  and  $\varphi$ ) complement the central barrel: the High-Momentum Particle Identification Detector (HMPID) consisting of an array of ring-imaging Cherenkov counters and the Photon Spectrometer (PHOS) which is an electromagnetic calorimeter. The last commissioned detector is the Electromagnetic Calorimeter (EMCal): is located in the central barrel and will be dedicated to the physics of high- $p_T$  photon jets. The Muon Spectrometer is a forward detector located at  $-4 < \eta < -2.5$  made of an absorber with small atomic number  $Z$ , followed by a spectrometer with a dipole magnet, five tracking stations, an iron absorber and two trigger stations. Additional forward detectors are the Forward Multiplicity Detector (FMD) made of silicon strips, the Photon Multiplicity Detector (PMD) made of layers of lead converter and gas proportional chambers and the Zero Degree Calorimeter (ZDC) consisting of two hadronic calorimeters, one for protons and one for neutrons, plus one electromagnetic calorimeter: these detectors provide information on the centrality of the collisions.

Two trigger detectors are located on each side of the interaction point: the V0, made of scintillator detectors, and the T0, consisting of two arrays of Cherenkov counters. The ALICE experimental program includes also a contribution to cosmic-ray physics with the aim of studying high-energy cosmic air showers in the energy range  $10^{15} - 10^{17}$ eV and to study the nature of primary cosmic rays. In order to trigger on them, an array of scintillators (ACORDE) has been installed on the roof of the L3 Magnet.

### 2.2.1 Magnet

The barrel detectors are installed inside the magnet constructed for the L3 experiment at LEP, which produces a weak solenoidal magnetic field ( $B \leq 0.5T$ ). The choice of the magnetic field is driven by the important constraint that it has to be intense enough to provide a momentum resolution at high- $p_T$ , yet to allow the reconstruction of low- $p_T$  particles in the TPC. The lower momentum cut-off which allows the reconstruction of the tracks in the whole TPC is given by  $p_{cut-off} = 0.3BR = 0.2\text{GeV}/c$ , where  $B$  is the magnetic field,  $R = 2.5/2\text{m}$  is

the minimum radius for a particle to traverse the TPC, whose external radius is  $R_{ext} = 2.5$  m.

## 2.3 mid-rapidity Tracking System

### 2.3.1 Inner Tracking System

The Inner Tracking System (ITS)[ITSTDR, PPR06] consists of six cylindrical layers of silicon detectors located in the central barrel at radii,  $r \approx 4, 8, 15, 24, 38$  and  $43$  cm. The innermost radius is the minimum allowed by the presence of the beam pipe, whose radius is  $3$  cm. The outermost radius is determined by the requirement to match tracks from the ITS to the TPC and viceversa. The tasks of the ITS are:

- primary and secondary vertex reconstruction with the high resolution required for the detection of hyperons and particles with open charm and open beauty;
- reconstruction and identification of low momentum tracks with  $p < 100 - 200$  MeV/c, which are too bent by the magnetic field to be reconstructed by the TPC;
- reconstruction and identification of those particles which traverse the dead regions of the TPC;
- improvement of the momentum resolution for the high momentum particles which also traverse the TPC.

With its improvement to the global tracking, momentum and impact parameter resolutions the ITS significantly contributes to the study of several topics, such as multiplicity distributions, particle spectra, resonances, heavy-flavor particles with short lifetime, jet production and jet quenching. Also the particle identification (PID) in the non-relativistic region is necessary because, including in the PID system low-momentum particles with  $p < 100 - 200$  MeV/c, the momentum range where particle spectra are measured is wider and this is important to study collective effects which are usually associated to long distance scale length.

The layout of the ITS is shown in Fig.2.2. Each layer is made of longitudinal supports, the ladders, which host the detectors. The geometrical dimensions, the technology used, the number of channels and the characteristics of the various layers of the ITS are summarized in Tab. 2.1 and Tab. 2.2.

Layer	Type	$r$ (cm)	$\pm z$ (cm)	Area ( $m^2$ )	Ladders	Det./Ladders
1	pixel	3.9	14.1	0.07	80	1
2	pixel	7.6	14.1	0.14	160	1
3	drift	15.0	22.2	0.42	14	6
4	drift	23.9	29.7	0.89	22	8
5	strip	37.8/38.4	43.1	2.09	34	22
6	strip	42.8/43.4	48.9	2.68	38	25

Table 2.1: Dimensions of the ITS detectors (active areas).

Parameter	Silicon Pixel	Silicon Drift	Silicon Strip
Spatial precision $r\varphi$ ( $\mu\text{m}$ )	12	38	20
Spatial precision $z$ ( $\mu\text{m}$ )	100	28	830
Two track resolution $r\varphi$ ( $\mu\text{m}$ )	100	200	300
Two track resolution $z$ ( $\mu\text{m}$ )	850	600	2400
Active area per module ( $\text{mm}^2$ )	12.8 $\times$ 69.6	72.5 $\times$ 75.3	73 $\times$ 400
Readout channels per module	40 960	2 $\times$ 256	2 $\times$ 768
Total number of modules	240	260	1698
Total number of readout channels (k)	9 835	133	2608
Total number of cells (M)	9.84	23	2.6
Average occupancy (inner layer) (%)	2.1	2.5	4
Average occupancy (outer layer) (%)	0.6	1.0	3.3

Table 2.2: Parameters of the various detector types. A module represents a single sensor element.

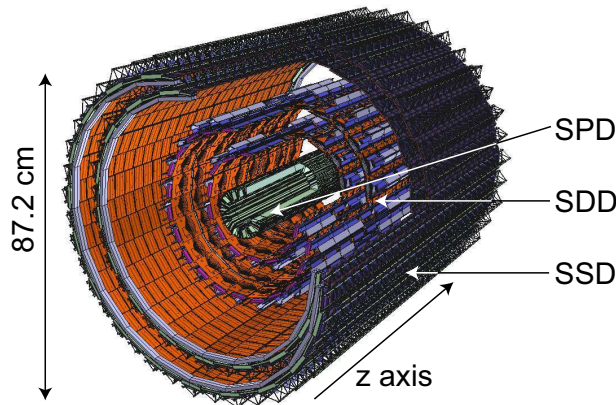


Figure 2.2: Layout of the ITS.

### 2.3.2 Time Projection Chamber

The Time Projection Chamber (TPC)[TPCTDR, PPR06] is the main tracking detector in ALICE: it provides charged-particle track reconstruction, identification, momentum measurements, primary and secondary vertex determination. All these requirements have to be fulfilled at the Pb-Pb nominal luminosity, corresponding to an interaction rate of 8 kHz, of which about 10% are central collisions with impact parameter  $b < 5$  fm. For these it was assumed the extreme multiplicity of  $dN_{ch}/dy = 8000$ , resulting in an unprecedented track density for a TPC. The TPC allows the study of hadronic and leptonic observables with transverse momenta up to  $\sim 100$  GeV/c in the pseudorapidity window  $|\eta| < 0.9$  (for  $p_T$  low resolution up to  $|\eta| < 1.5$ ).

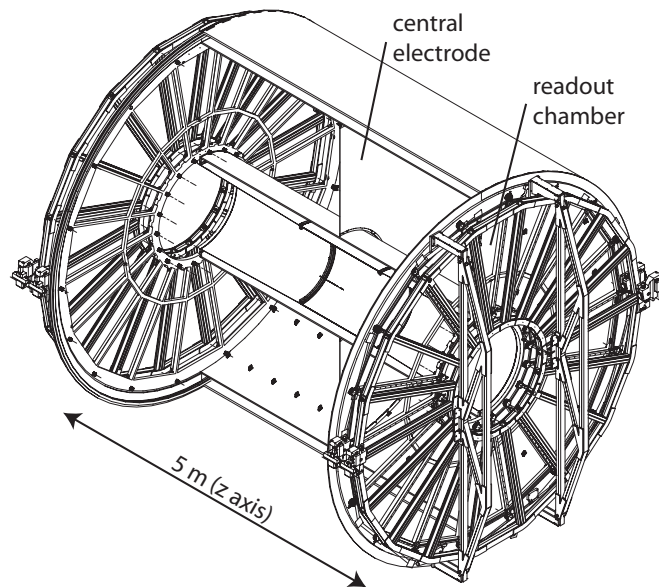


Figure 2.3: Schematic view of the TPC.

### 2.3.3 TPC design considerations

The layout of the TPC is shown in Fig. 2.3 and a synopsis of its main parameters is presented in Tab. 2.3. It has a cylindrical shape with an inner radius of about 85 cm, an outer radius of about 250 cm and an overall length of 500 cm. It is filled with  $88m^3$  of a mixture of  $Ne/CO_2(90\%/10\%)$ ; the field cage is made of an aramidic composite compound with small radiation length because the material budget is kept as low as possible to ensure minimal multiple scattering and secondary particle production.

Pseudo-rapidity coverage	$-0.9 < \eta < 0.9$ for full radial track length $-1.5 < \eta < 1.5$ for 1/3 radial track length
Azimuthal coverage	$2\pi$
Radial position (active volume)	$845 < r < 2466$ mm
Radial size of vessel	$780 < r < 2780$ mm
Length (active volume)	5000 mm
Segmentation in $\varphi$	18 sectors
Segmentation in r	2 chambers per sector
Segmentation in z	central membrane, readout on 2 end-plates
Total number of readout chambers	$2 \times 2 \times 18 = 72$
Inner readout chamber geometry	trapezoidal, $848 < r < 1320$ mm active area
pad size	$4 \times 7.5$ mm ( $\varphi \times r$ )
pad rows	63
total pads	5504
Outer readout chamber geometry	trapezoidal, $1346 < r < 2466$ mm active area
pad size	$6 \times 10$ and $6 \times 15$ mm ( $\varphi \times r$ )
pad rows	$64 + 32 = 96$ (small and large pads)
total pads	$4864 + 5120 = 9984$ (small and large pads)
Detector gas	$Ne/CO_2$ 90/10
Drift length	$2 \times 2500$ mm
Drift field	400 V/cm
Drift velocity	2.84 cm/ $\mu$ s
Maximum drift time	88 $\mu$ s
Total HV	100 kV
Diffusion	$D_L = D_r = 220 \mu\text{m}/\sqrt{\text{cm}}$
Material budget	$X/X_0 = 3.5$ to 5% for $0 <  \eta  < 0.9$
Pad occupancy (for $dN/dy = 8\,000$ )	40 to 15% inner / outer radius
Pad occupancy (for pp)	5 to $2 \times 10^{-4}$ inner / outer radius
Event size (for $dN/dy = 8\,000$ )	$\sim 60$ MB
Event size (for pp)	$\sim 1$ -2 MB depending on pile-up
Data rate limit	400 Hz Pb-Pb minimum bias events
Trigger rate limits	200 Hz Pb-Pb central events 1000 Hz proton-proton events
Position resolution ( $\sigma$ ) in $r\varphi$	1100 to 800 $\mu$ m inner / outer radii
in z	1250 to 1100 $\mu$ m
$dE/dx$ resolution, isolated tracks	5.5%
$dN/dy = 8000$	6.9%

Table 2.3: Collection of TPC parameters.

The TPC material corresponds to about 3.5% of a radiation length. The drawback of  $Ne/CO_2$  mixture is its steep dependence of drift velocity on temperature. For this reason, the TPC is aiming for a thermal stability with  $\Delta T \leq 0.1$  K in the drift volume over the running period.

The potential needed to drift particles is established between a central electrode and the two end caps: the voltage gradients are very high, 400 V/cm, with a high voltage of 100 kV at the central electrode which results in a maximum drift time of about 90  $\mu s$ .

The two end-plates consist of 18 sectors with multi-wire proportional chambers with cathode pad readout: three different sizes of the pads were chosen to keep the occupancy low and to ensure a good spatial and  $dE/dx$  resolution. Usually the readout chambers are closed by a gating grid which prevents ionization electrons coming from the drift region to be collected; they are opened only by the L1 trigger (6.5  $\mu s$  after the collision) for the duration of one drift-time interval[TPCTDR].

The TPC readout chain has been designed to be able to transfer 200 central or 400 minimum-bias Pb-Pb events per second for the extreme multiplicity case. The recorded data volume can be reduced with the “region-of-interest” option of the trigger, reading out only a few sectors of the TPC. Moreover, the High Level Trigger will help to increase the statistics for rare signals like dielectron pairs selecting only those particles identified as electrons by the TRD.

## 2.4 Particle identification system

Particle identification is one of the key points in the ALICE experiment. Besides the TPC and the ITS, using the  $dE/dx$  technique, there are detectors specifically built to this purpose: the TOF provides identification of charged particles in the intermediate momentum range where most particles are produced, the TRD identifies electrons with momentum above 1 GeV/c and the HMPID is able to separate hadrons of higher momentum, up to  $\sim 5$  GeV/c.

### 2.4.1 Transition-Radiation Detector (TRD)

The Transition-Radiation Detector (TRD)[TRDTDR, PPR06] provides electron identification in the momentum region above 1 GeV/c where the identification through ionization energy loss made by the TPC is no more efficient. This is necessary to measure the production of  $J/\psi$  and  $\Upsilon$  in their dielectron channel rejecting the background given by Dalitz decays. Furthermore, using the information of the TRD together with the impact-parameter determination in the ITS, it is possible to study mesons with open charm and open beauty via their semi-leptonic decays.

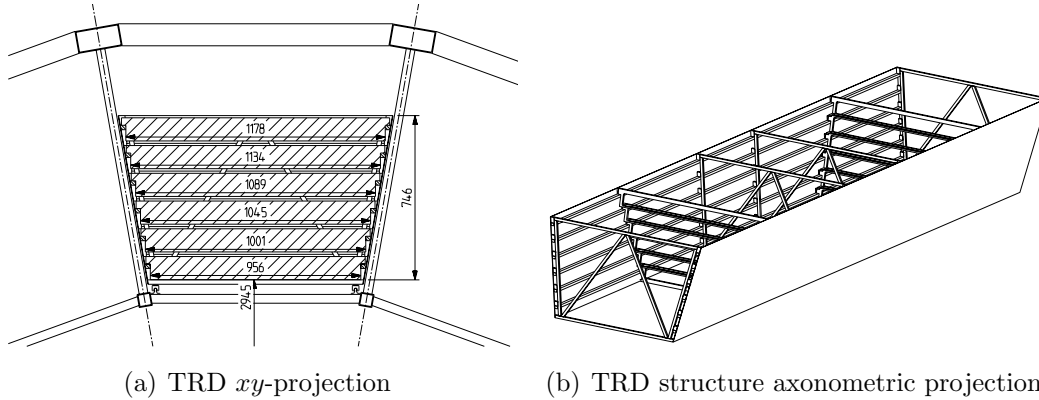


Figure 2.4: TRD

The TRD is composed of several modules, each consisting of a radiator where x-rays are emitted by charged particles per boundary crossing, and a multi-wire proportional readout chamber which detects the x-rays. This detector is useful for particles with Lorentz factor  $\gamma$  larger than 1000, which in practice corresponds to good electron/pion separation for momenta  $1 \leq p \leq 100$  GeV/c.

### 2.4.2 Time-Of-Flight Detector (TOF)

The TOF detector [TOF00, PPR06] of ALICE covers the central pseudorapidity region ( $|\eta| < 0.9$ ) and plays an fundamental role in the identification of pions, kaons and protons in the intermediate momentum range. This detector will be described further in Chapter 3.

### 2.4.3 High-Momentum Particle Identification (HMPID)

The HMPID [PPR06] identifies hadrons with momenta larger than 1 GeV/c and thus enhances the PID capabilities of ALICE by extending the limited momentum region where particles can be identified through energy loss (in ITS and TPC) and time-of-flight measurements (in TOF). It allows a good separation  $\pi/K$  and  $K/p$  on a track-by-track basis up to 3 GeV/c and 5 GeV/c respectively.

The technology chosen for such purposes is the Ring-Imaging Cherenkov (RICH) consisting of seven modules of about  $1.5 \times 1.5 m^2$  each, mounted on a cradle fixed to the space frame occupying 3 out of the 18 sectors of the barrel and at a distance of  $\sim 4.5$  m from the center of interaction. The acceptance is only 5% of the central barrel detectors (Fig. 2.5). The radiator is a thick layer of  $C_6F_{14}$  (perfluorohexane) with an index of refraction  $n = 1.2989$  at  $\lambda = 175$  nm, corresponding to a momentum threshold of  $p_{th} = 1.21 \times m$  where  $m$  is the particle mass in GeV/c<sup>2</sup>. When a

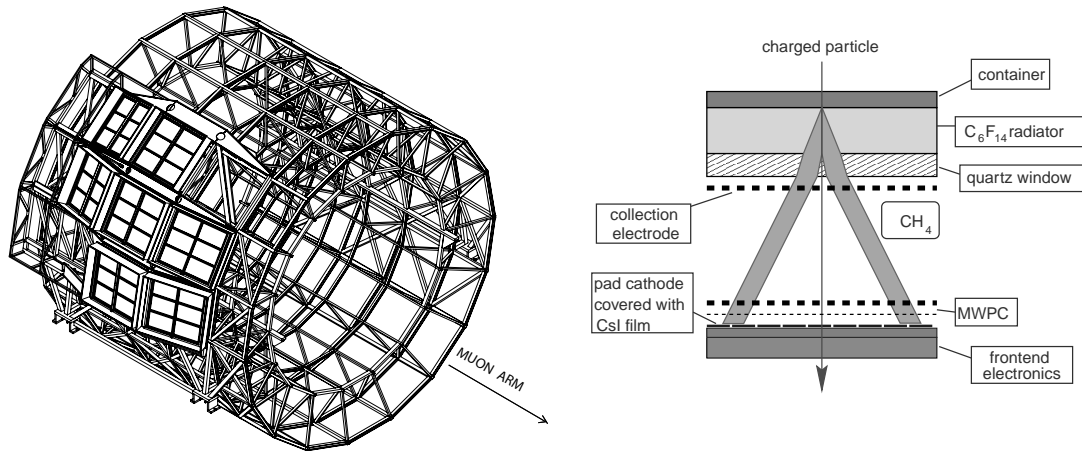


Figure 2.5: hmpid

particle crosses the radiator with a velocity larger than the light velocity in the same medium, it emits Cherenkov photons which are detected by a photon counter made of CsI located on the pad cathode of a Multi-Wire Pad Chamber (MWPC). The working principle of the RICH detector is shown in Fig. 2.5. HMPID is the largest RICH ever employed up to now.

#### 2.4.4 Photon Spectrometer (PHOS)

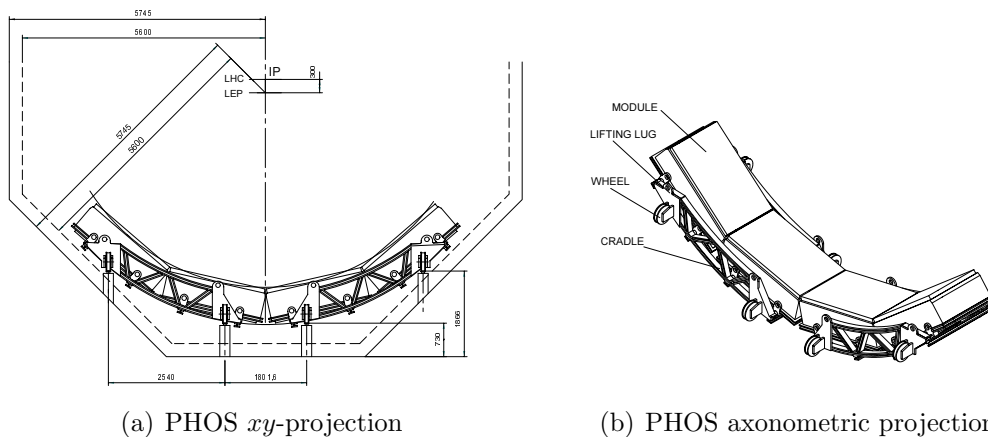


Figure 2.6:

The PHOS[PHOSTDR, PPR06] is a high resolution electromagnetic calorimeter dedicated to the detection of photons directly coming from the interaction point

and neutral mesons (e.g.  $\pi^0$ ) decaying in two photons. Since the main task of the detector is to distinguish between direct photons and photons coming from particle decays, it has to be characterized by a high granularity and good space and energy resolution. The segmentation must be below the Molière radius<sup>1</sup> of the material. The calorimeter is made of lead tungstate crystals, PbWO, grouped in five modules; this material has a Molière radius equal to 2 cm. The PHOS is located at 460 cm from the interaction point and covers the pseudorapidity region  $-0.12 \leq \eta \leq 0.12$ , and an azimuthal angle of  $100^\circ$ . Its total area is  $\sim 8m^2$ .

### 2.4.5 Electromagnetic Calorimeter (EMCal)

The main physics motivation for the EMCal[EMCTDR] is to improve the ALICE performances for an extensive study of jet quenching: in fact the EMCal extends the ALICE  $p_T$  capabilities for jets, direct photons and electrons from heavy-flavor decays.

The detector contains several modules each consisting of sampling calorimeters made of alternating layers of 1.44 mm Pb and 1.76 mm polystyrene, which is the scintillating material. The EMCal covers the pseudorapidity range  $-0.7 \leq \eta \leq 0.7$  and  $110^\circ$  in  $\varphi$ . It is positioned to provide partial back-to-back coverage with the PHOS and its nominal acceptance is about 25% of the TPC acceptance.

### 2.4.6 Forward Muon Spectrometer

The forward muon spectrometer [MUOTDR] will allow the study of resonances like  $J/\psi, \psi', \Upsilon, \Upsilon'$  and  $\Upsilon''$  through their decay into  $\mu^+ \mu^-$  pairs, and to disentangle them from the continuum given by Drell-Yan processes and semi-leptonic decays of  $D$  and  $B$  mesons. It will also be interesting the study of open heavy flavor production with the muon spectrometer, accessible through measurements of  $e - \mu$  coincidences, where the muon is detected by the muon spectrometer and the electron by the TRD. A resolution of  $70 \text{ MeV}/c^2$  in the  $3 \text{ GeV}/c^2$  region is required to resolve  $J/\psi$  and  $\psi'$  peaks and of  $100 \text{ MeV}/c^2$  in the  $10 \text{ GeV}/c^2$  region to separate the  $\Upsilon$  family. This detector is located around the beam pipe and corresponds to the pseudorapidity range  $-4.0 \leq \eta \leq -2.5$ . It consists of a passive front absorber to absorb hadrons and photons from the interaction vertex. The material must have a small interaction

<sup>1</sup> The Molière radius is a constant describing the electromagnetic characteristics of the material:

$$R_M = 0.0026 X_0 (Z + 1.2),$$

where  $X_0$  is the radiation length and  $Z$  is the atomic number.  $R_M$  is related to the transverse dimension of the electromagnetic shower in the calorimeter, thus the smaller is  $R_M$ , the better is the capacity of the calorimeter to contain the shower.

length in order to absorb hadrons and a large radiation length, in order to reduce multiple scattering.

Muon tracks are then reconstructed by tracking chambers consisting of multi-wire proportional chambers with cathode pad readout. They are embedded in a magnetic field generated by a dipole magnet located outside the L3 magnet. The trigger on dimuon signals is done by four layers of RPC operating in streamer mode located behind a second absorber.

### 2.4.7 Forward rapidity detectors

To complete the experimental apparatus there are detectors located at small angles with respect to the beam axis.

The **Zero-Degree Calorimeter (ZDC)**[ZDCTDR] measures the energy of the spectator nucleons and thus provides information on the centrality of the collision: in fact, the zero degree forward energy decreases with increasing centrality. Furthermore, the ZDC allows to perform flow analyses because it can estimate the reaction plane through the directed anisotropy (see 1.3.1). The ZDC consists of two calorimeters, one for neutrons and one for protons. Two ZDCs are symmetrically installed with respect to the interaction point, at a distance of 116 m from the interaction point. The adopted technique for this detector is to alternate a dense absorber (passive material), where incident particles originate showers, and quartz fibers (active material), where the showers produce Cherenkov radiation. Because of the incomplete fragmentation of the spectator nucleons, the correlation between the ZP (proton calorimeter) and the ZN (neutron calorimeter) is not enough to determine the centrality of the collision. Thus, the ZDC includes also an electromagnetic calorimeter (ZEM) to solve the ambiguity due to fragment production. The ZEM is designed to measure, event by event, the energy of photons emitted at forward from  $\pi^0$  decays.

The **Photon Multiplicity Detector (PMD)**[PMDTDR] measures the multiplicity and the spatial distribution of photons on an event-by-event basis in the forward region of ALICE. It consists of two planes of gas proportional counters having a honeycomb structure with a thick lead converter in between them. The PMD is placed at 360 cm from the interaction point, on the opposite side of the forward muon spectrometer, covering the region  $2.3 \leq \eta \leq 3.7$ .

The **Forward Multiplicity Detector (FMD)**[FDTDR] provides information on the charged-particle multiplicity and consists of five rings of silicon strip

detectors, two of which are installed on the muon absorber side in the pseudorapidity region  $-3.4 \leq \eta \leq -1.7$ , while the remaining three are located on the opposite side of the interaction point, in the  $1.7 \leq \eta \leq 5.1$  region. With this detector will be possible to extend the pseudorapidity coverage of multiplicity measurements, to study multiplicity fluctuations on an event-by-event basis and to perform flow analyses.

The **T0 detector**[FDTDR], made of 24 Cherenkov radiators, generates the T0 signal for the TOF detector with a precision of  $\sim 50$  ps, measures a rough vertex position, provides a first level trigger and helps to discriminate against beam-gas interactions.

The **V0 detector**[FDTDR], consisting of scintillators, provides a minimum bias trigger for the central barrel detectors and can be used as a centrality indicator. Both the T0 and V0 consist of two modules installed on each side of the interaction point.

## 2.5 Trigger and Data acquisition

### 2.5.1 Trigger system

The trigger system[CSTDR] in ALICE is studied to be able to select events with different features depending on the physical interests and must be optimized to work both in nucleus-nucleus and pp collisions. The trigger includes three levels (L0, L1 and L2) and the so called High Level Trigger (HLT). The trigger system is monitored by the Central Trigger Processor (CTP) which receives inputs from the trigger detectors and sends decisions to the other detectors for the data acquisition.

The first trigger input is the “TRD pre-trigger” consisting of signals from TOF, T0 and V0 detectors which are sent to the TRD in less than 100 ns after the collision, in order to wake-up the TRD electronics, which otherwise would be in a standby state. The Level 0 (L0) trigger is sent to the detectors at  $1.2 \mu\text{s}$ : the latency of this fast signal is due both to the time required by the electronics to elaborate the signal ( $\mathcal{O}(50\text{ns})$ ) and to the time needed to propagate through the cables (order of  $\mu\text{s}$ ). The latency is common and independent from the triggering input. In this way an estimate of the time of the collision is provided by the machine collision phase.

The L0 signal is too fast to be able to receive all the trigger inputs, therefore a Level 1 (L1) signal is sent at  $6.5 \mu\text{s}$  to pick up all remaining inputs. If the L1 decision reaches the fast detectors, they start the data conversion and bufferization on a temporary ring memory. The latency of L1 ( $\sim 5.5\mu\text{s}$ ) has been chosen to allow the bufferization of the SDD of the ITS, whose drift time is of the order of  $5 \mu\text{s}$ .

The third trigger level (L2) fulfills the request to avoid piled-up events. The event pile-up will be frequent and in some cases unavoidable in ALICE, because of the slow detectors in ALICE and the high luminosity reached with the LHC. The TPC is the slowest detector with a drift time of  $88\mu\text{s}$  and thus it will be affected by pile-up: it may indeed happen either that in the TPC there are still the drift charges of the previous event when the interesting event is coming, or that a subsequent event is triggered before the interesting one has been registered. In order to avoid such a problem, the Central Trigger Processor makes use of the past-future protection, which rejects any other event occurring within a specified time window. The time window is set equal to the sensitive window for the TPC,  $\pm 88\mu\text{s}$  centered on the event under consideration: if two events are separated by less than  $88\mu\text{s}$ , their pile-up is unavoidable.

In Pb-Pb collisions, the past-future protection accepts no more than 4 additional peripheral events and no additional semi-central events to take place in an interval of  $176\mu\text{s}$  centered on the interesting event. In case of proton-proton collisions, given the increased luminosity, the pile-up becomes a certainty; nevertheless, if it is possible to distinguish multiple event vertexes, the pile-up is more tolerable because the multiplicities are much lower than in nucleus-nucleus interactions. The approach adopted in this case is to control with the past-future protection not only the TPC but also the other detectors: for example, the pile-up in the ITS is serious for the reconstruction of primary vertex. Therefore, the past-future protection checks two different time windows ( $\pm 10\mu\text{s}$  for the ITS, whose drift detectors have a drift time of  $\pm 5\mu\text{s}$ , and  $\pm 88\mu\text{s}$  for the TPC), to ensure that pile-up is not excessive. The L2 trigger waits for the end of the past-future protection interval to verify that the event can be registered. When the CTP sends the L2 decision the event is ready to be transferred to the Data Acquisition system (DAQ).

The L0 and L1 trigger levels may also include signals coming from detectors specific for certain analyses, like the Muon Spectrometer, the TRD, the PHOS and the EMCal. The trigger given by Muon Spectrometer is used to select only those events containing a pair of muons with  $p_T$  above a given threshold. The trigger given by the TRD allows the selection of events containing high- $p_T$  electron pairs or jets. Finally, with the PHOS and the EMCal it is possible to trigger events with photon jets, with photons plus jets, and with very high- $p_T$  jets.

At the nominal luminosity of  $10^{27}\text{cm}^{-2}\text{s}^{-1}$  the interaction rate will be 8000 Hz for Pb-Pb: with such conditions, the maximum total rates of the different trigger levels will be of 1300 Hz and 1100 Hz for L0 and L1 respectively. These numbers are reduced in case of additional selections on centrality or if dimuon event candidates are required. The L2 rate using the TPC for triggering on minimum bias events will be 40 Hz. The rates can be reduced applying downscaling factors.

## 2.5.2 Data Acquisition (DAQ) System

The main functions of the DAQ system[CSTDR] are the following:

- data transfer from the front-end electronics to the control room; this is done in parallel for all the sub-detectors. The transfer is initiated by the L2 trigger;
- event building, performed by the Global Data Collectors (GDC);
- archive data to mass storage Permanent Data Storage (PDS).

The estimated bandwidth to mass storage is 1.25 GB/s, even though the aggregate bandwidth of readout data from the detector is  $\sim 25$  GB/s.

According to simulation results, the event size of Pb-Pb collisions is rather big:  $\sim 86.5$  MB for central events, 50% and 25% of that size for semi-central and minimum bias events respectively. ALICE DAQ is designed to cope with the event sizes resulting from heavy-ion collisions by using a combination of increased trigger selections and data compression.

## 2.5.3 High-Level Trigger (HLT)

As a multi-purpose experiment, ALICE searches for a large number of probes such as open charm and beauty, quarkonia, direct photons, jets, correlations. Since most of the probes are rare signals, it is necessary to exploit all the data collected with a collision rate of 8 kHz for Pb-Pb. It may happen that the remaining data rate after the three trigger levels are still high to be transferred to the permanent storage system. The HLT[CSTDR] works online to reduce such data rate by improving particle identification and momentum resolution, or by selecting regions of interest like jet regions, or by filtering out low momentum tracks in the TPC. The HLT system is located in the data flow between the front-end electronics and the event building of the DAQ system.

## 2.6 LHC Machine complex

Whether ALICE will reach its physics goals will depend not only on the performance of the detectors, but also on the statistics available. The number of collected events depend on the nature of the beam, on the luminosity and on the running time.

Like the SPS and RHIC programs, the heavy-ion program at LHC will be based on colliding both the largest available nuclei at the highest energy, and different collision systems (pp, pA, AA) with various energies.

The “standard” LHC yearly program will consist of several months of pp running

followed at the end of each year by several weeks of heavy-ion collisions. The effective running time per year is foreseen to be  $\sim 10^7$ s for protons and  $\sim 10^6$  heavy ions. ALICE in 2009 started its data taking with pp collisions as well as every other main experiments at LHC. At the end of the first long pp run, a Pb-Pb run is foreseen in 2011.

This first Pb-Pb run will allow studies on global event properties and on large cross section observables; in order to study low cross section signals, in particular hard processes such as those containing charm and beauty, further 1-2 years of Pb-Pb will be required in order to collect enough statistics. The ALICE program is related to the LHC one and is summarized below:

- regular pp collisions at center-of-mass energy of  $\sqrt{s} = 14$  TeV;
- first Pb-Pb short run (pilot run);
- 1-2 years of Pb-Pb at  $\sqrt{s} = 5.5$  TeV per nucleon pair;
- 1 year of pA-like collisions (pPb, dPb,  $\alpha$ Pb);
- 1-2 years of Ar-Ar.

The program includes pA runs because pA collisions allow to determine nuclear modifications on the parton distribution functions (nuclear shadowing). The study of Ar-Ar collisions has been proposed to study how the energy density varies with the mass of the collision systems. Additional Pb-Pb runs at lower energies are also foreseen in order to connect LHC results with those from RHIC. The LHC will collide protons at the maximum energy of  $\sqrt{s} = 14$  TeV; this puts a constraint on the maximum center-of-mass energy for heavy-ion collisions. Since only charged particles are accelerated, the  $Z$  protons inside a nucleus will drag the  $A - Z$  neutrons, resulting in an average momentum of the nucleons of  $p \cdot Z/A$ , where  $p$  is the momentum of the protons in the proton beam case. Considering two colliding nuclei, the center-of-mass energy per nucleon pair  $s_{NN}$  is therefore given by:

$$s_{NN} = \left( \frac{Z_1}{A_1} p_1 + \frac{Z_2}{A_2} p_2 \right)^2 = 2 \frac{Z_1}{A_1} \frac{Z_2}{A_2} p_2 p_1 \quad E \gg m \quad (2.1)$$

where  $Z$  and  $A$  are the atomic and mass numbers for the two ions and  $p$  is the four-momentum in the proton beam case. Since in the above approximation ( $E \gg m$ ) the center-of-mass energy for the proton pair is  $s_{pp} = 2p_2 p_1$ , considering Pb ions with  $Z_1 = Z_2 = 82$  and  $A_1 = A_2 = 208$ , a value of  $\sqrt{s_{NN}} = 5.5$  TeV is obtained. In the 2010 run the foreseen pp center-of-mass energy is 7 TeV, corresponding to a  $\sqrt{s_{NN}} = 2.8$  TeV.

### 2.6.1 Luminosity determination

The luminosity  $\mathcal{L}$  is a parameter of the accelerating machine relating the process rate  $R$  to its cross section  $\sigma$ :

$$R = \mathcal{L} \cdot \sigma$$

In case of two colliding beams (i.e. LHC), the luminosity is given by the following relation:

$$\mathcal{L} = f N_b \frac{N^2}{4\pi\beta_x\beta_y} F \quad (2.2)$$

where  $f$  is the revolution frequency,  $N_b$  the number of bunches,  $N$  the number of particles per bunch. The quantity  $4\pi\beta_x\beta_y$  indicates the transverse area of the two bunches in the interaction point; it is calculated assuming a Gaussian distribution of the transverse spot of the two beams with horizontal and vertical standard deviations  $\beta_x$ , and  $\beta_y$  respectively. The factor  $F$  is related to the finite crossing angle of the beams and depends on the ratio between longitudinal and transverse beam sizes.

The TOTEM experiment[Kie99] will measure the total pp cross section at LHC. In ALICE only a fraction of the rate of inelastic pp cross section is measured ( $R = a \cdot R_{tot}$  where  $a$  is the detector acceptance); the luminosity is then given by:

$$\mathcal{L} = \frac{R}{a \cdot \sigma_{inel}} \quad (2.3)$$

The total pp cross section ( $\sigma \sim 100$  mb) is the sum of the elastic ( $\sigma_{el} \sim 28$  mb) and inelastic events ( $\sigma_{inel} \sim 72$  mb). One possible way to monitor the luminosity in Pb-Pb runs with ALICE is to measure the total hadronic cross section, mainly given by the geometry of the collision and known with an accuracy better than 10%. Measuring the hadronic interaction rate, the luminosity is then  $\mathcal{L}_{had} = R_{had}/\sigma_{had}$ .

### 2.6.2 ALICE luminosity constraints

**Pb-Pb collisions** The luminosity for Pb-Pb collisions is given by the accelerating machine. The maximum rate is limited by the ALICE detectors, mainly by the TPC and the Forward Muon Spectrometer. The TPC limits the sustainable rate because of event pile-up during the 90  $\mu$ s drift time; another constraint comes from the RPC of the muon spectrometer, which has a maximum acceptable illumination of  $50 Hz cm^{-2}$ . The maximum expected value for the luminosity in Pb-Pb is  $10^{27} s^{-1} cm^{-2}$ . The total hadronic cross section is 8 b, thus the expected rate is  $\sim 8$  kHz, 10% of which are central. The trigger rate, as discussed in §2.5.1, is lower than 8kHz.

**pp collisions** In order to keep the event pile-up at an acceptable level in the TPC and in the SDD, the luminosity has to be limited to  $\sim 5 \times 10^{30} \text{cm}^{-2} \text{s}^{-1}$ , corresponding to an interaction rate of  $\sim 200$  kHz. Thus, the luminosity has to be reduced comparing to the dedicated high-luminosity LHC experiments where  $\mathcal{L} \sim 10^{34} \text{cm}^{-2} \text{s}^{-1}$ .

## 2.7 Radiation damage

The radiation dose on the various detectors of ALICE depends on the beam type, on the luminosity and on the running time. The main sources of radiation in ALICE are the following[Mor02]:

- particles produced at the interaction point;
- beam losses due to mis-injection: ALICE will receive such radiation because it is placed near the injection point in the beam pipe;
- beam-gas interactions.

The major contribution comes from the interaction point; beam losses and beam gas interactions contribute 1% and 10% respectively to the total radiation fluency. In Table 2.4 a typical scenario for ten years of LHC operation is presented. The last line, showing the total number of charged particles, suggests that 80% of the radiation dose is from pp and High-luminosity ArAr interactions. Another possible source of radiation is thermal neutrons. They come from scatterings of highly energetic neutrons largely produced through hadronic cascades in the ALICE absorbers. According to the present estimates, each minimum bias event produces approximately 50 thermal neutrons per  $\text{m}^2$  at a distance of 5 m from the interaction point.

Table 2.4: Operation scenario for a ten-year run period.

	pp	Ar-Ar	High- $\mathcal{L}$ Ar-Ar	Pb-Pb	d-Pb
$\langle \mathcal{L} \rangle (cm^{-2}s^{-1})$	$3 \times 10^{30}$	$3 \times 10^{27}$	$10^{29}$	$10^{27}$	$8 \times 10^{28}$
$\sigma_{incl} (mb)$	70	3000	3000	8000	2600
Runtime (s)	$10^8$	$10^6$	$2.0 \times 10^6$	$5.0 \times 10^6$	$2.0 \times 10^6$
Rate ( $s^{-1}$ )	$2 \times 10^5$	$9 \times 10^3$	$3 \times 10^5$	$8 \times 10^3$	$2 \times 10^5$
Events	$2 \times 10^{13}$	$9 \times 10^9$	$9 \times 10^9$	$4 \times 10^{10}$	$4 \times 10^{11}$
$E_{beam}$	7 TeV	3.2 TeV/A	3.2 TeV/A	2.8 TeV/A	2.8 TeV/A–7 TeV
$N_{ch}$ per event	100	2400	2400	14200	500
$N_{tot}$	$2.1 \times 10^{15}$	$2.2 \times 10^{13}$	$1.4 \times 10^{15}$	$5.7 \times 10^{14}$	$2 \times 10^{14}$

# Chapter 3

## The Time-Of-Flight Detector

In the previous chapter I showed the advantage for a relativistic heavy ion experiment to make use of a large detector array for particle identification (PID): the ALICE detector hosts a large TOF in the central rapidity region. Since most of the particles generated in a QGP reaction are within the intermediate momentum range<sup>1</sup>, the TOF will be essential to measure particle ratios and particle spectra for single species on an event-by-event basis and to study the invariant masses with identified particles, e.g.  $D^0 \rightarrow K^- \pi^+$  or  $\phi \rightarrow K^+ K^-$  [Aki06].

### 3.1 Time-Of-Flight technique

The ALICE TOF is located at 3.7 m from the beam axis and covers the  $|\eta| \leq 0.9$  range with full azimuthal acceptance; the active area is 141 m<sup>2</sup>. With a magnetic field of 0.5 T, the momentum threshold for this detector, calculated only from geometrical constraints, is  $p = 278 \text{ MeV}/c$ . Taking into account the material budget, according to a MonteCarlo simulation, the momentum threshold is  $\sim 300 \text{ MeV}/c$  for  $\pi^\pm$ ,  $\sim 350 \text{ MeV}/c$  for  $K^\pm$  and  $\sim 450 \text{ MeV}/c$  for protons and antiprotons. Assuming a global TOF resolution of 80 ps, the separation between particles at  $3\sigma$  is achieved up to 2.5 GeV/c for  $\pi/K$  and 4 GeV/c for  $K/p$ .

The Time-Of-Flight technique consists in measuring the  $\beta$  factor of a particle by the independent measurements of the length of the trajectory and its time of flight [Leo94]; with the momentum information available it is possible to obtain an indirect measure of the mass of the particle. A particle of momentum  $p$ , moving on a trajectory of length  $L$  with a time-of-flight  $t$  has a mass:

$$m = p \sqrt{\frac{t^2}{L^2} - \frac{1}{c^2}}. \quad (3.1)$$

---

<sup>1</sup> the 97% of the charged particles produced in a QGP reaction has momentum  $p < 2 \text{ GeV}/c$

It is possible to compute the contributions to the error on the mass deriving from Eq. 3.1 for every measured entity in the equation

$$\frac{\delta m}{m} = \frac{\delta p}{p} \quad (3.2)$$

$$\frac{\delta m}{m} = \left(\frac{E}{m}\right)^2 \frac{\delta t}{t} \quad (3.3)$$

$$\frac{\delta m}{m} = \left(\frac{E}{m}\right)^2 \frac{\delta L}{L}. \quad (3.4)$$

It is clear that the contributions relative to the length of the trajectory and to the time of flight are dominant when  $E \gg m$ . Considering two particles of mass  $m_1$  and  $m_2$  and the same momentum  $p$ , the difference of time of flight is

$$\Delta t \sim \frac{L}{2c} \frac{(m_1^2 - m_2^2)}{p^2} \quad \text{if} \quad \frac{m_{1,2}^2}{p^2} \ll 1 \quad (3.5)$$

where  $L$  is the length of the trajectory. To assess the capability of the TOF detector one can quantify the separation in standard deviations as

$$n_{L,m_{1,2}} = \frac{\Delta t}{\sigma} = \frac{L(m_1^2 - m_2^2)}{2p^2 c \sigma} \quad (3.6)$$

where  $\sigma$  is the time resolution. Fig. 3.1 shows the separation from Eq. 3.6 for particles traversing perpendicularly a magnetic field  $B=0.5$  T in the  $e/\pi$ ,  $\pi/K$ ,  $K/p$  and  $p/d$  case.

## 3.2 The Detector

The Time-Of-Flight detector of the ALICE experiment is designed with a highly modular architecture, based on a detector element: the Multigap Resistive Plate Chambers (MRPC) strip. Though a time resolution better than 100 ps is achievable with scintillators and photomultiplier systems, this solution is economically unsustainable for a detector with a large active area ( $\sim 150\text{m}^2$ ). In the framework of the LAA project at CERN an intensive R&D work was carried out to develop a gaseous detector combining the high efficiencies of large-gap resistive plate chambers (RPCs) with the time resolution of small-gap RPCs. The idea developed in this process is sketched in Fig. 3.2, the MRPC is basically a large gap RPC with the gap divided into several small gaps.

Resistive plate chambers are ionization chambers in a parallel plate geometry with a constant electric field applied by means of resistive electrodes. If the electric field is strong enough, an electron from primary ionization can acquire sufficient

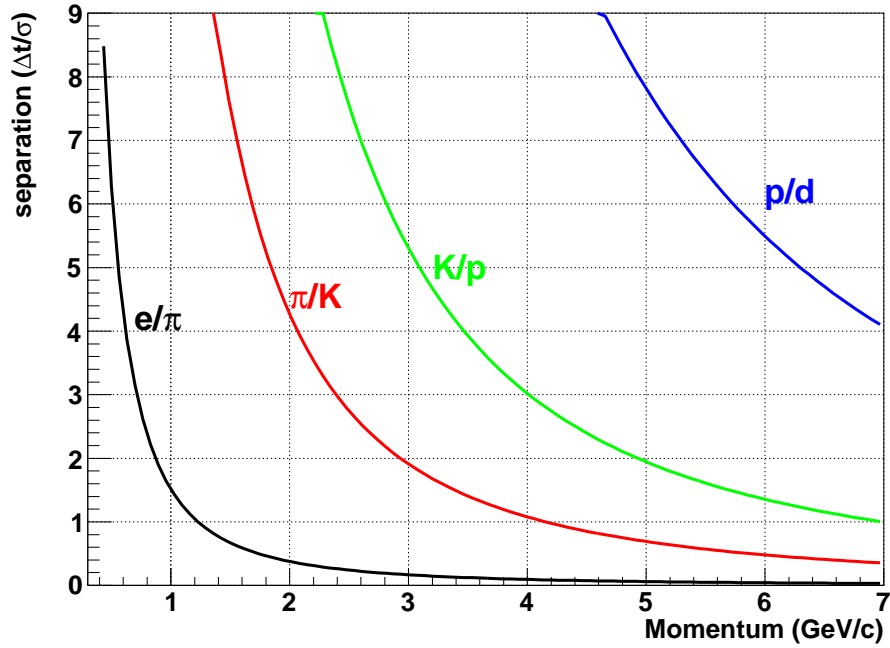


Figure 3.1: Separation for  $e/\pi$ ,  $\pi/K$ ,  $K/p$  and  $p/d$  in the shortest path from interaction point to the TOF.

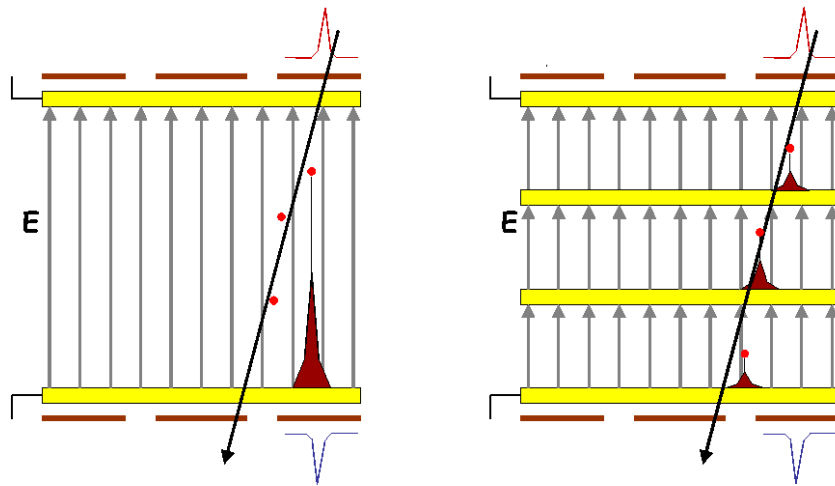


Figure 3.2: A schematical diagram of an RPC (Left) and a Multigap RPC (Right).

momentum to create a second ionization pair, thus an avalanche multiplication. In the active region a large number of charged ions and electrons are created and they move according to the external electric field, inducing a signal on pick-up pads close

to the electrodes.

### 3.2.1 Time signal from an RPC

The uncertainties on the time signal formation in a general RPC design depends mainly on two factors: fluctuations on the avalanche development and fluctuations on the primary electron–ion pair.

As demonstrated in [Man02] and [Rie03], the time fluctuations induced on the pads are a function of gas characteristics and the electric field following the relation

$$\sigma_t \approx \frac{1.3}{(\alpha - \eta) v_D} \quad (3.7)$$

where  $\alpha$  is the Townsend coefficient (i.e. the inverse of the mean free path for electrons in the active volume),  $\eta$  is the attachment coefficient which is the inverse of a mean free path for a electron–ion recombination or a electron–atom capture, while  $v_D$  is a the drift velocity of an electron in the electric field.

Considering these aspects, a request on the time resolution better than 50 ps implies a large electric field and a mixture of gas, with large  $v_D$  and Townsend coefficients.

### 3.2.2 The Multigap RPC technology

Since the drift velocity and the effective Townsend coefficient grow linearly with the electric field, then good time resolution implies the use of a gas mixture with large drift velocity (like Freon) and a large electric field.

Timing RPC are built with small gap ( $\sim 0.3mm$ ) and use a highly electronegative freon-based mixture. This allows to have good time resolution, but the detection efficiency is not satisfactory.

Fig. 3.4 and Fig. 3.5 show the drift velocity and Townsend coefficient as a function of the electric field for different gas mixtures the former and for the gas mixture used in ALICE TOF MRPC the latter.

The MRPC concept has been developed[Cer96] to solve the issue on the efficiency. The superimposition of several gaps has several advantages:

**Signal shape:** since the signal is roughly the sum of each contribution, the spectrum for a small–gap RPC is shown in Fig. 3.6(b) as a reference. The result of summing the contributions of each gaps is a clear peak on the charge spectrum of an MRPC (Fig. 3.6(a)).

**Efficiency:** the efficiency is enhanced due to the overall gas thickness (in ALICE-TOF MRPC there are 10 gaps of 250  $\mu m$  corresponding to 2.5 mm of total gas thickness.)

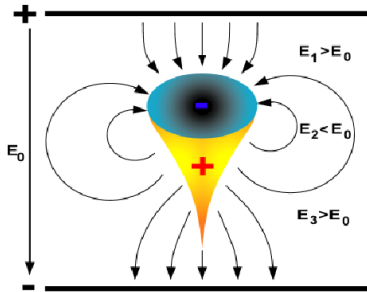


Figure 3.3: Diagram illustrating the spatial charge effect.

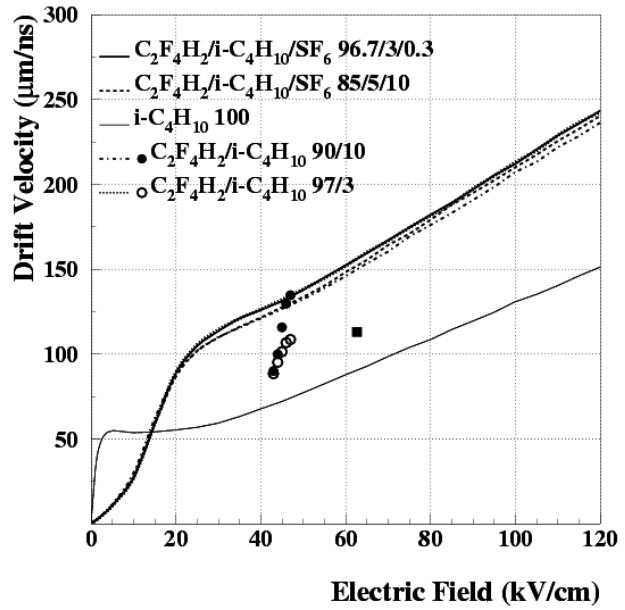


Figure 3.4: Drift velocity as a function of the electric field applied.

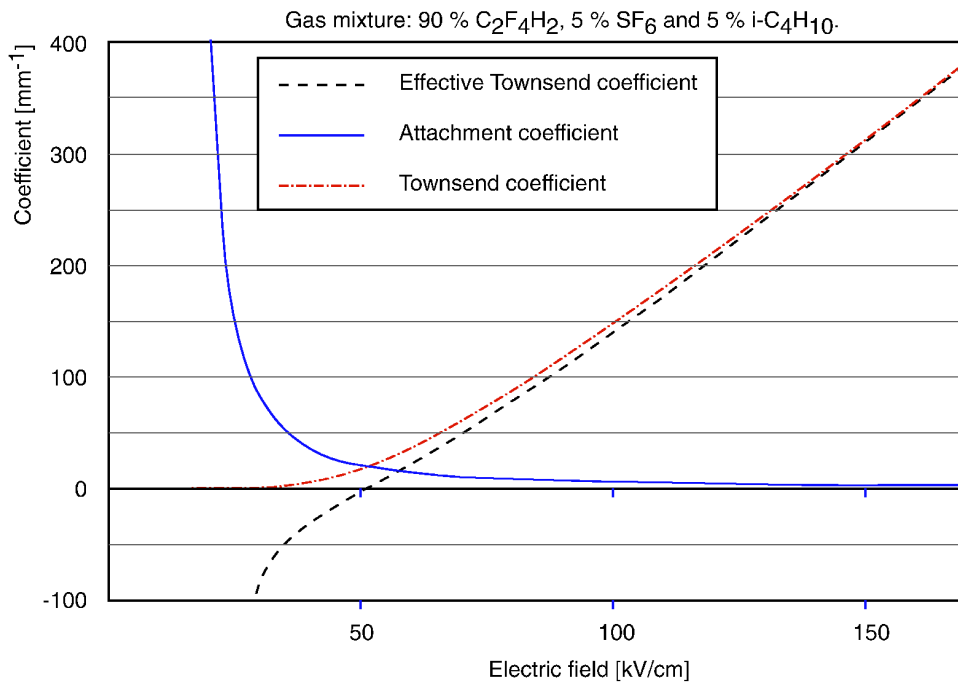
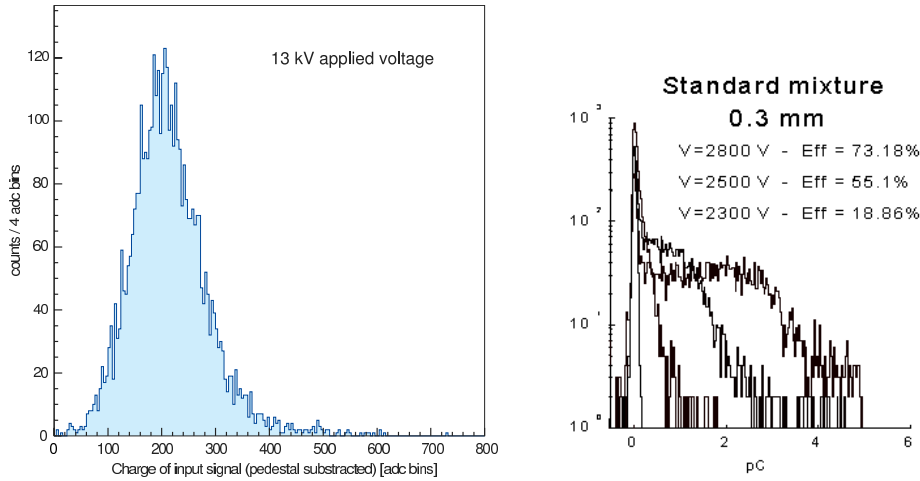


Figure 3.5: Townsend and attachment coefficients as function of the electric field applied; the effective Townsend coefficient is the difference between them.

**Space charge:** as seen in single gap RPC, the multiplication factor is disfavoured with respect to the predicted one ( $\propto e^{\alpha_{eff}d}$ ). Due to space charge effects, sketched in Fig. 3.3, an MRPC works in a streamer free regime even with large effective Townsend coefficient[Aki03].

**Ageing:** as a consequence of the avalanche mode, MRPCs are not affected by ageing for a equivalent 15 years dose in the ALICE environment[Aki04b].

The gas mixture used is  $C_2F_4H_2/SF_6/i-C_4H_{10}$  in percentages 90%/5%/5% or 93%/7%/0% with comparable performance.



(a) Analog to Digital spectrum for a MRPC strip (pedestal is subtracted). (b) Charge spectrum for a small-gap RPC, for different high voltage settings.

Figure 3.6: Charge spectra for a small-gap RPC and an MRPC.

The design of the MRPCs used in the TOF detector is a simmetrical stack of gaps, where a central anode is “sandwiched” by two cathodes. In Fig. 3.7 the section of an MRPC strip is sketched.

The simmetrical double-stack design has several advantages over an equivalent single stack design:

- it allows the high voltage to be considerably lower applying the same electric field ( $E \sim 100kV/cm$ );
- presents an improvement in the avalanche footprint since the pickup pads are closer to the ionization avalanche, improving the border effects between neighbouring pads[TOF02][Aki04e][Aki04d].

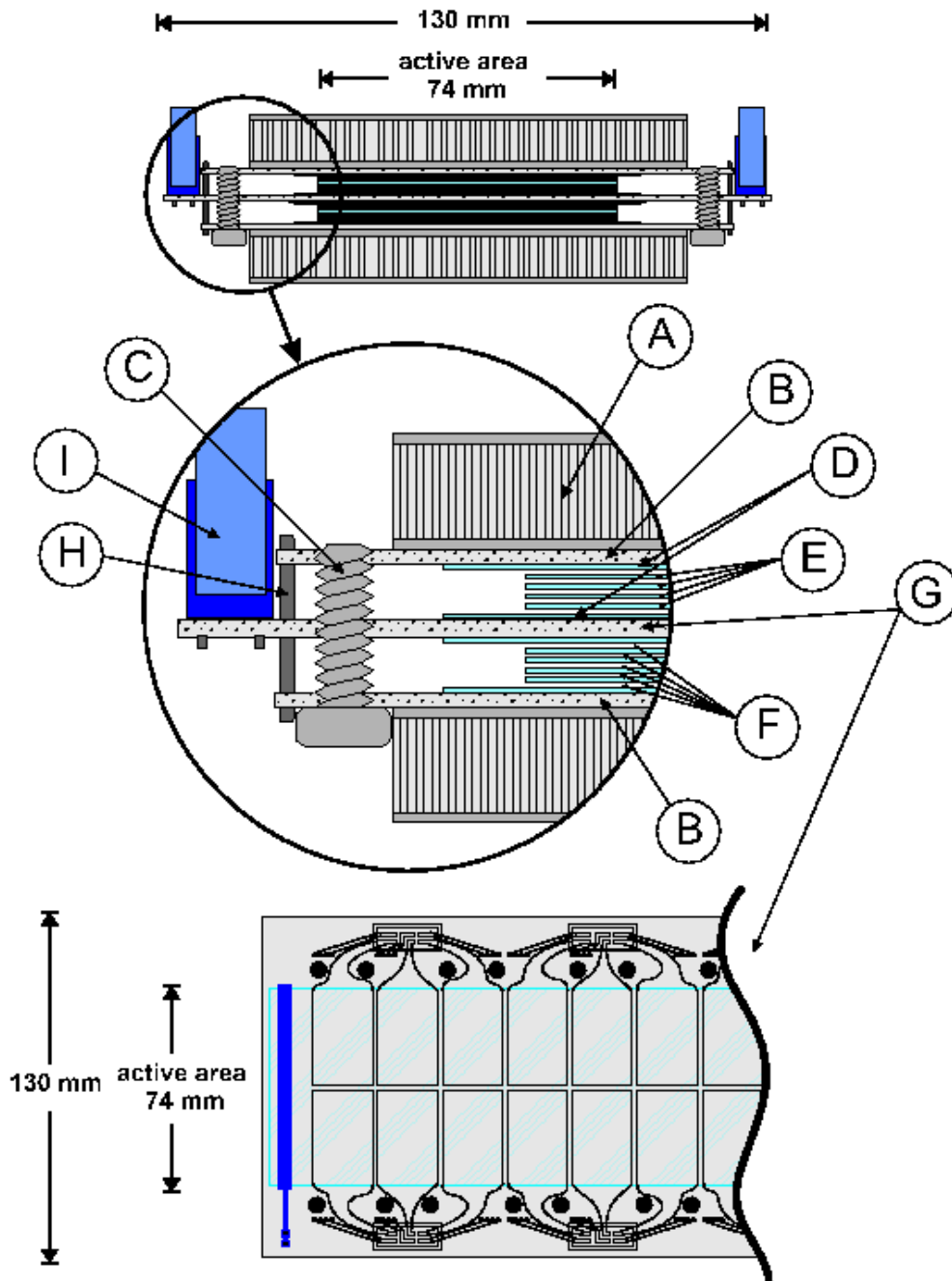


Figure 3.7: Cross section of a double stack MRPC. Elements recognizable in the picture are: **A**. 1.0 cm thick nomex honeycomb panel, **B**. cathode PCB with pads, **C**. nylon screws, **D**. external glasses treated with resistive paint, **E**. internal glasses, **F**. 250  $\mu\text{m}$  wide gaps (fishing line spacers are not shown), **G**. central PCB with anodic pads, **H**. metallic pins for connections of cathodic signals to **G** and structural support, **I**. connector for flat cables to front-end electronics.

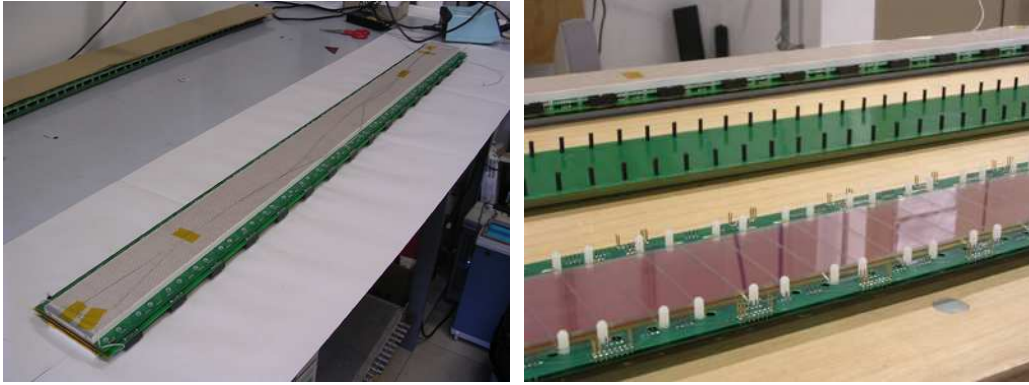


Figure 3.8: Photo of MRPCs during assembly phases. Right: an MRPC in the final assembly phase: before the last cathodic PCBs (green layers) is installed closing the MRPC structure, the spacing wire (fishing line) is recognizable between nylon screws. Left: an assembled strip.

The geometry of MRPC strips is  $122 \times 13 \text{ cm}^2$  with  $120 \times 7.4 \text{ cm}^2$  of active area,  $5 + 5$  gaps  $250 \mu\text{m}$  wide. Each strip has 96 pads of  $3.7 \times 2.5 \text{ cm}^2$  in two rows. The pads are metallic pads in a multilayer printed circuit board (PCB). The resistive electrodes are realized through painting a  $550 \mu\text{m}$  thick soda-lime glass with a resistive paint ( $\rho \sim 10^{13} \Omega \cdot \text{cm}$ ). Internal glasses are  $400 \mu\text{m}$  thick. The surface resistivity of the electrodes is depending on the thickness of the paint layer and the curing process. A quality assurance control measures the surface resistivity of the glasses to be inside the  $2 \div 25 \text{ M}\Omega/\square$  window.

The construction process of a MRPC strip is explained in [Sci04]. Fig. 3.8) shows two photos of MRPC during a assembly phase and at the end of the assembly.

MRPC strips are housed in a modular structure, consisting of 18 supermodules installed in the space frame parallel to the beam axis (shown in Fig. 3.9). Each TOF supermodule hosts 91 strips in two external and two intermediate modules (19 strips each) and one central module (15 strips). Fig. 3.10 shows the cross section of the superposition of the intermediate and central modules, in particular the picture shows the geometry of the strips tilted in order to point the interaction region with a 2 mm overlap for neighbouring strips. Fig. 3.11 shows the structure of a module: the front-end electronics (FEE), the cooling system, the PCB interface boards and, beneath it, the gas-tight module hosting the MRPC strips. In the worst case scenario of  $dN_{ch}/d\eta = 8000$ , the total number of channels fired in a central collision is  $N_{on} \sim dN_{ch}/d\eta \cdot 1.8$ , assuming 100% efficiency and geometric

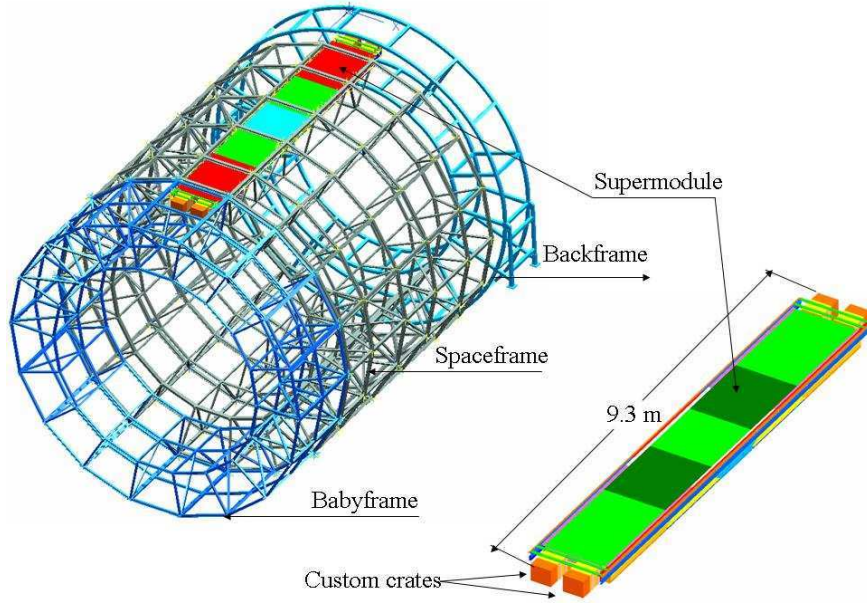


Figure 3.9: Space frame hosting one supermodule of ALICE-TOF.

acceptance (ideal case) and, with the granularity here described, the occupancy  $c$  is

$$c = N_{on}/N_{channels} \sim \frac{dN_{ch}/d\eta \cdot 1.8}{N_{sector} N_{Stripspersector} N_{channelperstrip}} \approx 9\%. \quad (3.8)$$

This rough calculation however does not consider particle decays and interactions with the detectors in front of the TOF (i.e. ITS, TPC and TRD) and the multiplicity distribution in  $\eta$ . A detailed Monte Carlo simulation shows an occupancy of 13% in the worst case scenario.

Figure 3.10: longitudinal cross section showing the overlap of two neighboring modules (i.e. central and intermediate).

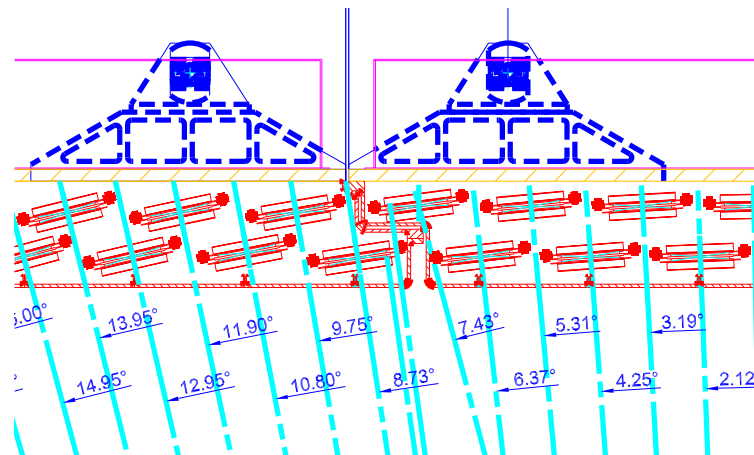
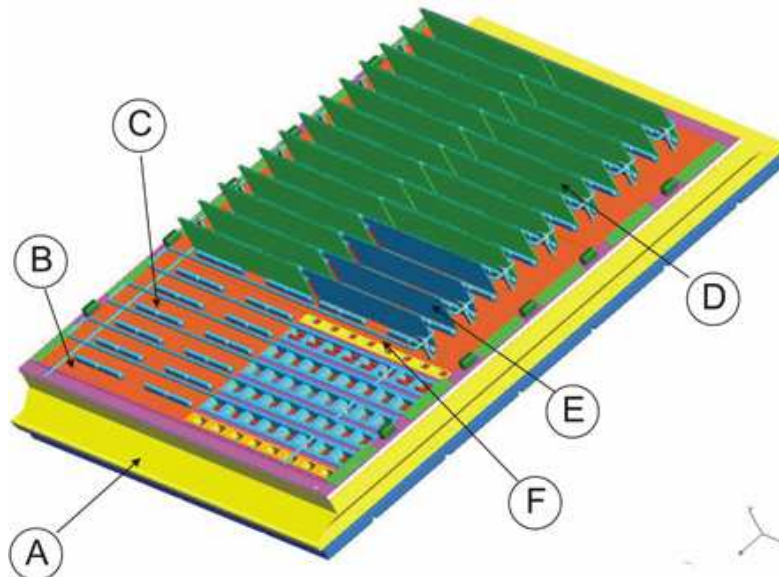


Figure 3.11: Axonometric projection of an intermediate module. **A**: Fiberglass container. **B**: Interface Board. **C**: FEE connector DIN41612. **D**: Front end electronics boards (FEA) **E,F**: Water cooling system.



### 3.2.3 MRPC Efficiency and resolution

The efficiency and the resolution of the MRPC modules have been measured with a test beam at CERN throughout both the design and production phases. The results shown in Fig. 3.12 come from the November 2006 test beam on a sample of randomly chosen MRPC strips from the mass production. Data are referred to a sample with a trigger area of  $1 \times 1 \text{ cm}^2$  and corrected for the time slewing effect<sup>2</sup>. This remarkable result is the starting point for the PID performances of the TOF detector.

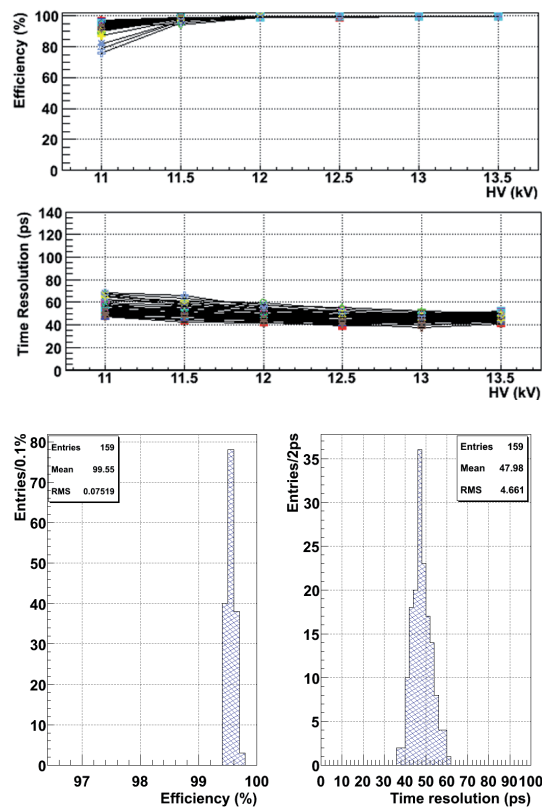


Figure 3.12: Top: Efficiency and time resolution measurements as a function of HV for 55 pads from 10 MRPCs. A long plateau with full efficiency and stable time resolution is observed. Bottom: Distribution of efficiency and time resolution measurements from 159 pads of 10 MRPCs at 13.0 KV: the pads are placed in different positions along and across each strip.

<sup>2</sup>Time slewing corrections are applied to correct the threshold-crossing effect dependent on the height of the signal[TOF02].

### 3.3 Front-end electronics

From the particle crossing an MRPC strip to data recording in the DAQ, the detection chain foresees these steps: (1) amplification, (2) discrimination, (3) digitization and (4) readout.

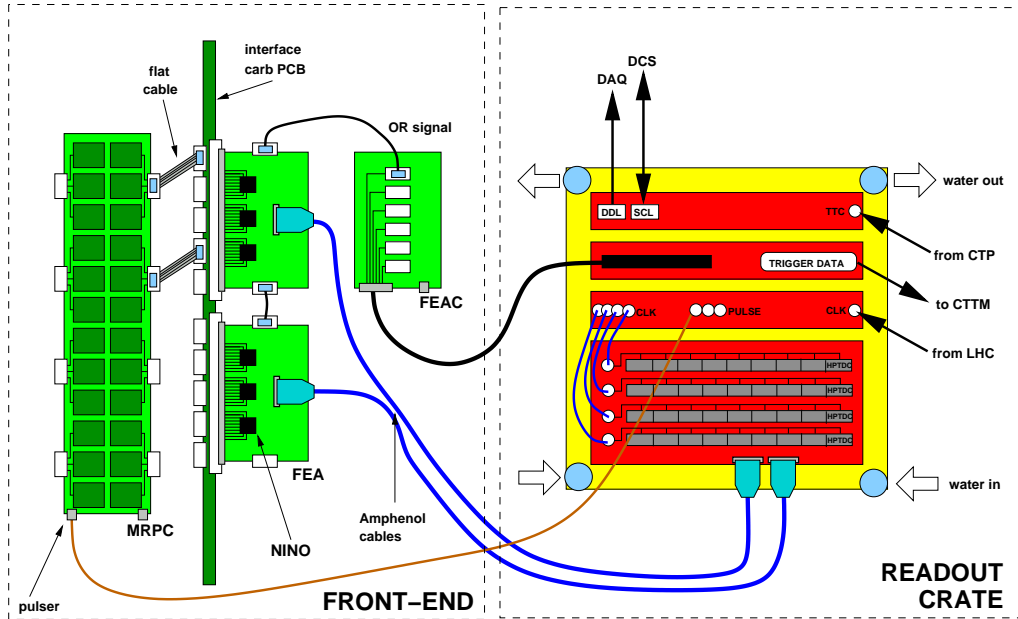


Figure 3.13: Sketch of the detector-to-readout chain in the TOF supermodules [Pre09].

In order to comply with the first two steps, the NINO[Ang04] Application Specific Integrated Circuit (ASIC) has been developed to satisfy the following requirements:

- 8 differential inputs with a capacitance matching the MRPC (i.e. 30 pF)
- LVDS output pulse whose width depends on the charge of the input signal (for time slewing corrections),
- fast amplifier (peaking time  $< 1\text{ns}$ ),
- discrimination threshold adjustable in the range  $10\div 100\text{ fC}$ .

The layout was done at CERN and submitted as part of a multi project wafer run to IBM (CMOS  $0.25\ \mu\text{m}$ ). The design is made to combine with the High Performance Time to Digital Converter (HPTDC)[Chr00] with a power consumption

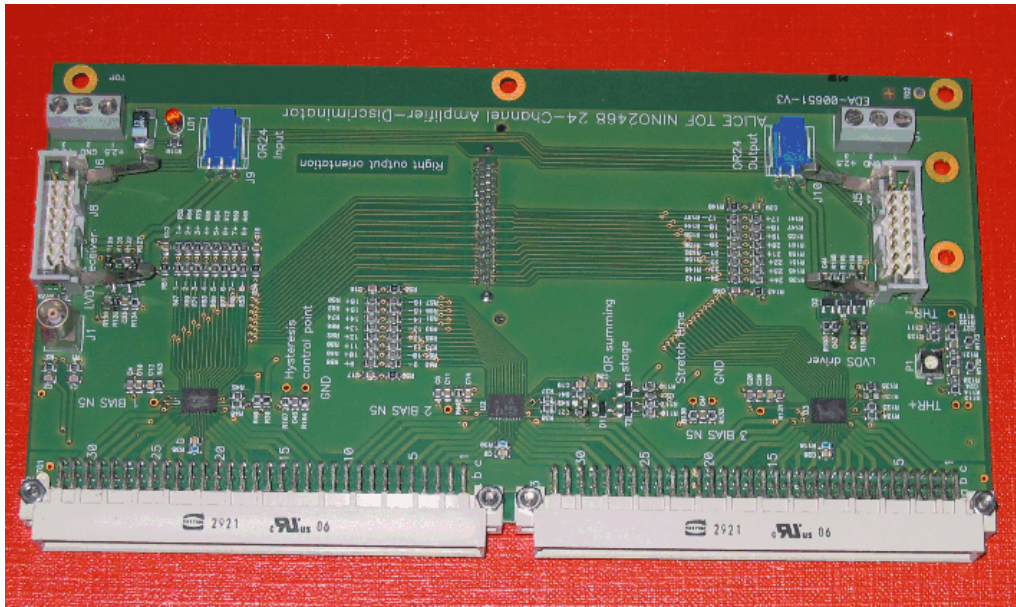


Figure 3.14: Photo of a FEA, dimensions of the board are  $(19.0 \times 10.5)$  cm<sup>2</sup>.

smaller of a factor 10 with respect to the “commercial off-the-shelf” solution initially proposed[TOF02]. The NINO ASIC, developed for ALICE-TOF is now used by other high-energy physics experiments [Len08, Tec09].

Three NINO ASICs are housed in the Front-End Analog boards (FEA) as sketched in Fig. 3.13 and shown in Fig. 3.14. Each FEA card is interfaced through an IDC flat cable (see Fig. 3.13) from a FEA Control board (FEAC) for the slow control system, power supply and trigger.

The signals on these IDC cables are listed in Tab. 3.1(a). The design of FEA offers the possibility to daisy-chain this connection.

On the FEA are also hosted:

- a threshold circuit that translates the analogic voltage of the threshold (i.e.  $0 \div 1.6$  V) to a differential threshold, since the NINO ASIC is fully differential (Tab. 3.1(b)).
- an OR summing stage; the NINO ASIC has an additional differential output providing the OR of the eight channels. A summing stage, made through discrete emitter-coupled circuitry, performs the logic OR of the three NINO OR signals and the OR of the FEA downward in the daisy-chain (a receiver is implemented).
- a VHDCI<sup>3</sup> non-magnetic connector. The 24 LVDS channels are connected to

<sup>3</sup>Very High Density Cable Interconnect. A 68 pin connector (only 48 poles are connected).

Table 3.1: Pinout of the FEA-FEAC connection 3.1(a) and Threshold levels translation table 3.1(b).

(a) Signal Assignment

pin	signal	pin	signal
1	GND	9	2.5 V
2	GND	10	2.5 V
3	GND	11	OR+OUT
4	THRESREM	12	OR-OUT
5	GND	13	+2.5_CON
6	GND	14	0V_CON
7	THRESCON+	15	2.5V
8	THRESCON-	16	2.5V

(b) Threshold levels

THRESREM	THRESCON+	THRESCON-	Differential Threshold
0	1.6	1.	0.6
1	1.6	1.4	0.2
1.6	1.6	1.6	0.

the TDC Readout Module (TRM) with an Amphenol cable.



Figure 3.15: Left: An assembled supermodule. Right: A detail of the crate pair.

## 3.4 Readout electronics

The discriminated signals are transferred from the FEE to a Custom 9U VME64 Crate where the differential signal is digitized into the time data. Each side of a supermodule hosts two crates, as shown in Fig. 3.15. The content of this crates is listed in Tab. 3.2. There are four types of VME64 modules used in the TOF Crates: the TRM (already mentioned in §3.3), the Local Trigger Module (LTM), the Clock and Pulser Distribution Module (CPDM) and the Data Readout Module (DRM).

Slot #	Crate Left	Crate Right
1	DRM	DRM
2	LTM	LTM
3	TRM	CPDM
4	TRM	TRM
5	TRM	TRM
6	TRM	TRM
7	TRM	TRM
8	TRM	TRM
9	TRM	TRM
10	TRM	TRM
11	TRM	TRM
12	TRM	TRM

Table 3.2: Crate Left and Crate Right content.

### 3.4.1 TRM

The TRM manages the TDC readout operations. The TRM deals with:

- HPTDC configuration;
- HPTDC hits reading;
- trasfering data in temporary buffers embedded in an external RAM memory bank
- data forwarding to the VME master module in a properly formatted form;
- non-linearity correction: the TRM board also features an Integral Non-Linearity look up table, that is a correction code needed in the very high resolution mode of the HPTDCs.

Each TRM hosts 30 HPTDCs and has a power consumption of  $\sim 35$  W. HPTDCs are connected in 2 chains and read parallelly by a Field Programmable Gate Array (FPGA) ACTEL APA750 (Fig. 3.16 and Fig. 3.17).

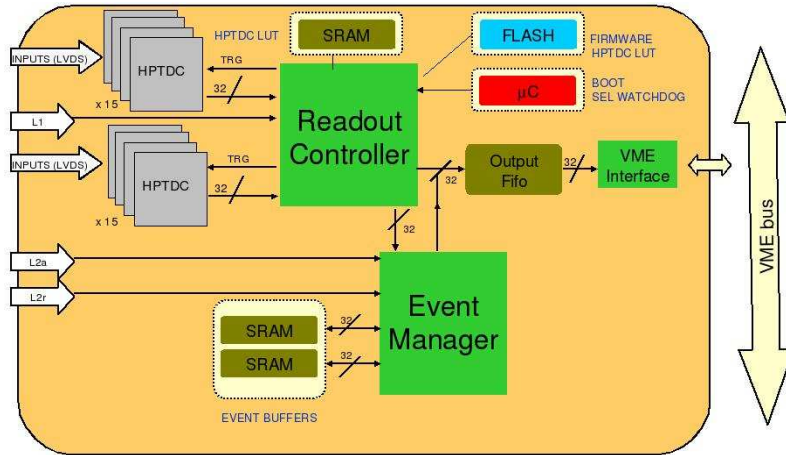


Figure 3.16: Conceptual schema of a TRM. Green boxes represents functionalities implemented inside the FPGA.

The design choice for the TRM was to build mezzanine cards (piggyback), each one hosting three HPTDCs. This choice is taken to simplify the construction of a TRM and the HPTDC replacement (HPTDC has a ball grid array package). In Fig. 3.17 a TRM is shown with an unmounted piggy-back; when mounted, the piggy-back is in contact with an aluminium bar by means of a thermally conducting silicone layer and the exposed mass layer, for heat dissipation. The ACTEL FPGA is mounted on the common PCB hosting the piggy-back cards.

## HPTDC

The HPTDC[Chr00] working principle is based on the Delay Locked Loop (DLL) pictured in Fig. 3.18. a device consisting of 3 components:

- a chain of 32 programmable delay elements; each element has one digital input, one digital output and an analog input. The programmable delay element replicates the digital input to the digital output with a delay related to the analog input voltage;
- a phase detector, that produces a voltage proportional to the delay between signals at its input (i.e. a Time to Analog Converter).
- an integrator circuit with a low-pass filter.

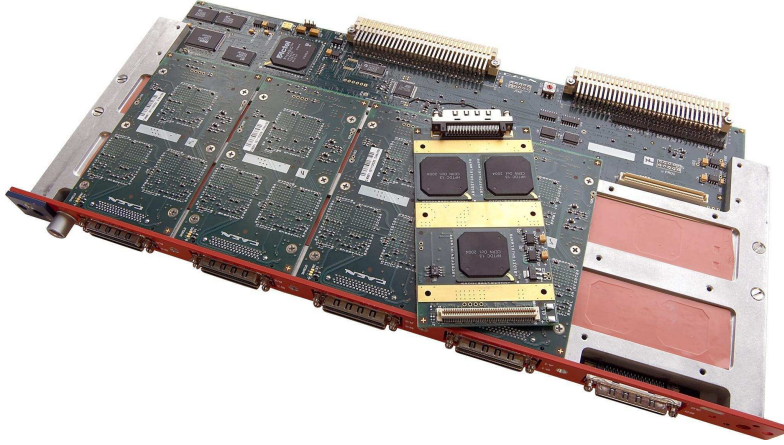


Figure 3.17: Photo of a TRM with an unmounted piggyback card. It is possible to see the aluminium bar for heat dissipation and the pink silicon layer to ensure thermal contact.

A DLL can be interpreted as a shift register, making a full circular shift in one clock cycle. The phase detector and integrating circuit are implemented to lock the shift to the input clock, using a feedback principle. The outputs of each delay element are connected in parallel to a 32-bit register. The 32-bit word is encoded in a 5 bit word representing the time of the hit in  $1/32 t_{ck}$  units.

The HPTDC is designed to meet the diverse experimental situations present at LHC and in general in high-energy physics, and has the possibility to operate in different resolution modes by multiplying the frequency of the running clock (40 MHz) by means of a Phase locked Loop (PLL). In the “high resolution” and in the “very high resolution” mode the frequency is multiplied by 8 (i.e. 320 MHz).

$$t_{min} = \frac{t_{ck}}{32 \cdot 8} = \frac{1}{f_{ck} \cdot 32 \cdot 8} = 97ps.$$

In order to further improve the time resolution, the HPTDC uses a technique similar to the one used with the mechanical vernier caliper: the hits are sent to four channels of HPTDC through an RC delay line consisting of four adjustable delay elements with characteristic time  $\tau = t_{LSB}/4$ . In this way it is possible to add two bits of interpolation with  $t_{int} = t_{LSB}/4 = 24.4ps$ , by simply counting the number of channels that mark the same “time” of the first element of the chain of delay. In this way an HPTDC can digitize 32 LVDS channels up to the “high resolution” mode or 8 channels in the “very high resolution” mode. The linearity of conversion is ensured by the HPTDC design, however when working in higher resolution modes the TDC exhibits a systematic non-linearity, probably due to clock interference

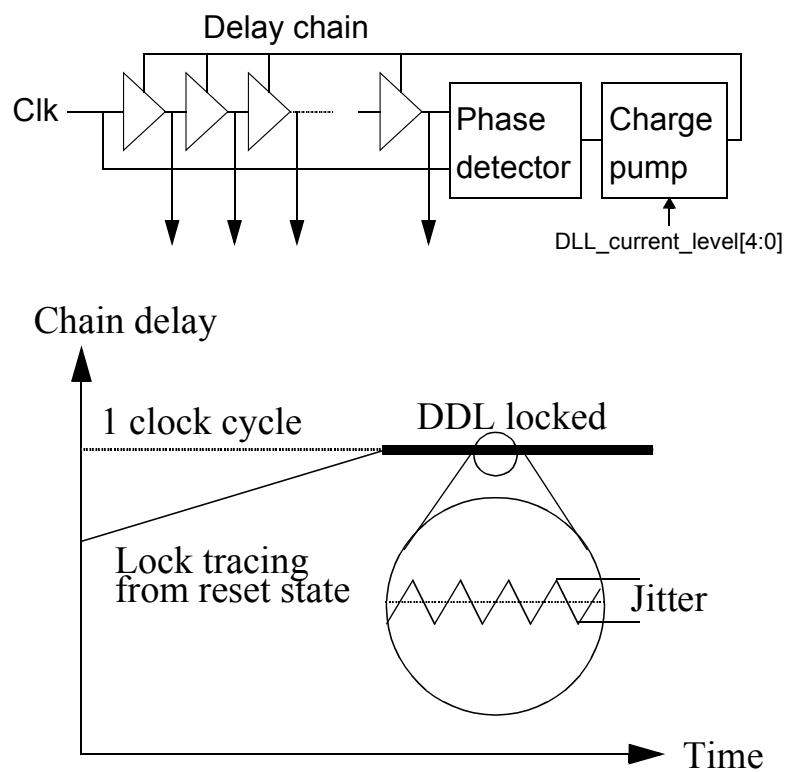


Figure 3.18: Block diagram of a DLL.

through the substrate in the 40 MHz clock domain and the 320 MHz clock domain.

In order to correct the non-linearities, a correction look-up table can be calculated through a code-density test: recording a large number of events evenly distributed in the 25 ns, the most populated bins will have a larger effective width than the less populated ones; by integrating this differences it is possible to obtain a “integral non-linearities” look-up table to correct the data directly on the readout electronics. An hit on the HPTDC is registered in an internal buffer; the hits transferred in the L1 FIFO of the HPTDC are the hits present in a valid matching window, starting  $t_{latency}$  before the trigger arrival. Both  $t_{latency}$  and the matching windows are programmable.

The NINO ASIC has the capability (Cfr. §3.3) to translate the charge in input into the width of the output pulse produced. By digitizing both the rising and the falling edge in a HPTDC, the TOF can provide time slewing corrections without requiring an ADC per channel.

### 3.4.2 CPDM

The Clock and Pulser Distribution Module is the module that receives the LHC clock via an optical fiber and sends the clock in LVDS standard to each VME module in a crate pair. The clock received by the CPDM is a dedicated clock parallel to the TTC system in order to reduce the jitter associated with it. In absence of an external clock CPDM delivers a clock locked to an internal oscillator. Further details on the synchronization of the clock and TTC signals will be given in §3.6.

CPDM also provides 17 LEMO outputs that are connected to the pulse lines of the MRPC strips. These pulse lines are capacitive coupled to the pads. A pulse on the strips allows to simulate a signal, and to control the status of the readout chain. The CPDM outputs are driven by a signal on the back plane fed by the DRM.

### 3.4.3 LTM

The Local Trigger Module is a VME64x board that monitors low voltages and temperatures in the FEE section of the supermodule and constitutes the first level of the TOF trigger

Each LTM hosts two Robinson-Nugent connectors connected to the FEACs and a 50 poles Centronics connector linked to the Cosmic and Topology Trigger Module (CTTM) see Section 3.8.

The LTM sets the thresholds for the FEA cards with a rail to rail DAC, and reads the analog value of the low voltage of the FEA, the ground level of the FEA, the value of a temperature probe on the FEAC, checks the value of the thresholds and receives the logic OR of a daisy chain. The low voltages are read by the ACTEL

APA600 FPGA through a serial Analog-to-Digital Converter (ADC) and are available on VME registers.

### 3.4.4 DRM

The Data Readout Module is a VME64x Master board that serves multiple purposes:

- In the configuration stage, Read/Write operations are issued through an optical link connected to a server devoted to the slow control (Slow Control Link, SCL).
- In run, receives and decodes trigger signals and messages from the TTC system. Part of the trigger information is stored in the data to be sent over the Detector Data Link (DDL) for consistency checks. Bunch counter reset, L1 and L2 triggers are sent to the backplane for all the VME modules.
- Reads out the data in the LTM and TRMs of the crate and formats the buffer in the common ALICE data format when a L2A trigger is issued. The buffer containing the event can be also accessed through the Slow Control Link (SCL) allowing an independent check on the data during the run without accessing the VME bus.
- Hosts a single board computer (ARM) that access the JTAG chain of all the FPGAs in the crate, allowing the re-programmation of the firmware for each of them.
- Monitors the condition of the readout and sets a busy signal to the Auxiliary Control Modules (ACMs) in case of critical DAQ conditions.
- Receives from the ACM an external pulse signal, for the detector calibration.

## 3.5 Auxiliary Control System

The development, test and installation of the Auxiliary Control System has been carried out by the Ph.D. candidate. The Auxiliary Control System is a 6U VME crate deployed in the ALICE cavern, hosting 5 ACMs that bridge L0, BUSY and PULSE signals between the trigger system and the Readout electronics. The Auxiliary Control Module (ACM) is a VME module specifically designed for the TOF project, that is able to manage the communication with up to 16 DRMs. The signals described in Tab.3.3 are transmitted in LVDS in a KERPEN megaline8 cable ( $\sim 60$  m) from one ACM to one DRM, the receiver/driver at both ends is an LVM1677. As shown in Fig. 3.19 the connector used is an RJ45.

Signal	Description	Pins	ACM side	DRM side
BUSY	DAQ/Trigger Busy	1+,2-	Input	Output
PULSE	Pulse for MRPCs	3+,6-	Output	Input
AUX	Spare	4+,5-	Input	Output
L0	L0 signal (not over TTC)	7+,8-	Output	Input

Table 3.3: Signals exchanged between ACM and DRM.

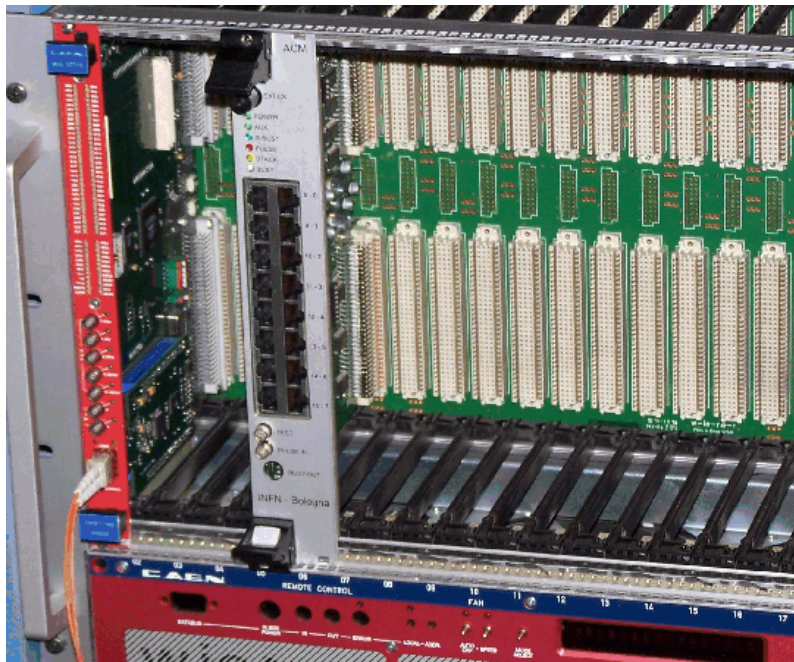


Figure 3.19: An ACM under test in Bologna.

In the Auxiliary Control System there are 5 ACMs to handle 72 crates. The ACM behaves accordingly to the slot where it is plugged, ACM in slot 6 behaves as the ACM master, ACMs in slot 8,10,12 and 14 are ACM slaves.

**Busy Handling:** The BUSY signal is a signal asserted by the DRM when a DAQ criticality is in place, the BUSY signal requests to the ALICE trigger system to stop the delivery of triggers. The auxiliary control system complies with this function elaborating the OR of the enabled inputs. The BUSY signal received from the DRM is forwarded by the ACM slaves to the ACM master through the VME backplane and processed in a logic OR by the ACM master.

Each ACM has a local busy mask stored in a dedicated VME register, to inhibit the DRMs/DDL not in readout in the OR concentration.

**Pulse Handling:** the ACM can send pulses to the enabled DRMs strobed by a signal on the backplane (Cfr. Tab. 3.4), this signal is driven by the ACM in slot 14 through VME access or external inputs. In this way it is possible to send an external pulse asynchronous with the LHC clock, to check and, if needed, to correct the integral non-linearities of the HPTDCs for all the experiment. More broadly the pulse runs are a useful tool to test the whole readout chain.

**“BUSY Occupancy” Monitor:** The ACM system monitors the BUSY state of each input with a specific counter, counting the number of bunch crossing when the busy was asserted in a 10 s second period.

This ACM feature has been proven to be a powerful debug tool for DAQ critical conditions. Identifying a faulty DRM over the 72 is greatly facilitated by this tool, since occupancy monitor counters are constantly readout and available for the shifter.

**Remote Firmware upgrade:** The functions of an ACM are implemented by means of an FPGA. The radiation doses in the UX25 zone where the auxiliary control system is deployed allows the use of a SRAM-based FPGA. The firmware is stored in an ATMEL serial flash memory and autonomously loaded at each reset of the board.

A communication interface from VME to the flash memory has been implemented in the firmware in such a way that it is possible to write the content of the flash memory through the VME connection. This remote upgrade tool ensures a great degree of flexibility for the auxiliary control system.

	A	C		A	C
1	B16	B32	17	B24	B40
2	B17	B33	18	B25	B41
3	B44	B60	19	B52	B68
4	B45	B61	20	B53	B69
5	B18	B34	21	B26	B42
6	B19	B35	22	B27	B43
7	B46	B62	23	B54	B70
8	B47	B63	24	B55	B71
9	B20	B36	25	B28	B59
10	B21	B37	26	B29	not used
11	B48	B64	27	B56	not used
12	B49	B65	28	B57	L0
13	B22	B38	29	B30	PULSE
14	B23	B39	30	B31	not used
15	B50	B66	31	B58	not used
16	B51	B67	32	nCLK	pCLK

Table 3.4: Backplane assignment for Auxiliary Control System; signals labeled with B are the masked busy inputs for the corresponding crate. The crate from ID=0 to ID=15 are not assigned in the back plane, since they are already connected at the master ACM.

## 3.6 Clock and TTC system

As already mentioned in §3.4, each board of the readout electronics system is synchronous with the LHC clock (HQCK) and receives triggers through the TTC optical system. A time alignment for TTC and HQCK is therefore needed for trigger elaboration. The procedure and measurement campaign performed by the Ph.D. candidate to align the phase of these signals is detailed in this section.

### 3.6.1 Clock and TTC distribution schema

Each left-right crate pair receives the LHC clock and TTC signals through optical fibers, the High Quality Clock (HQCK) is connected to the CPDM in the right crate, the TTC signals are connected to the two TTCrq mezzanine cards housed in the DRM.

In Fig. 3.20 a sector of the HQCK and TTC distribution system is shown; the sources for these signals are located in UX25 in the C-Area. HQCK is generated

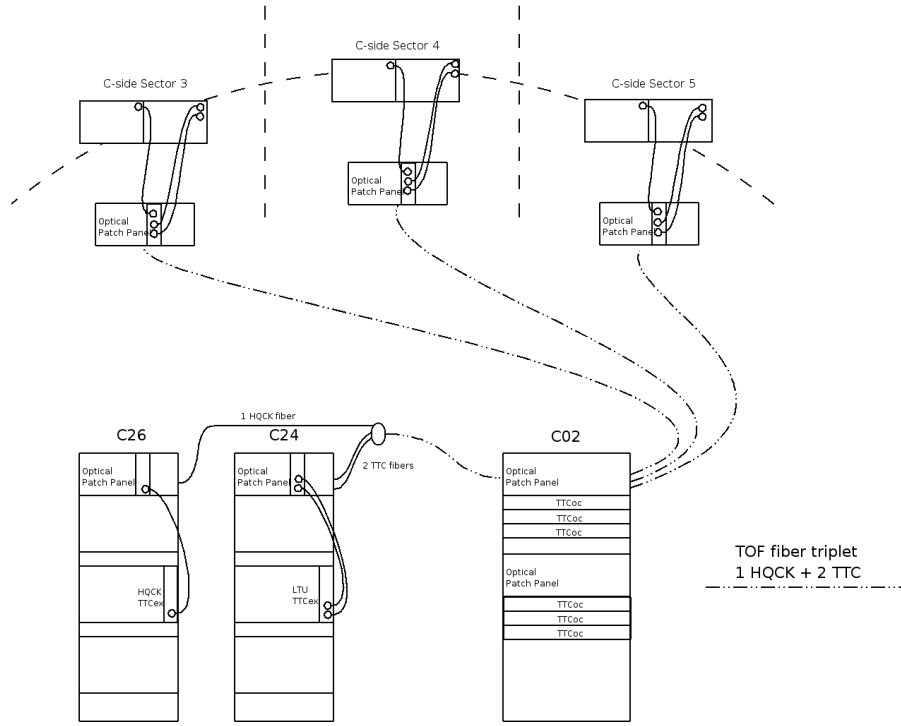


Figure 3.20: High Quality Clock (HQCK) and TTC distribution system.

from a TTC laser transmitter (TTCex) in rack C25 (2 master fibers) cabled directly with the TTC machine interface (TTCmi)<sup>4</sup> and the TTC signal is generated from the TOF LTU partition in rack C24 (4 master fibers). These fibers are routed to C02 rack and are splitted by means of 6 TTC Optical couplers (TTCocs). The TTCoc outputs feed the detector-side optical patch panels (OPP).

The difference in the length of the connections between C02 patch panel and detector-side OPP is the main cause of phase misalignment between different sectors (Fig.3.21). In order to align the phase of the signals, patch cords of different length have been deployed to absorb these delays. The procedure used to align signals on FEE consists in measuring the delays in different sectors, and deploying a patch cords with tuned length to absorb the phase differences. After deploying the calibrated patch cords, the delays of signals between different sectors will differ of an integer number of clock cycles. This difference does not affect HQCK distribution due to its periodicity, nor it affects TTC signal distribution (L1Accept, Bunch Counter Reset, Event Counter Reset), because it can be absorbed by a proper configuration of the

<sup>4</sup>The use of a dedicated TTCex reduces the jitter on the HQCK; the LHC-clock is also sent through the TTC system, however the encoding of TTC messages adds a jitter on the clock decoded by TTCrx.

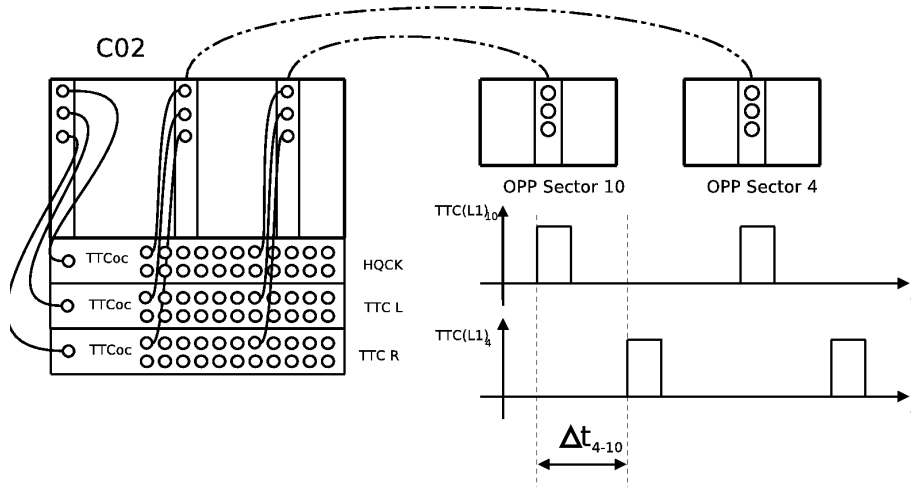


Figure 3.21: Source of misalignment for sectors 4 and 10.

TRM boards.

### 3.6.2 Measurement procedure

**Delay measurement instrumentation** An optical receiver card called HQCK and TTC Receiver Card (HTRC) is used as receiver to measure the delays on patch panels. HTRC is an electronic board designed in the electronics lab of INFN-Bologna. It hosts 2 TRR Optical receivers (for HQCK) and 2 TTCrq mezzanines (for TTC), the optical receiving circuits are the equivalent of 2 CPDMs and 2 DRMs. The signals received are then sent to LEMO connectors in LVTTTL logic. From this LEMO outputs the signals are measured with a digital oscilloscope. Fig. 3.22 shows the schematics and a picture of the HTRC.

A first calibration on delays measured with HTRC and received on FEE has been performed in laboratory. A test setup using same length of fiber and light sources similar to those in the ALICE cavern has been used to check that delays measured on FEE and using HTRC are the same. The delay between TTC decoded clock (TTCck) and HQCK is 2.2 ns in both setups. The HTRC, a digital Oscilloscope and four 15 m long fibers (two for HQCK and two for TTC) have been used to measure delays on detector side patch panels. Sector 4 is taken as a reference for C side measurements because it has the longest path from OPP on rack C02 to detector-side OPP. The signals measured are HQCK, TTCck and Level 1 trigger Accept (L1A). In Tab. 3.5 the data taken on C-side patch panels are presented.

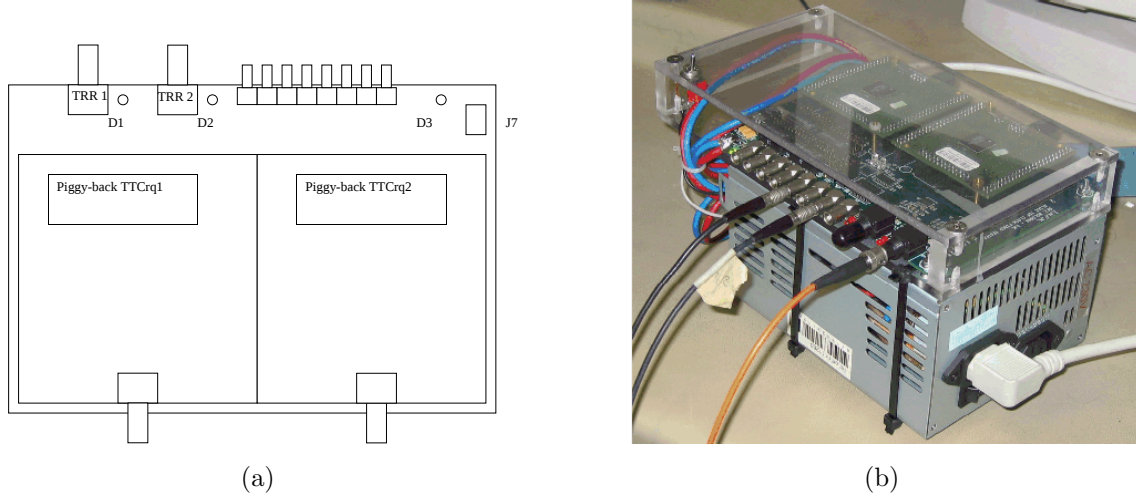


Figure 3.22: Layout and photo of the HQCK and TTC receiver card (HTRC).

Table 3.5: Delay data on C-side patch panels in ns. The time resolution of the oscilloscope used in the measure is 0.2 ns.  $t_{Hi}$  is time of the clock rising edge for HQCK on the sector  $i$ ,  $t_{TRi}$  and  $t_{TLi}$  are the same measurements for TTC clock for the right DRM and left DRM,  $L1a_{Ri}$  is the time of the rising edge of the Level 1 trigger accept signal for the right DRM in sector  $i$ .

Sector	$t_{H4} - t_{Hi}$	$t_{H4} - t_{TRi}$	$t_{H4} - t_{TLi}$	$t_{TRA} - t_{TRi}$	$t_{TRA} - t_{TLi}$	$L1a_{RA} - L1a_{Ri}$	$L1a_{RA} - L1a_{Li}$
0	00.0	02.8	02.8	00.0	00.0	25.4	25.4
1	19.4	21.8	21.8	19.0	19.0	19.0	19.0
2	12.8	16.0	16.0	12.5	13.0	13.0	13.6
3	06.4	08.8	08.8	06.3	06.3	06.3	06.3
4	00.0	03.2	03.2	00.0	00.0	00.0	00.0
5	09.1	11.6	11.6	08.8	08.0	08.8	08.0
6	17.1	19.0	19.0	15.8	15.8	15.8	15.8
7	21.0	24.0	24.0	20.9	20.9	20.9	20.9
8	22.3	00.0	00.0	22.5	22.5	22.5	22.4
9	23.1	02.2	01.9	24.0	23.8	24.0	23.8
10	10.2	12.5	12.5	09.3	09.3	34.7	34.7
11	24.1	01.2	01.0	22.8	22.8	48.2	48.2
12	03.4	05.5	05.5	02.2	02.2	53.2	53.2
13	03.4	06.5	06.5	03.3	03.3	54.0	54.0
14	01.9	05.2	04.5	01.9	01.9	52.2	52.2
15	17.6	19.9	19.9	17.2	17.2	42.8	42.8

### 3.6.3 Calibration of the patch cords length

The synchronization of signals on FEE of different sectors is granted if every sector is connected using a patch cord length according to this equation:

$$\frac{n}{c}L_i + t_{HQCK_i} = \frac{n}{c}L_4 + t_{HQCK_4} \quad (3.9)$$

where  $L_i$  is the length of patch cord on the sector  $i$ ,  $L_4$  is the length of patch cord in sector 4 (the shortest in C-Side),  $c$  is the speed of light and  $n$  is refraction index for the fibers used ( $n = 1,469$ ), while  $t_{HQCK_i}$  is the time of a high quality clock transition on the patch panel. The length of the patch cord computed with the previous equation is then

$$L_i = L_4 + \frac{c}{n}(t_{HQCK_4} - t_{HQCK_i}) \quad (3.10)$$

Tab. 3.6 lists the length of fibers computed according to the eq. 3.10; the length have a 5 cm clearance, according to the time resolutions of the system ( $200 \text{ ps} \times c/n = 4 \text{ cm}$ ). The length of the detector-side patch cords has been computed using only HQCK information, common delays between HQCK and TTC will be absorbed by changing the length of the TTCoc input fibers in C02; this choice allows to take the patch cords for TTC and HQCK in a sector of the same length, thus facilitating the spare fibers management.

Table 3.6: Length of sector (C-side) patch cords according to the time alignment procedure.

Sector	0	1	2	3	4	5	6	7	8	9	10	11	12	13	14	15	16	17
Length (m)	1.30	5.25	3.90	2.60	1.30	3.15	4.80	5.	5.85	6.00	3.40	6.20	2.00	2.00	1.70	4.90	4.05	2.45

The procedure has been performed to synchronize the signals on the A-side patch panels; delays and computed lengths are listed in Tab. 3.7 and Tab. 3.8. The choice of sector 8 as a reference was taken in order to facilitate the measurement, because the fibers from A-side OPP and C02 are roughly equal.

### 3.6.4 Reference crates measurement

In the procedure shown in this section, the time references used for the measurements reported in Tables 3.5 and 3.7 have been sector 4 C-side and sector 8 A-side respectively. To provide a common time frame for the TOF, the delay between the reference sectors was measured. In addition, the delay from one TOF optical patch panels and the T0 optical patch panels was measured.

Table 3.7: Delay data on A-side patch panels (ns). The time resolution of the oscilloscope used in the measurements is 0.2 ns.

Sector	$t_{HS} - t_{Hi}$	$t_{HS} - t_{TRi}$	$t_{HS} - t_{TLi}$	$t_{TRS} - t_{TRi}$	$t_{TRS} - t_{TLi}$	$L1a_8 - L1a_{Ri}$	$L1a_8 - L1a_{Li}$
0	-0.3	10.8	10.5	-3.8	-4.2	-4.4	-4.5
1	-0.3	12.8	13	-1.5	-1.5	-1.9	-1.7
2	-3.6	9.9	9.3	-4.5	-4.9	-5.1	-5.2
3	-3.5	9.6	9.1	-4.6	-4.9	-5.2	-5.3
4	-2.6	-13.8	-13.7	-3.5	-3.4	-3.9	-3.5
5	2.9	-8.7	-8.6	1.6	1.8	0.9	1.2
6	1.7	-9.5	-9.6	0.5	0.5	0.1	0.3
7	3.9	-7.4	-7.4	2.6	2.8	2.7	2.8
8	0	-9.9	-10.4	0	-0.5	0	-1.1
9	5	-6.4	-6.3	3.8	3.8	2.4	3.4
10	5.8	-5.4	-6.2	4.7	4	4.4	3.2
11	1.3	-8.9	-8.9	1.5	1.5	0.6	0.6
12	1.8	-9.3	-9.3	1.1	1.9	0.5	0.2
13	2	-8.9	-9.8	1.4	0.3	0.8	0
14	5.3	-5.9	-5.5	4.3	4.6	3	3.4
15	5.5	-5.6	-5.8	4.6	4.4	4.5	4.1
16	5.9	19.6	19.4	4.8	4.7	4	4.3
17	7.6	-3.7	-3.8	6.5	6.5	4.9	5.9

Table 3.8: Length of sector (A-side) patch cords according to the time alignment procedure.

Sector	0	1	2	3	4	5	6	7	8	9	10	11	12	13	14	15	16	17
Length (m)	3.8	3.8	4.5	4.5	4.2	3.1	3.3	2.8	3.5	2.7	2.5	3.3	3.3	3.3	2.5	2.5	2.5	2.1

The T0 detector uses, as readout electronics, a TOF custom crate hosting one DRM, one CPDM and one TRM. This measurement was done to provide a common time reference for the event time. In this particular measurement, the connections of the HTRC to the T0 and TOF OPP (sector 13 A-side, since the measurement was done with the L3 magnet doors closed) are done with a 30 m and a 15 m long fibers respectively.

Tab. 3.9 lists the delays in ns for the reference crates and T0 crate measurements; the delays measured between the reference crates are used to compute the length of the common A-side and C-side patch fibers in rack C02. By tuning the delay at the inputs of the TTCoc optical splitters, it is possible to introduce a common delay for the 18 OPP of one side. The length computed according to this procedure are listed in Tab. 3.10.

Table 3.9: Delays in ns on sector 4 C-side and T0 patch panel. Sector 4C delays are referred to sector 8A, while T0 delays are referred to sector 13A. The label T0+15m is to take into account the length of fiber used in this peculiar measurement.

Sector	$t_{H8A} - t_{Hi}$	$t_{H8A} - t_{TRi}$	$t_{H8A} - t_{TLi}$	$t_{TR8A} - t_{TRi}$	$t_{TR8A} - t_{TLi}$	$L1a_{8A} - L1a_{Ri}$	$L1a_{8A} - L1a_{Li}$
4C	7.3	7.4	-2.8	-2.7	47.3	47.5	-7.7
Sector	$t_{H13A} - t_{Hi}$	$t_{H13A} - t_{TRi}$	$t_{H13A} - t_{TLi}$	$t_{TR13A} - t_{TRi}$	$t_{TR13A} - t_{TLi}$	$L1a_{13A} - L1a_{Ri}$	$L1a_{13A} - L1a_{Li}$
T0 +15m	-	-	-	3.7	-	128.7	-

Table 3.10: T0 crate and TTCoc input fiber lengths.

Position	Length (m)
C02 A TTC	1
C02 A HQCK	2.6
C02 C TTC	3.6
C02 C HQCK	2.4
T0 HQCK	3.1

### 3.7 Uncertainty sources in TOF measurement

The goal for the TOF detector is to reach an overall time resolution better than 80 ps. Each component of the system introduced in the previous sections contributes to the global error on TOF with its uncertainties. Excluding the intrinsic MRPC resolution ( $\sigma_{MRPC} \lesssim 40$  ps), the contributions to the overall resolution can be traced down in the following list:

- $\sigma_{FEE}$  time jitter from FEE amplification and discrimination;
- $\sigma_{TDC}$  HPTDC time resolution;
- $\sigma_{CAL}$  errors on calibration constants. Each readout channel has its own characteristic constants due to the different paths in the detector and pad-dependance of the time slewing coefficients. The error on the calibration constants depends on the statistics accumulated on the single channel.  $\sigma_{CAL} = \sigma / \sqrt{N_{events}}$ .
- $\sigma_{ClkTDC}$  jitter of the clock signal on the HPTDC; it is the sum of the clock jitter from the source and the jitter on the clock distribution system

$$\sigma_{ClkTDC}^2 = \overbrace{\sigma_{Clk}^2}^{intrinsic} + \overbrace{\sigma_{ClkDis}^2}^{distribution} ;$$

- $\sigma_{T0}$  error on the event time ( $T_0$ ). The indetermination on the event time depends on the technique used for its evaluation;
- $\sigma_{reco}$  error on the reconstruction of the event; it is the sum of the track length error and the momentum resolution.

$$\sigma_{reco}^2 = \sigma_{track\ length}^2 + \sigma_p^2.$$

depends on the technique used for its evaluation.

The global resolution on TOF is the sum in quadrature of the errors on the single independent elements, i.e.

$$\begin{aligned} \sigma_{TOF}^2 &= \sigma_{CAL}^2 + \sigma_{ClkTDC}^2 + \\ &+ \sigma_{TDC}^2 + \sigma_{FEE}^2 + \sigma_{MRPC}^2 + \sigma_{reco}^2 \end{aligned} \quad (3.11)$$

with  $\sigma_{CAL} = 30$  ps [Zam06],  $\sigma_{ClkTDC} = 18$  ps [PPR06]  $\sigma_{reco} \approx 30$  ps [PPR06], the sum of the contributions of  $\sigma_{ClkDis}$ ,  $\sigma_{TDC}$ ,  $\sigma_{FEE}$  and  $\sigma_{MRPC}$  is approximately 48 ps (Cfr. Fig. 3.12, [Aki09]). The resolution  $\sigma$  used in Eq. 3.6 is if  $t_0$  is

$$\sigma^2 = \sigma_{TOF}^2 + \sigma_{T0}^2. \quad (3.12)$$

When the event time is obtained from the T0 detector (Cfr. §2.4.7), the  $t_0$  resolution is

$$\sigma_{T0}^2 = \sigma_{T0\ detector}^2 + \sigma_{clkTDC}^2 + \sigma_{TDC}^2 \quad (3.13)$$

with  $\sigma_{T0} \approx 50$  ps. The resulting total time resolution is  $\sigma$  is 80 ps.

For events with a particle multiplicity high enough (e.g. Pb–Pb central events), it is possible to determine  $t_0$  from the hits on TOF through the best combination  $C^{best}(m_1, \dots, m_N)$  of the  $3^N$  mass hypothesis  $(\pi, K, p)$ , by minimizing

$$\chi^2(C) = \sum_{i=1, \dots, N} \frac{[t_i^0(m_i) - \langle t^0(C) \rangle]^2}{\sigma_i^2} \quad (3.14)$$

where  $t_i^0(m_i) = t_i^{exp}(m_i) - t_i^{TOF}$  is the difference between the expected arrival time for a particle of mass  $m_i$  and the time measured by the TOF detector. This algorithm is able to provide an unbiased  $t_0$ ; a Monte Carlo simulation shows that the resolution on  $\sigma_{T0}$  can be as low as 5 ps [PPR06]. Using the determination of the event time from TOF the  $\sigma$  is about 65 ps.

## 3.8 Trigger system

The goal of the TOF trigger system is to exploit the fast, low noise signals generated on the MRPC strips to provide a topological trigger to the experiment. The large granularity of the TOF and the relatively low noise ( $\sim 0.6\text{Hz}/pad$ ) of the MRPC allow triggering on several configurations:

- Resonance produced in Ultra Peripheral Collisions (UPC);
- Events with very large/low track multiplicity, corresponding to central/peripheral ion-ion collisions;
- Cosmic Rays.

### 3.8.1 Trigger electronics

The design of the trigger system is a two-layer architecture (LTM, CTTM), from the detector to the Central Trigger Processor (CTP) inputs:

- **MRPC**  $\rightarrow$  **LTM**: the signal induced on the pad at the passage of the charged particle is transported by means of flat cables at the input of the NINO ASICs on the FEA (cfr. §3.3), the signal then contributes to form the OR output on the NINO ASIC. The outputs of the NINO ASICs in the FEA are summed up in a

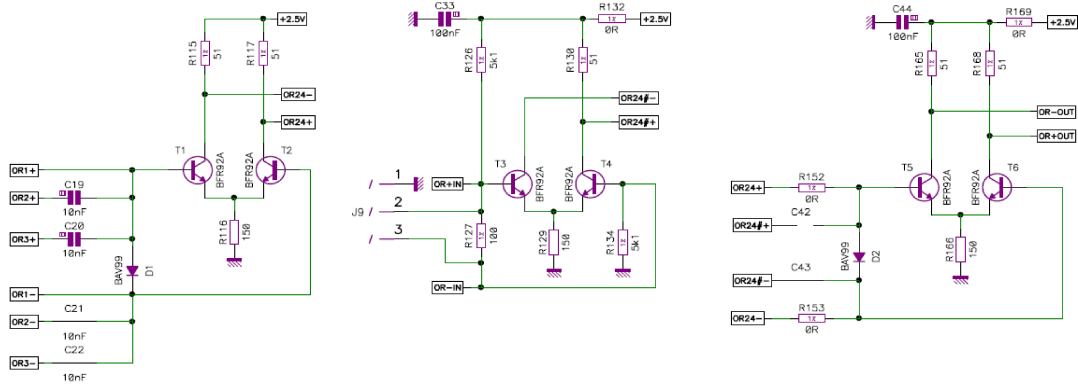


Figure 3.23: Circuit design of the OR summing stage. Left: OR sum of the 3 NINO ASICs. Center: receiver stage for the downward FEA in the chain. Right: final OR summing stage.

differential summing circuit shown in Fig. 3.23. The OR signal, corresponding to half-strip (i.e. 48 MRPC pads - 444 cm<sup>2</sup>), is then sent through the FEAC to the LTM (Cfr. §3.4.3).

- **LTM** → **CTTM**: in the LTM the 48 signals from the detector are sent to an LVDS receiver (SN65LVDS348) and through a Programmable Delay Line (PDL) whose purpose is to absorb the time differences from the cable length. The time-aligned signals are then shaped to a 25 ns pulse using a 160 MHz clock from an internal PLL; the channels can be masked using a proper register, this is particularly useful when a channel is connected to a LV/HV channel that is off. Masking the line prevents noise to contribute to the trigger elaboration. The channels are then concentrated in 24 channels in a 2-fold OR and sent to the CTTM through an Amphenol cable (Skewclear 166-2499-971), connected to a Centronics 50-pole connector. The use of such connectors in a 0.5 T magnetic field required a custom non magnetic shell, machined by the INFN Bologna mechanical workshop. Such cable has 25 shielded pairs, 100 Ω pair impedance, attenuation ~0.15 dB/m (at 40 MHz). Fig.3.24 shows an open-eye pattern of this custom cable. The signals to CTTM are center aligned with a 40 MHz clock signal that is sent to CTTM as well.

The LTM is equipped also with a VHDCI connector, that is connected by means of a splitter board to a TRM and to 2 RJ45 cables. This connection provides a way to store through DAQ the LTM outputs during a run and to send through the 2 RJ45 cables a Pre-Trigger to the Transition Radiation Detector. Tab. 3.11 lists the connections of the LTM to the other elements of

the trigger chain.

Table 3.11: LTM interconnections list.

Origin	Destination	Signals	Description
LTM	CTTM	25	Data to CTTM
LTM	TRM	24	Data debug
LTM	ALIC-TRD	up to 8	Pre-trigger
FEAC	LTM	48	OR signals
FEAC	LTM	8	Temperature
FEAC	LTM	16	Low Voltage
LTM	FEAC	16	Threshold

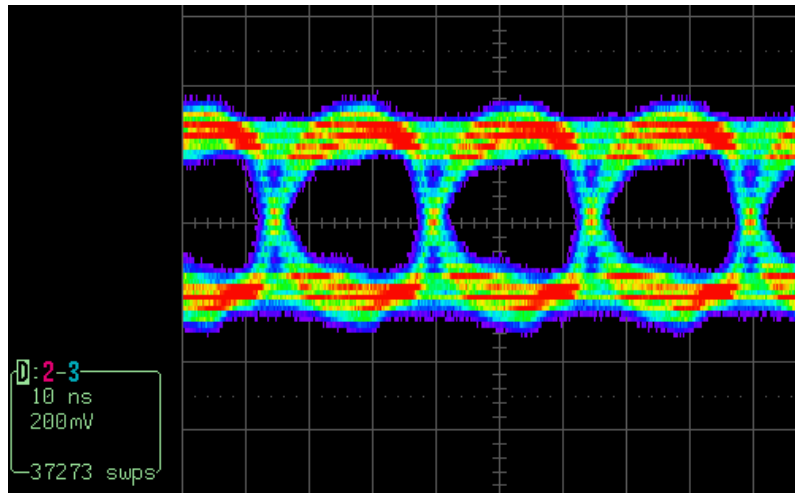
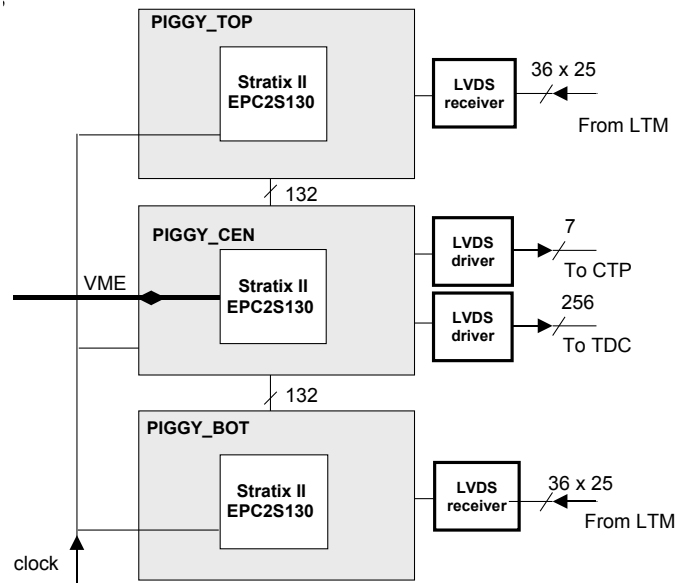
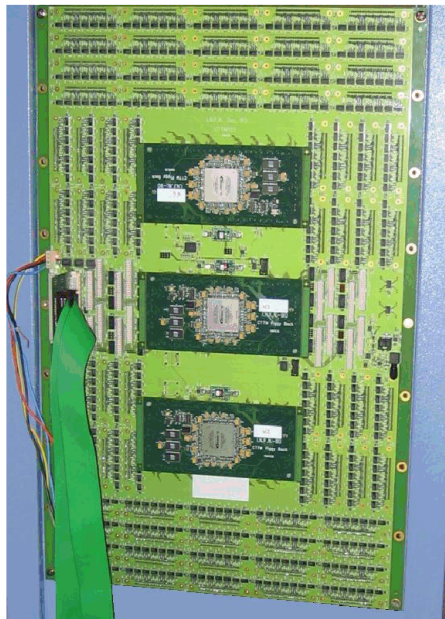


Figure 3.24: Oscilloscope screenshot of the open-eye pattern at 40 MHz for the Skewclear 166-2499-971.

- **CTTM**  $\rightarrow$  **CTP**: The Cosmic and Topology Trigger Module (CTTM) is the board that serves as a concentrator for the  $24 \times 72$  channels, from the LTMs. The development, test, installation and commissioning of the CTTM have been carried out by the Ph.D. candidate, throughout the 2007–2009 period.



(a) Conceptual schematics of the CTTM



(b) Picture of the front side of the CTTM during the tests in Bologna



(c) Picture of the back side of the CTTM during installation at CERN

Figure 3.25: conceptual schematics and pictures of the CTTM.

**CTTM Design** The maximum number of user available I/O pins on a commercial FPGA is  $\sim 1200$ , therefore it is impossible to manage the LTM signals with only one FPGA.

The choice was to build the CTTM as a very large board ( $78\text{ cm} \times 41\text{ cm}$ ) equipped with cable connections and LVDS receivers/drivers and hosting 3 mezzanine boards (piggyback). In Fig. 3.25(b) and Fig. 3.25(c) are shown the front and the back side respectively; on the back side are located the connectors for the 72 LTM cables and the cables to CTP; On the front side are located the LVDS receivers SN65LVDS348 (chosen for the wide common mode input voltage range<sup>5</sup> providing a safety margin in the data transmission on the 60 m long cables deployed), the VME connection for slow control and the fiber clock receiver. The CTTM is synchronous to the LHC clock by means of an optical fiber, in operating condition the clock generating the inputs on LTM is locked with this clock. There are also two 40 MHz oscillators housed on the board; the VME finite state machine (FSM) is driven by one of these in order to ensure SLC communication with the board even in case of a major clock failure<sup>6</sup>. Each piggy back, Fig. 3.25(a), is equipped with a high-end FPGA (Altera Stratix II EPC2S130) and is connected to the mother board using high density Samtec connectors. The motherboard is fed with 3.3 V and 5 V power supply from the VME crate: the total power consumption is 35 W. The FPGAs employed in this board have a 130 nm CMOS technology core that uses 1.2 V supply voltage; since the 1.2 V supply is not provided by the VME crate, the CTTM houses a miniature DC/DC switching modules (PTH03060) for each piggyback (three in total). The LV supply channels for the piggyback cards (three 1.2 V channels and three 3.3 V channels) are continuously monitored using external VME boards.

The slave piggyback boards (hereafter PIGGY\_TOP and PIGGY\_BOT) receive each 864 data bits and take a pretrigger decision. The master piggyback board (hereafter PIGGY\_CEN), connected to PIGGY\_TOP and PIGGY\_BOT by two 132 bit bus, elaborates these informations and asserts the L0/L1 decision. The output signals are sent to the CTP through 7 cables, using the LVDS standard.

---

<sup>5</sup> A differential receiver responds to the voltage difference at the inputs, provided that the common mode input voltage is in the allowed range. The common mode voltage is the average voltage of the inputs and may play an important role when receiving data from long cables such as the one used in this case.

<sup>6</sup>A failure on the central clock for TOF detector is a condition that blocks all the readout electronics. The DRM has a similar backup system.

**Slow Control** PIGGY\_CEN acts as a VME slave (A32/D16) and the connection with the VMEbus is made using two flat cables. The firmware for VME communication has been implemented in the PIGGY\_CEN FPGA. Slow control settings on PIGGY\_TOP and PIGGY\_BOTTOM are implemented through a serial link occupying 5 lines of the inter-FPGA bus. The choice of a serial standard is due to two main reasons: the cross talk is reduced and more lines can be used for the elaboration of the trigger. A dedicated slow control server monitors continuously the parameters of the CTTM.

**Remote upgrade** The CTTM is deployed in the UX25 experimental cavern in rack C03. Recalling what anticipated in §3.5, the radiation environment allows the use of SRAM-based FPGAs. Access to the experimental zone is forbidden during the beam for safety reasons, and the upgrade of the firmware must be implemented remotely. Each piggyback hosts an Altera EPCS64 flash memory containing the firmware image, that is loaded at every board reset. This image can be written remotely by means of an embedded Mega Function<sup>7</sup> (Serial Flash Loader, SFL)[AN370]. The firmware of PIGGY\_TOP and PIGGY\_BOTTOM is written through the serial communication link aforementioned while the firmware of PIGGY\_CEN is written through VME accesses.

**CRC error monitoring and Latch-up protection** Despite the relatively low fluence on the racks allows the use of SRAM-based FPGA, the 130 nm cores of the FPGAs are protected with two precautionary measures:

- Cyclic Redundancy Check (CRC) is monitored for the 3 FPGAs by PIGGY\_CEN and available to the user. If a CRC error happens in PIGGY\_CEN, the firmware issues a self-reset.
- Latch-up protection is implemented on each FPGA core separately by means of 3 PMOS switch with Thermal Shutdown (Maxim MAX893) that break the core supply if the 1.2A limit is reached.

**Debug LVDS outputs** In order to provide an external timing measurement for the input signals, the system foresees the installation of 4 commercial TDC modules connected to PIGGY\_CEN by 256 LVDS lines. Using this system,

---

<sup>7</sup> A Mega Function is the name used by the Altera Quartus Software to identify a proprietary VHDL function available for the user.

PIGGY\_TOP and PIGGY\_BOTTOM can multiplex in PIGGY\_CEN the signals of 10 LTM-CTTM cables.

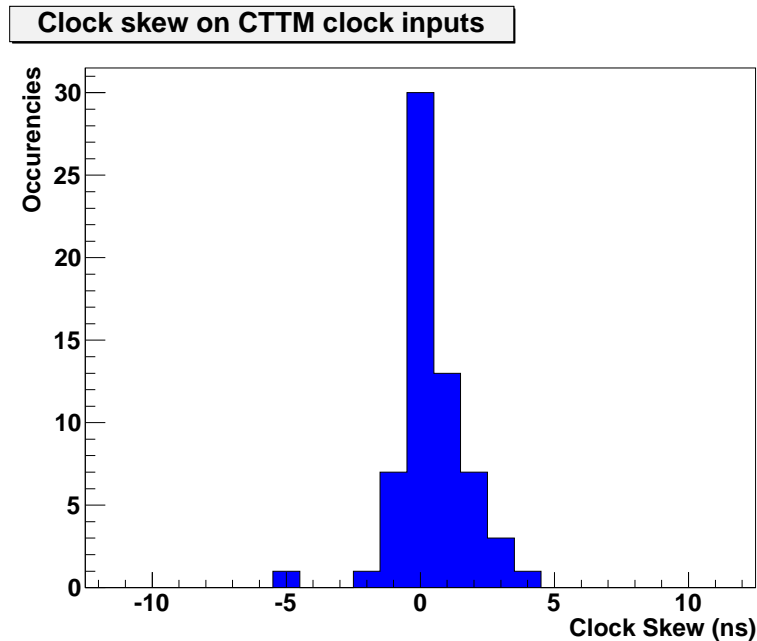


Figure 3.26: Clock skew distribution on the CTTM clock inputs.

**Clock alignment** The signals from the LTMs are center-aligned with the clock of the LTM-CTTM cable. The cables are 60 m long and have been measured to be of the same length within 1 ns. However the LVDS drivers and receivers have propagation delay differences between samples. Tab. 3.12 presents the values of the propagation delay quoted in the datasheets of the used components.

Fig. 3.26 shows the clock skew distribution on the 72 CTTM inputs. The skew is measured with a digital oscilloscope taking one of the clock signals as a reference, the skew distribution is therefore centered around this value. The narrow peaked skew distribution reduces the probability of timing violations in the behaviour of the firmware, and is a fundamental parameter for the timing analysis through the ALTERA analysis tool.

In Tab. 3.13 are presented the latencies of the different components of the trigger system to show that the signal elaborated fits comfortably in the L0 latency

constraint ( $\lesssim 800$  ns, Cfr. §2.5.1).

Table 3.12: Propagation delay in the CTTM LVDS receiver (SN65LVDS348) and LTM driver (SN65LVDM1677). [Tec03] [Tec01]

SN65LVDS348 PARAMETER	MIN	TYP	MAX	unit
tPLH Propagation delay time, low-to-high-level	2.5	4	6	ns
tPHL Propagation delay time, high-to-low-level	2.5	4	6	ns
SN65LVDM1677 PARAMETER	MIN	TYP	MAX	unit
tPLH Propagation delay time, low-to-high-level	1.3	2.5	3.6	ns
tPHL Propagation delay time, high-to-low-level	1.3	2.5	3.6	ns

Table 3.13: Trigger latencies for the L0 trigger decision.

Source	TOF	MRPC $\rightarrow$ FEA	FEA $\rightarrow$ LTM	LTM(PDL)	LTM $\rightarrow$ CTTM	CTTM	Total
Delay (ns)	20	10	30	160	260	250	730

# Chapter 4

## Physics Trigger capabilities of the TOF detector

As mentioned in §3.8, the TOF trigger system exploits the fast rise time and the relatively low noise of the MRPC strips to identify several event configurations:

- Cosmic rays physics;
- pp minimum-bias;
- Events with very large/low track multiplicity;
- Resonances produced in Ultra Peripheral Collisions (UPC).

In this chapter will be presented the results obtained by the TOF trigger in the ALICE experiment during the commissioning and 2009 cosmic-ray run (before the *pp* beam) and the foreseen configurations in Pb-Pb and *pp* collisions.

### 4.1 TOF trigger for cosmic rays

After the 2008 magnet incident, the LHC underwent a long repair period. During this forced long stop ALICE profited of this period in two ways: in the first months, a long hardware-upgrade phase took place, then a long run of cosmic-ray data-taking was carried out from week 34 (17.08.2009) to week 44 (30.10.2009).

The main goal of the 2009 cosmic run was to collect enough data in different detector configurations for TPC calibration and tracking detectors alignment, ensuring running stability and commissioning the DAQ up to the rates expected for the beam. In order to cope with this goals the Collaboration required a L0 trigger capable to select several tenths of muons per second.

ACORDE is a detector devoted to provide a cosmic ray trigger, but its geometrical configuration does not allow a purity<sup>1</sup> higher than 2%.

Assuming a rate of 150 Hz, the true muon rate is 3 Hz, which is far below the requests of the Collaboration.

The TOF trigger is a perfect candidate for selecting cosmic rays in the barrel, due to its large area and the barrel geometry. In this section, some of the results achieved with the TOF as a cosmic trigger detector will be presented.

### 4.1.1 Noise estimation

During test beams and in the early installation phases, the noise rate on the pad has been measured to be  $0.54 \text{ Hz/cm}^2$  [PPR06], the noise rate is therefore low for an RPC system, however when considering the large area of the TOF, noise limitations may arise. The noise rate per supermodule estimated from the specific noise  $n$  is

$$R = n \cdot A = \underbrace{0.54 \text{ Hz/cm}^2}_{\text{noise rate}} \cdot \underbrace{3.7 \cdot 2.5 \text{ cm}^2}_{\text{pad area}} \cdot \underbrace{96}_{\text{pads per strip}} \cdot \underbrace{91}_{\text{strips per SM}} = 44 \text{ kHz}. \quad (4.1)$$

This noise rate per supermodule is used here as a input in the calculation of the Fake Trigger Rate (FTR). The accidental coincidence of two supermodules in a time window of 25 ns ( $1/f_{LHC}$ ) is

$$FTR = (R/f_{LHC})^2 \cdot f_{LHC} = 48 \text{ Hz}. \quad (4.2)$$

The FTR for this two-fold coincidence must be multiplied for the number of combinations (both the geometric configurations and the gate width) e.g. in a pure back-to-back geometry the configurations to be considered are nine.

During the commissioning in the ALICE cavern, the rate has been found considerably lower than the one measured in the test beams. This deviation from the test beam data is probably due the different gas fluxing of the MRPC chambers in the cavern environment. The MRPC modules have been under a continuous gas-fluxing of approximately 20 l/h per supermodule since the supermodule installation (last installation April 2008).

The specific noise rate measured in the cavern is  $n \sim 0.075 \text{ Hz/cm}^2$ , it is therefore a factor 8 lower than the expected. Consequently the noise rate per supermodule  $R$  is

$$R = n \cdot A = \underbrace{0.075 \text{ Hz/cm}^2}_{\text{noise rate}} \cdot \underbrace{3.7 \cdot 2.5 \text{ cm}^2}_{\text{pad area}} \cdot \underbrace{96}_{\text{pads per strip}} \cdot \underbrace{91}_{\text{strips per SM}} = 6.1 \text{ kHz} \quad (4.3)$$

---

<sup>1</sup>Purity is defined by the number of valid TPC reconstructed tracks over the total triggers.

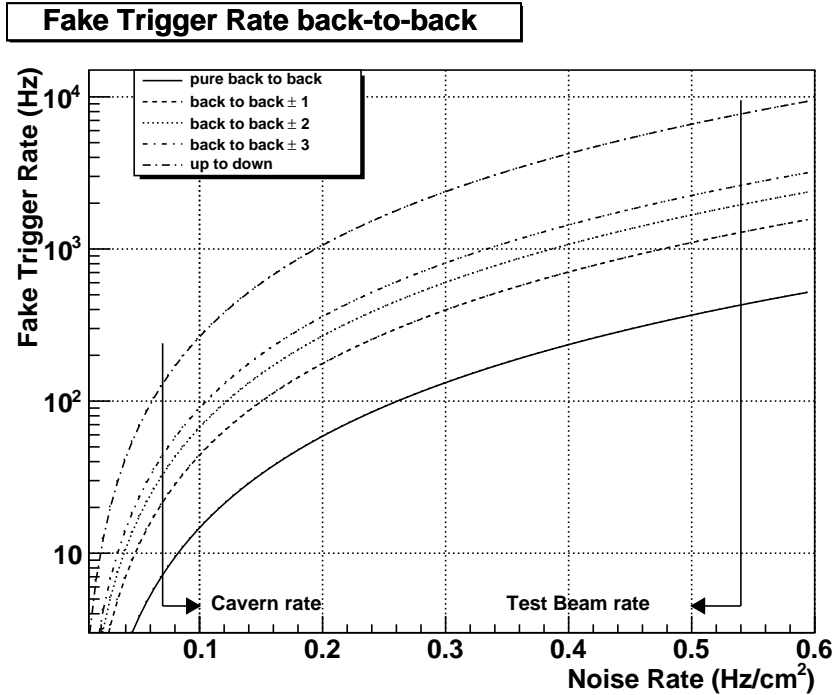


Figure 4.1: Fake trigger rate as a function of the average noise rate in several trigger configurations. “Back-to-back  $\pm k$ ” configuration select events with hits on opposite supermodules and the  $2k$  neighbouring ones with a gate of 25 ns. “Up - down” configuration selects events with a hit in the upper 9 supermodules and one hit in the 9 lower supermodules with a gate of 50 ns.

and the FTR for the two-supermodule coincidence is

$$FTR = (R/f_{LHC})^2 * f_{LHC} = 0.92 \text{ Hz.} \quad (4.4)$$

Fig. 4.1 shows the FTR for different trigger configurations. the FTR is calculated as a function of the specific noise in an ideal geometry.

The FTR scaling between the selection algorithm depends basically on the number of combinations, that are reported in Tab. 4.1

The meaning of the BTB $\pm k$  trigger is shown in the  $k = 3$  case in Fig. 4.2. The trigger is issued when there is a combination of a hit in a supermodule in the upper half and one in the symmetric acceptance window opposite to the upper supermodule and large  $2k + 1$  supermodules. The acceptance window is reduced to 3 supermodules for the S00 and S08 cases to reduce the horizontal configurations, whose signal-to-noise ratio is disfavoured. In all the combinations the gate of the acceptance window is shifted of one LHC cycle to take into account the time of flight of the down-going particle.

Fig. 4.1 also shows the FTR for the up-down algorithm that selects events with one

Table 4.1: Combinations and fake trigger rate for several trigger configurations.

Algorithm	Combinations	FTR (Hz)
Pure BTB	9	8.3
BTB $\pm$ 1 supermodule	27	24.8
BTB $\pm$ 2 supermodules	41	37.6
BTB $\pm$ 3 supermodules	55	50.5
UP-DOWN	162	149

hit in the upper half of the and one hit in the lower half of the TOF in a 50 ns gate. Tab. 4.1 shows the total number of combinations and the FTR expected for the trigger configurations described.

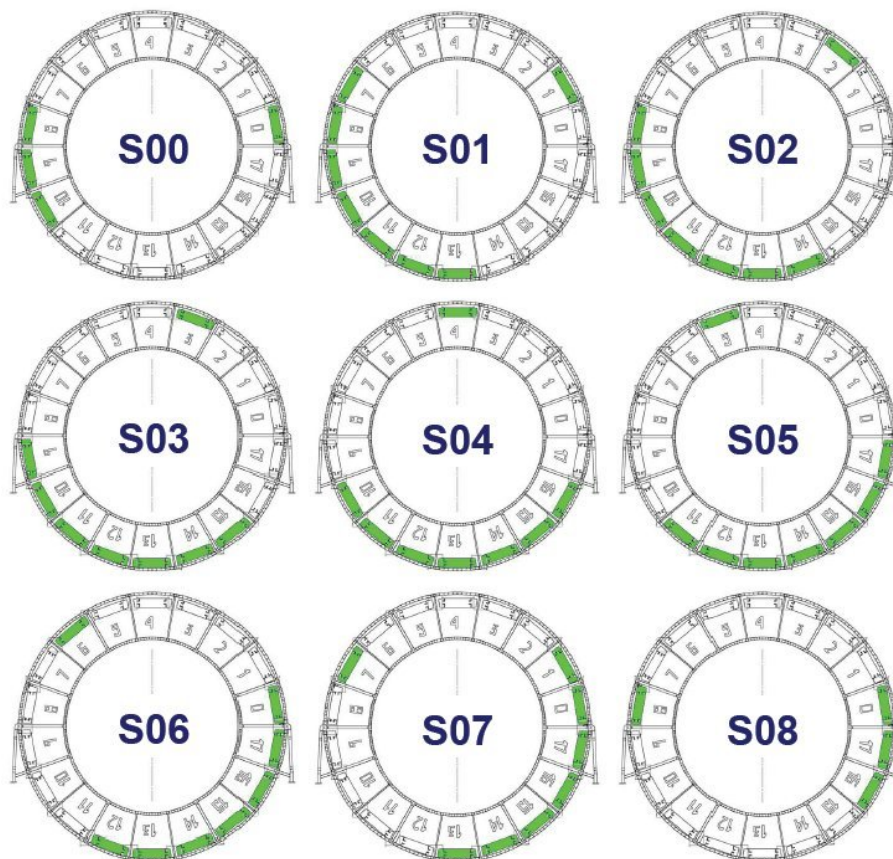


Figure 4.2: The 55 possible combinations in the BTB $\pm$ 3 supermodules trigger algorithm.

**Online purity control.** The calculations presented in the previous paragraph must be controlled on the data read from the detector. This can be done offline with a benchmarking procedure that will be described in §4.1.5.

An online purity-control tool has been developed to monitor the purity of the sample, by simply monitoring an off-gate trigger that is elaborated parallelly to the in-gate trigger.

This off-gate trigger is issued by the CTTM with the same logic of the in-gate

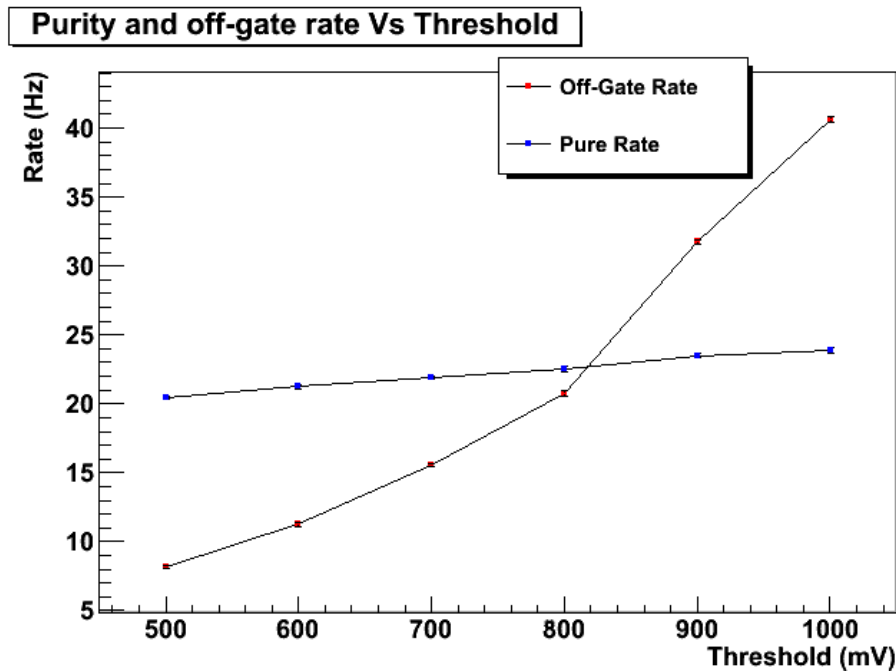


Figure 4.3: Rate of muon candidates and rate of the off-gate trigger as a function of the threshold set by the LTM (higher LTM threshold corresponds to a lower differential threshold) for  $BTB\pm 1$  trigger.

trigger, but the on the opposite window are delayed of 250 ns (10 Clock cycles). The rate of the off-gate trigger is an online estimate of the FTR, since the number of combinations taken into account are the same and there are no time-correlated hits (i.e. muons) in the shifted gate.

The difference between the correct in-gate trigger rate and the off-gate trigger rate is an estimate of the rate of muons selected by the in-gate trigger. Fig. 4.3 shows the rate of muon candidates and the off-gate trigger as a function of the threshold set on the NINO ASICs for the  $BTB\pm 1$  trigger.

As anticipated in §3.3, lower values of the LTM threshold correspond to higher val-

ues of the differential threshold<sup>2</sup>; the off-gate trigger clearly shows a dependence on the threshold, while the muon candidate trigger is almost unaffected by the threshold setting.

**Rate stability.** Trigger rate stability is a consequence of the correct system behavior: if the rate is not stable within statistical fluctuation, then the trigger system suffers from noise bursts in a given point of the trigger chain.

Fig. 4.4(a) shows the trend of the main trigger (BTB $\pm$  3) rate in a 36 hours period. The trend shown in figure is a screenshot from the graphical user interface available for the shifter.

Fig. 4.4(b) shows the distribution of the rate for the same trigger in a different 36 hours period. The rate is calculated using an internal counter of the CTTM that is reset every 30 s. The statistical fluctuation of the trigger rate  $\delta(R)_{stat}$  are therefore

$$\delta(R)_{stat} = \sqrt{R/T}. \quad (4.5)$$

The intrinsic statistical fluctuation from this value are, from Eq. 4.5, 1.76 Hz. The statistical fluctuation accounts for 70% of the  $\sigma$  obtained from the gaussian fit. The main trigger is then stable on long time periods and the fluctuations in the rate are mainly due to statistical fluctuations.

### 4.1.2 Main trigger for the 2009 cosmic run

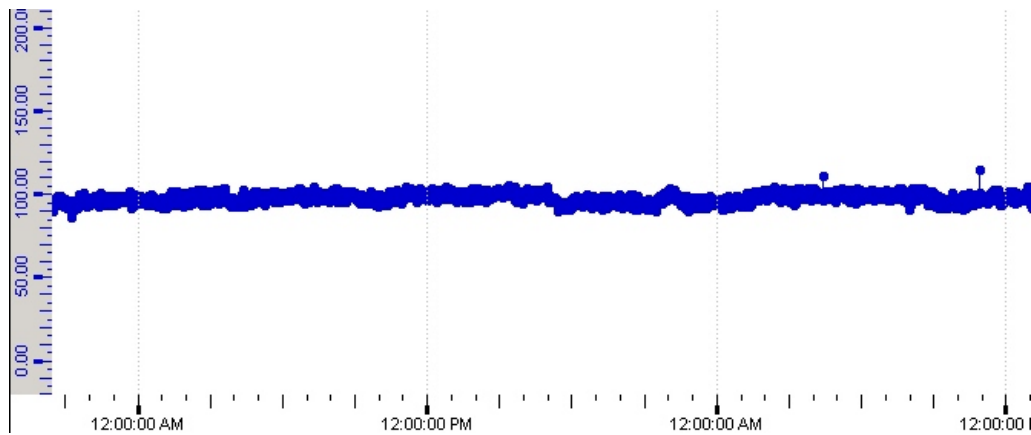
In the first weeks of the 2009 cosmic run, a selection process was performed to identify the best candidate for the main trigger.

As anticipated, the algorithm chosen for the 2009 cosmic ray run was the BTB $\pm$ 3. The Pure BTB was not considered optimal for the TPC calibrations since the algorithm imposes a geometrical cut on the momentum of the particles. More than ten trigger configurations has been tested until the BTB $\pm$ 3 was considered optimal for the low- $p_T$  track calibrations.

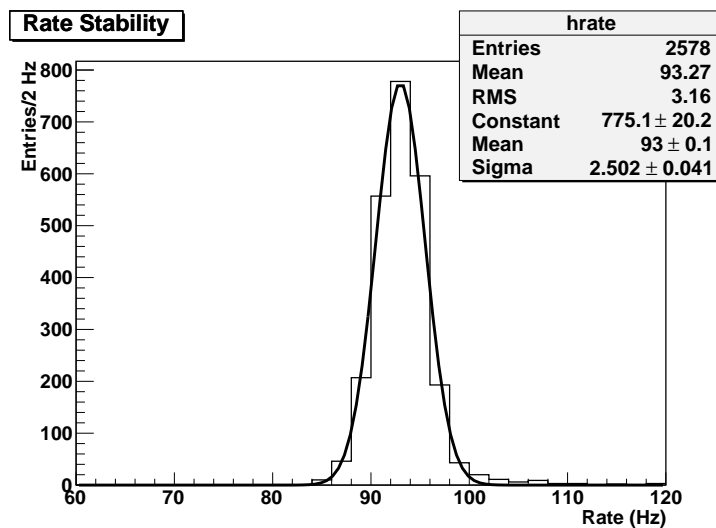
Beside the main trigger several groups of the Collaboration requested additional trigger configurations to facilitate their commissioning activities. The EMCAL group requested a subset of the BTB $\pm$ 3. The ITS group requested a specific subset of the BTB $\pm$ 3 trigger using only the four strips at the center of the supermodules, since the SPD trigger was not available during its cooling plant maintenance.

---

<sup>2</sup>The LTM threshold  $V_{th}$  and the differential threshold on the NINO ASIC  $V_{diff}$  are related by the  $V_{diff} = 0.6 - 0.27 \cdot V_{th}$ . Therefore a higher LTM threshold corresponds to a lower differential threshold.



(a) Rate trend in Hz on a 36 hours period



(b) Rate distribution in a 36 hours period

Figure 4.4: (a): Rate in Hz of the BTB  $\pm 3$  supermodules in a 36 hours period, taken from the graphical user interface of the TOF available for the shifter. (b): Rate distribution for the trigger rate from a different 36 hours period.

### 4.1.3 Cosmic Rays Physics trigger

The Cosmic physics group of the ALICE collaboration requested an additional trigger in order to study multi-muon and photo-nuclear events.

Multi-muon bundles are produced in extensive atmospheric showers at high altitude and arrive almost parallel to shower direction. Photo-nuclear events are inelastic interactions between a high energy muon ( $E > 10$  GeV) and a nucleon.

Photo-nuclear and multi-muon events are triggered by selecting events with multi-

plicity on TOF  $n_{hits} \geq 4$  in a time window of 50 ns. The fake trigger rate expected for this trigger is  $\sim 4$  mHz (Cfr. Fig. 4.9), while the DAQ rate for this trigger class was  $R_{CP} \sim 9$  Hz.

#### 4.1.4 2009 Cosmic Run Statistics

The main goal of the 2009 cosmic run was to collect enough statistic to provide a TPC calibration. The request from TPC group was to collect  $\sim 4 \cdot 10^7$  events in different magnetic field configurations. This main goal can be considered successfully accomplished and the cumulated statistics during 2009 cosmics run is a factor 10 higher.

Besides the main calibration goal, the exercise of a long run was fundamental to tune the detectors for the first collisions.

Table 4.2: Cumulated statistics for 2009 Cosmic run.

period	Statistics
Wk 32-33 detectors warming-up	
Wk 34: L3=0.0T Dipole=0.0T	TOF+TPC+ITS trg: TOF(BTB $\pm$ 3)33Mevents TOF+TPC+ITS trg: SPD 23kevents
Wk 35-36: L3=0.5T / 0.2T Dipole=0.7T	TOF+TPC+ITS++ trg: TOF(BTB $\pm$ 3) 110Mevents TOF+TPC+ITS trg: SPD 27kevents
Wk 37: L3=0.0T Dipole=0.0T	TPC+ITS++ trg: TOF(BTB $\pm$ 3): 165 Mevents
Wk 38/39: Maintenance	
Wk 40-41-42-43-44: L3=0.0T Dipole=0.0T	TOF+TPC+ITS++ trg:TOF(BTB $\pm$ 3) 160Mevents
Total	468 Mevents

#### 4.1.5 Results

In this section some of the results obtained in the 2009 cosmic-run data taking will be introduced.

**Data purity** In order to check the purity of the data collected in the cosmics run, one can consider the quantity  $\tau$  (Fig. 4.5(a)):

$$\tau = t - t_0 - L/c \quad (4.6)$$

where  $t - t_0$  is the Time-Of-Flight,  $L$  is the distance between two hits and  $c$  is the speed of light. In the case of a particle traversing the detector at the speed of light,  $\tau$  should be 0.

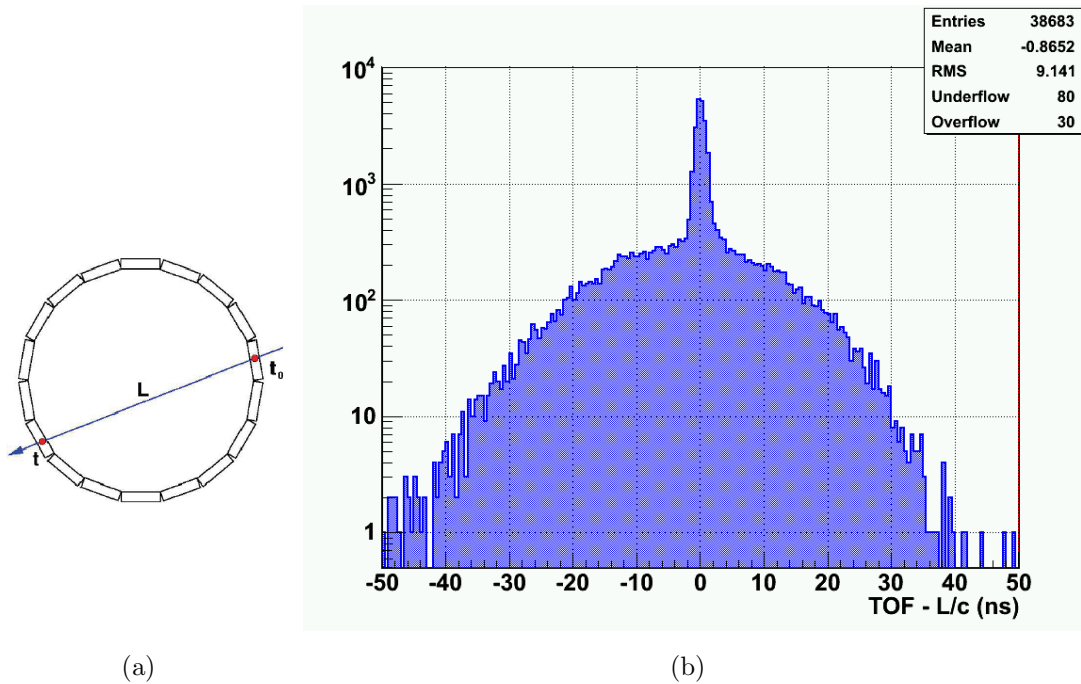


Figure 4.5: (a): Diagram illustrating the TOF- $L/c$  concept. (b): Histogram of TOF- $L/c$  from a cosmic data sample.

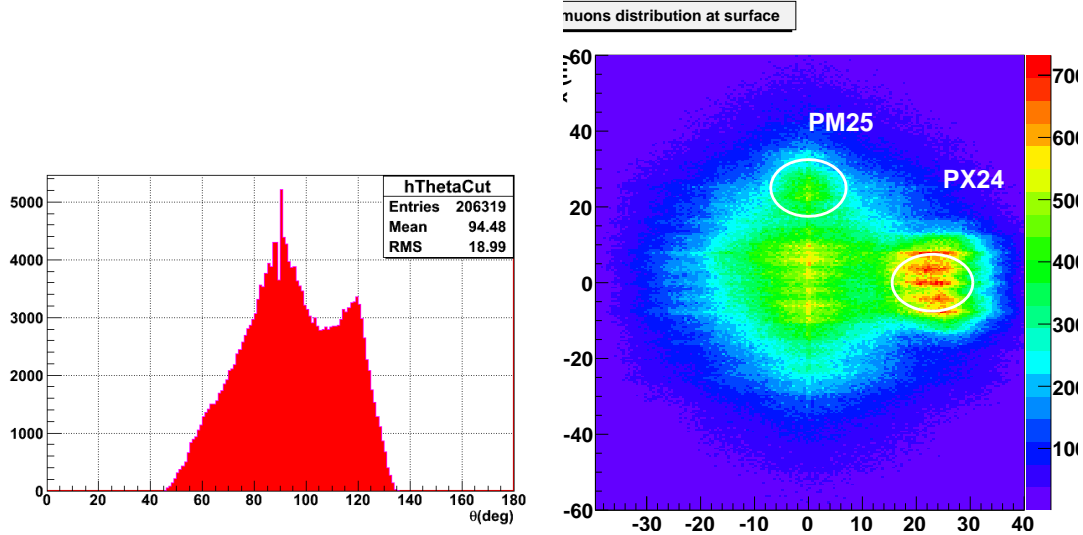
Fig. 4.5(b) shows the  $\tau$  distribution, calculated only from TOF data, without any TPC information. The histogram has a clear central peak over a stochastic background ranging from -50 ns to 50 ns; the hits from the central narrow peak are more than 40% of the total triggers. The online trigger monitor estimate is compatible with the offline, both are consistent with the 45 Hz value of the FTR listed in Tab. 4.1.

**Time Resolution.** The time resolution can be preliminary obtained by fitting the central narrow peak with a gaussian superimposed to the stochastic background. The  $\sigma$  of the gaussian obtained only from the TOF data fit is  $\sigma_\tau = 170ps$ .

The single-hit time resolution is therefore  $\sigma_t = \sigma_\tau/\sqrt{2} = 120 ps$ , which is a remarkable achievement considering the poor time slewing correction<sup>3</sup>, the non-aligned

<sup>3</sup>The optimal time slewing correction requires channel-specific correction parameters. However the selected tracks are sufficient to calibrate all the available channels using a smaller number of

geometry and that no tracking has been applied.



(a)  $\theta$  distribution of muons selected through the cut on  $\tau$ . (b) Surface extrapolation of the tracks selected; the main shaft and service shaft positions have been highlighted in white

Figure 4.6: Angular distribution and surface extrapolation for a cosmic muon sample.

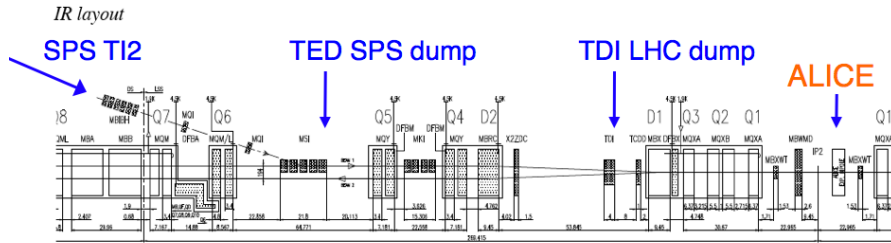
**Angular Distribution.** The large sample of muons from the 2009 cosmic run allows the study of the angular distribution of the down-going muons. Fig. 4.6(a) shows the angular distribution in  $\theta$ , that is the angle with respect to the horizontal axis (i.e.  $z$ ) in the  $yz$  plane<sup>4</sup>, the distribution is centered around the vertical  $\theta = 90^\circ$  and clearly shows an excess around the  $\theta = 120^\circ$  point.

The excess is due to the ALICE access shaft (i.e. PX24 in the LHC naming standard). Fig. 4.6(b) shows the extrapolation of the  $\theta - \phi$  directions to the surface level (i.e. 45 m above the interaction point). The surface extrapolation shows a central peak around the zenith of ALICE and two excess points corresponding roughly to the PM25 service shaft and PX24 access shaft of ALICE.

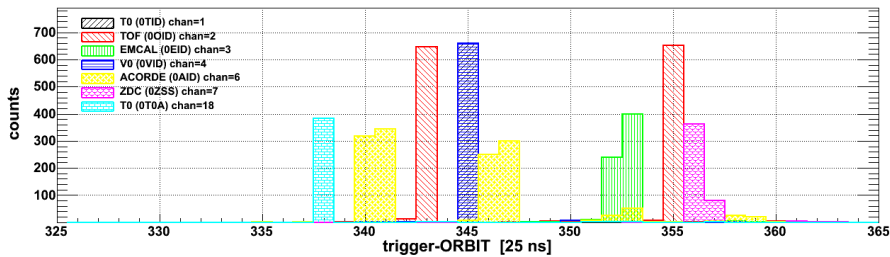
common calibration parameters

<sup>4</sup>In the coordinate system considered here, the origin of the axes is the interaction point (IP), the  $y$  axis is the vertical,  $z$  is the beam axis pointing in the clockwise sense of LHC, and the  $x$  axis is pointing to the geometrical center of the LHC.

## 4.2 Trigger latency tuning with beam dump



(a) .



(b) .

Figure 4.7: (a): Diagram of the beam transfer line from SPS to LHC in the sector 2, beam dumps are highlighted. (b): Time distributions of the hits during a TED beam dump.

As already mentioned in §2.5.1 the latency of the trigger inputs must be aligned in time by the CTP in such a way that, the trigger is issued with a common latency independent from the triggering detector.

The particles generated synchronously during a beam dump provided a common timing reference to align the triggers before the collisions (this is possible only for the ALICE and the LHCb experiments). Fig. 4.7(a) shows the schematics of the transfer line in the LHC sector 2.

The trigger latency is for the TOF an issue that is discussed in §3.8. Fig. 4.7(b) shows the input time expressed as bunchId with respect to the LHC ORBIT<sup>5</sup>. The TOF trigger is now time aligned in the CTP, since TOF triggers are issued within the L0 latency. Despite the distance from the interaction point TOF trigger is issued before triggers from detectors closer to the interaction point (i.e. V0, SPD).

<sup>5</sup> The LHC ORBIT is a signal issued every full orbit of LHC, i.e. every 3564 LHC clock cycles.

### 4.3 Ultra peripheral collisions

An ultra-peripheral collision (UPC) between two charged particles is the interaction between the virtual photon clouds surrounding the charged particle. Since the intensity of the electromagnetic field and the density of the photon cloud is proportional to  $Z^2$ , this kind of processes is highly favored in an heavy ion collider. The impact parameter is larger than the radius of the nuclei and the interaction occurs between quasi-real photons. The specific case here examined is the production of vector mesons production ( $\rho$ ,  $J/\Psi$ ).

The STAR experiment at the RHIC make use of a dedicated trigger detector (Central Trigger Barrel) to select events with “two back-to-back tracks in an otherwise empty detector” to select exclusive  $\gamma\gamma \rightarrow^{UPC} \rho \rightarrow \pi^+\pi^-$  production [Bal08]. The selection of this specific topology can be carried out by the TOF trigger system at an L0 level. In this section, the production rates and contamination for the UPC selection of  $\rho$  and  $J/\Psi$  are described .

Labeling the decay products of the  $\rho$  and  $J/\psi$  as “back-to-back” is misleading with respect to the definitions given in the previous sections. The topology of the decay is represented in Fig. 4.8(b) and Fig. 4.8(a). Due to the magnetic field the two tracks are bent and reach TOF with an angle  $\theta$ . The distribution of the angle  $\theta$  is shown in Fig. 4.8(c) obtained with a Monte Carlo simulation using the STARlight event generator. The topology selected in these cases is one hit on a supermodule and one hit on a window centered in  $\theta = 80^\circ$  for  $\rho$  and centered in  $\theta = 160^\circ$  for the  $J/\Psi$

$\boxed{\gamma\gamma \rightarrow^{UPC} \rho \rightarrow \pi^+\pi^-}$ : The cross section for  $\gamma\gamma \rightarrow^{UPC} \rho$  process is relatively large (i.e. 5200 mb)[Bal08], however the probability of the detection of both pions  $\epsilon^{cont}$  is rather low (i.e. 8.3%) since the longitudinal momentum of the  $\rho$  can be as large as 6 GeV/c. Considering the window of 2 supermodules for the “back-to-back” decay product, the trigger efficiency is 60%. Therefore the rate expected is

$$R^{(UPC} \rho \rightarrow \pi\pi) = \mathcal{L} \cdot \sigma \cdot \epsilon^{cont} \cdot \epsilon^\rho = 10^{27} \text{ cm}^{-2}\text{s}^{-1} \cdot 5200 \text{ mb} \cdot 0.083 \cdot 0.6 = 259 \text{ Hz} \quad (4.7)$$

while the fake trigger rate expected for TOF is

$$FTR = \frac{N_{comb} R^2 \delta}{f_{LHC}} = 2 \cdot 18 \cdot (6.1 \text{ kHz})^2 \cdot 0.2/40 \text{ MHz} = 6.7 \text{ Hz} \quad (4.8)$$

where  $R$  is the noise rate per supermodule with 0.07 Hz/cm<sup>2</sup>,  $N_{comb}$  is the number of combinations and  $\delta$  is the noise suppression factor when vetoing the trigger in the clock cycles with no bunch crossing (i.e.  $f_{coll}$  for the ions is 125 ns). This selection algorithm is able to select at L0 an UPC production of  $\rho$  with a purity of 97%.

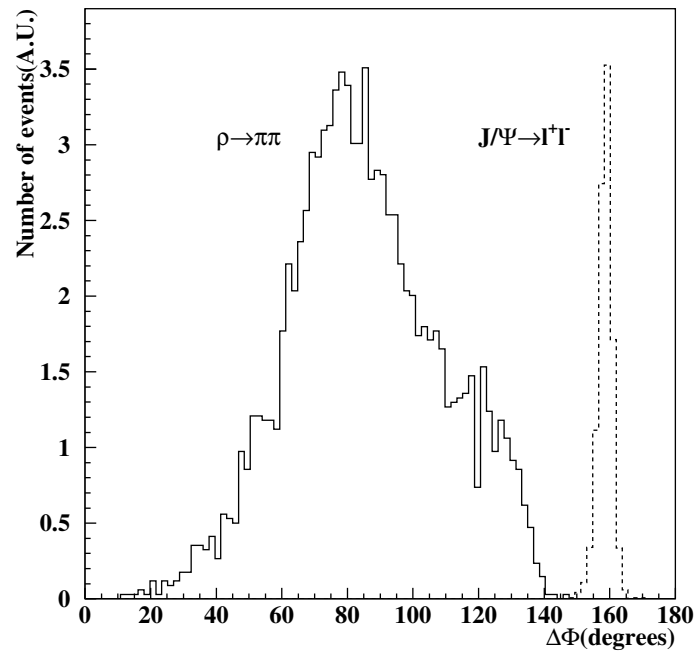
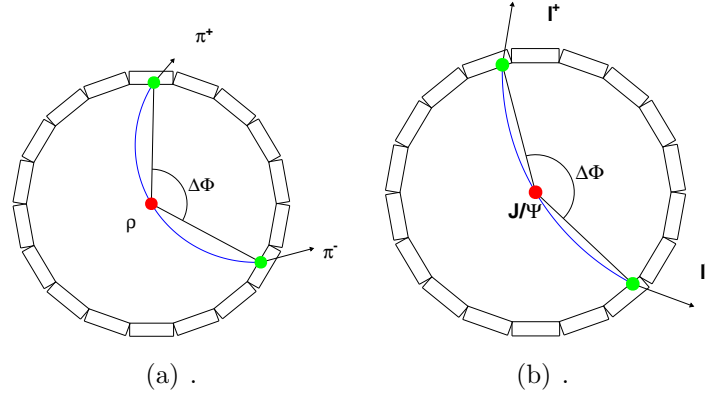


Figure 4.8: (a),(b): Decay topology for  $\rho \rightarrow \pi^+\pi^-$  and  $J/\Psi \rightarrow l^+l^-$  respectively. (c): Distribution of  $\theta$  for the  $\rho$  and the  $J/\psi$  case obtained through a Monte Carlo simulation

$\boxed{\gamma\gamma \rightarrow^{UPC} J/\Psi \rightarrow l^+l^-}$ : The cross section for this process is smaller with respect to the previous one, however the acceptance (17.6%) and efficiency (94%) are higher and the trigger window can be of one supermodule. The expected production rate is

$$R(\gamma\gamma \rightarrow^{UPC} J/\Psi \rightarrow l^+l^-) = \mathcal{L} \cdot \sigma \cdot \epsilon^{cont} \cdot \epsilon^{J/\Psi} = 10^{27} \text{ cm}^{-2}\text{s}^{-1} \cdot 32 \text{ mb} \cdot 0.176 \cdot 0.94 = 0.64 \text{ Hz} \quad (4.9)$$

The FTR is considerably smaller

$$FTR = \frac{N_{comb} R^2 \delta}{f_{LHC}} = 18 \cdot (6.1\text{kHz})^2 0.2 / 40\text{MHz} = 3.3 \text{ Hz}. \quad (4.10)$$

The sample selected at L0 with a total rate of 3.94 Hz has a purity of 16%. The purity of the sample can be improved if the TRD detector can provide the  $e^+e^-$  identification within L1 latency, thus selecting the  $e^+e^-$  decay case.

#### 4.4 $pp$ Minimum bias

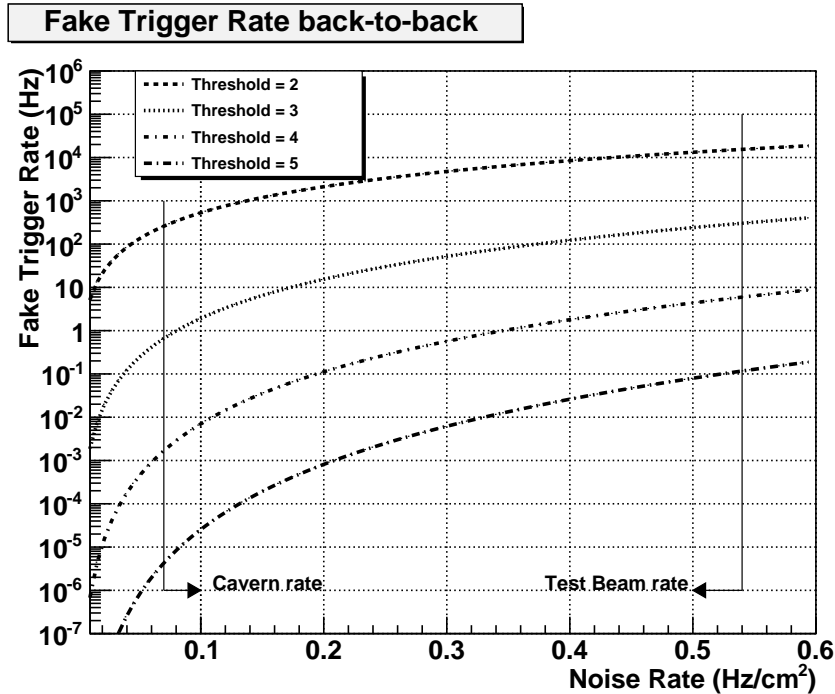


Figure 4.9: Fake trigger rate for several MB thresholds on TOF with a gate of 25 ns.

The  $pp$  minimum bias (MB) is defined as the minimal criteria that trigger data acquisition. The minimal criterion in the case of TOF MB trigger is the minimum number of fired channels in the CTTM.

The selection of a small number of hits is susceptible of a considerable fake trigger rate for a detector with a large area such as the TOF. Fig. 4.9 shows the FTR for several thresholds on global multiplicity.

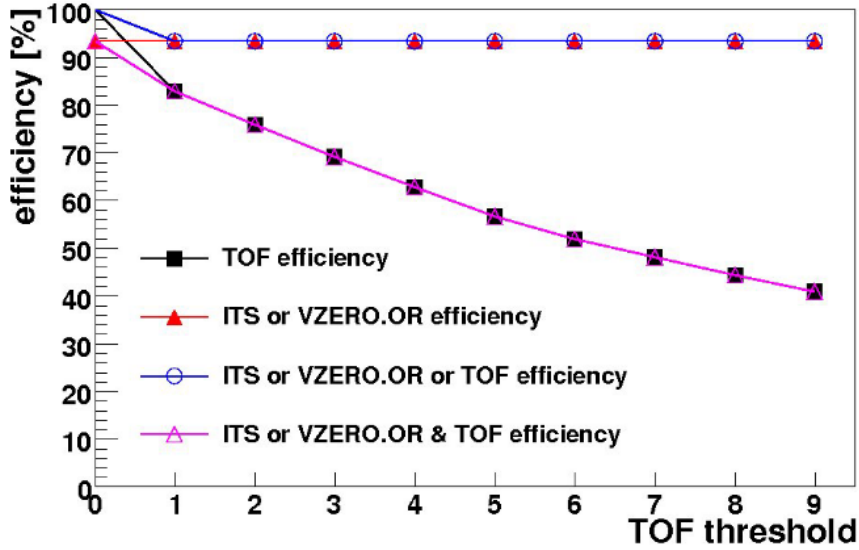


Figure 4.10: Efficiency for several MB trigger configurations on CTP.

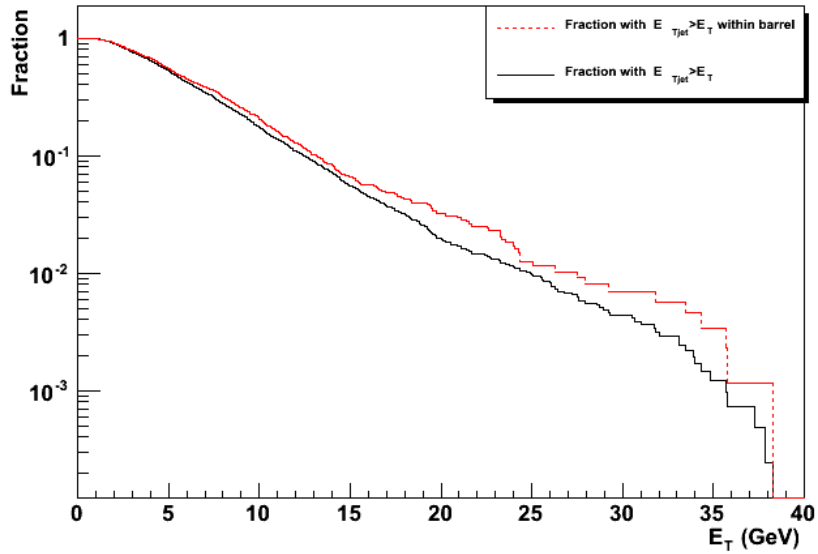
To study the efficiency of the TOF MB trigger in several threshold configurations a Monte Carlo calculation has been performed. Fig. 4.10 shows the MB efficiency calculated through  $10^4$  PYTHIA MB Events. The efficiency for MB is considerably lower (i.e.  $\epsilon \sim 70\%$ ) with respect of the ITS (SPD) trigger, since the TOF is located at 3.7 m from the beam axis.

This simple calculation shows that, despite the limitations, the TOF trigger system can provide a backup trigger for the ITS.

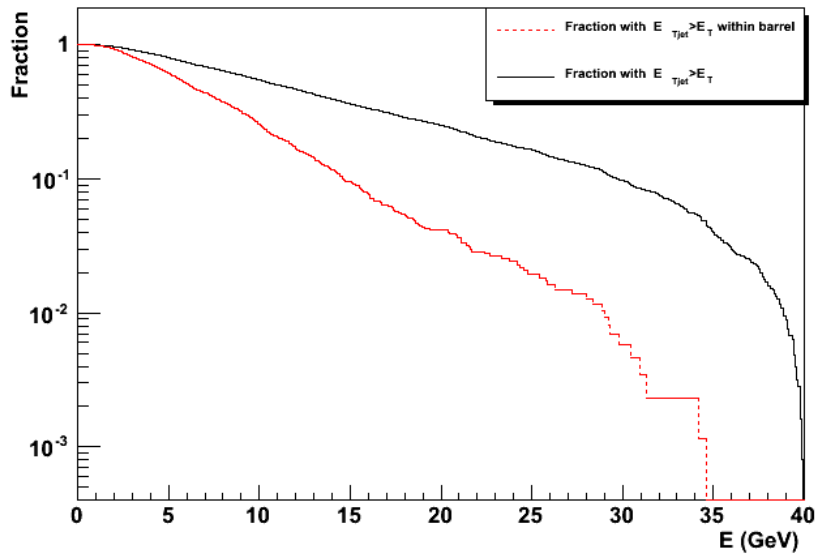
## 4.5 Jet trigger study

Jet physics is a topic of interest both for heavy-ion oriented studies and  $pp$  physics. In the case of a heavy ion collision the possibility to identify a jet with the TOF is ruled out by the large charged multiplicity. In  $pp$  collisions the expected multiplicity is much lower, therefore a TOF trigger on jets can be foreseen.

The barrel geometry of the TOF can introduce a bias in the selected sample. A Monte Carlo simulation has been carried out using  $10^5$  PYTHIA events simulated with Aliroot for  $pp$  collisions at 14 TeV. Fig. 4.11(b) shows the fraction of jets with energy higher than  $E(\text{GeV})$  for all the generated jets (solid line) and the jets with  $|\eta| < 1$  (dashed line). The barrel geometry therefore introduces a significant bias when considering the total energy. For the transverse energy the bias is considerably



(a)



(b)

Figure 4.11: (a): Fraction of events with  $E_T(jet) > E_T$ . (b): Fraction of events with  $E(jet) > E$ .

lower: Fig. 4.11(a) shows the fraction of jets with transverse energy higher than  $E_T(GeV)$  for all the jets (solid line) and the jets in the barrel acceptance (dashed

line).

### 4.5.1 Topological jet selection

Most jet selection algorithms are elaborated through the use of calorimetric information. In the TOF trigger system, and more generally in ALICE there is no hadronic calorimetric information.

The localized structure of a jet suggests the development of a topological trigger based on the  $\eta - \phi$  correlations in the structure of a jet.

Even if the initial particles have a strong  $\eta - \phi$  correlation, this information is “shuffled” during the event evolution (e.g magnetic field, particle decays and multiple scattering). A baseline study of the  $\eta - \phi$  correlations in jet events at TOF level is here reported. Fig. 4.12(a) shows the correlation histogram<sup>6</sup> of the distance  $r$  ( $r^2 = \eta^2 + \phi^2$ ) for a Monte Carlo sample (red line) and for a completely random generated sample (black line). The random sample has been generated with the same multiplicity distribution of the Monte Carlo sample with hits uniformly generated in  $\eta$  and  $\phi$ .

The correlation patterns differ significantly for small  $r$ . Fig. 4.12(b) shows the differences  $(n_{MC} - n_{random})/n_{random}$  as a function of  $r$ .

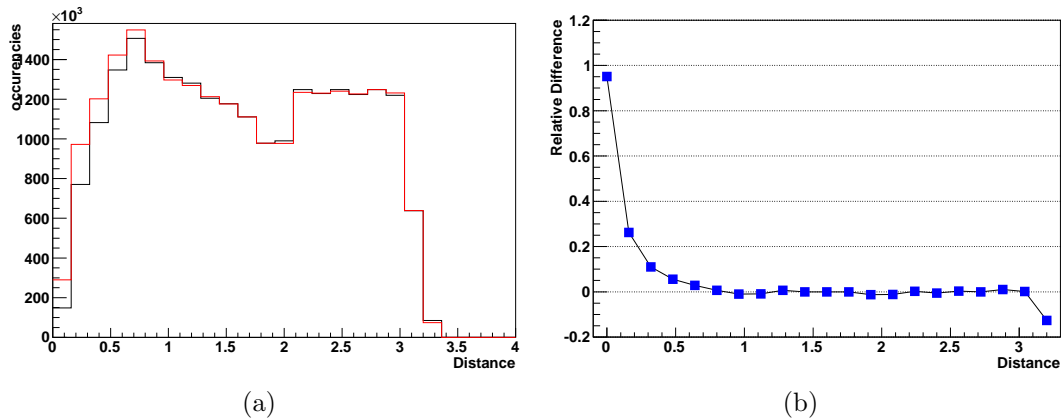


Figure 4.12: (a): Correlation in distance  $r$  with  $r^2 = \eta^2 + \phi^2$  for a completely random generated sample and for a Monte Carlo sample. (b): Relative difference in the samples.

<sup>6</sup>The correlation histogram is the distribution of the distances between each pair of hits within an event.

### 4.5.2 Multiplicity jet selection

Despite the topological content may be emphasized, the satisfactory clustering algorithm at trigger level is yet to be identified; a simpler trigger algorithm can be studied on a global multiplicity basis.

The CDF collaboration has extensively studied the properties of jets in  $p\bar{p}$  collisions [Aff02] in  $|\eta| < 1$ . In minimum-bias data, they observed that the number of charged particles produced in a jet fragmentation depends on the energy of the jet.

In the Monte Carlo simulation for pp collisions at 14 TeV, the global multiplicity on TOF shows a dependence on the jet transverse momentum. Fig. 4.13 shows the scatter plot of the leading jet<sup>7</sup> transverse momentum versus global multiplicity on TOF.

From this simple Monte Carlo calculation, it is possible to derive that a trigger algorithm based on a global multiplicity on TOF  $n_{ch} \geq 20$  has an efficiency of 55% on jets with leading jet transverse momentum  $p_T > 2$  GeV/c with 0.5% contamination.

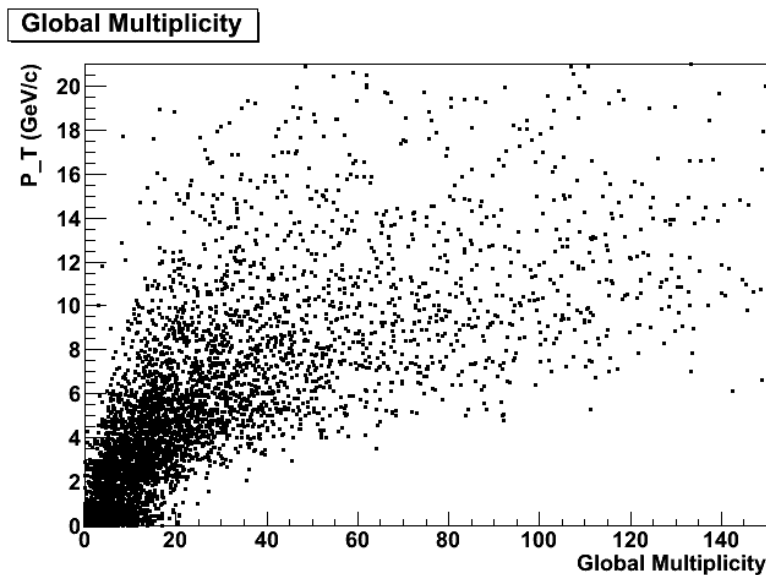


Figure 4.13: Scatter plot of the leading jet transverse momentum versus global multiplicity on TOF.

<sup>7</sup>The leading jet is the jet with the highest the transverse momentum in an event.

# Conclusions

In this thesis work the Time-Of-Flight detector of the ALICE experiment has been presented with particular attention to the trigger system.

The trigger system has shown its capabilities in the 2009 Cosmic run with more than  $4 \cdot 10^8$  collected events and with a 40% purity. Using the data collected in this long run, it was possible to calibrate the ALICE tracking systems and to debug the detector in preparation for the first collisions.

This work was made possible by several hardware and firmware conditions/features:

- the noise rate of the FEE is a factor 8 lower than what expected from the commissioning phase, probably due to a better gas conditioning of the MRPC strips;
- the absence of electronic noise in the trigger electronic chain;
- the signals from the TOF detector are aligned within  $\pm 1$  ns, a clock and TTC time-alignment campaign was carried out for this purpose;
- the possibility to modify the CTTM firmware without hardware intervention in the cavern. This particular feature helped to test more than ten trigger configurations and to identify the optimal one;

Thanks to the relatively low noise of the MRPC strips, the TOF trigger system can provide:

- a back-up trigger for minimum bias events.
- ultraperipheral event selection in Pb-Pb collisions by selecting the  $\rho$  and  $J/\Psi$  with an expected sample purity higher than the first estimate [PPR06].
- A multiplicity event selection of jets within Level 0 latency.

This thesis work shows how the TOF trigger system ensures maximum flexibility in the development of the selection algorithms and is therefore prepared to cope with the unexpected physics that the LHC will explore.



# Bibliography

- [Acc02] A. Accardi, arXiv:hep-ph/0212148.
- [Ada03] D. Adamova et al. [CERES/NA45 Collaboration], *Enhanced production of low-mass electron pairs in 40-A-GeV Pb Au collisions at the CERN SPS*, Phys. Rev. Lett. **91**, 042301 (2003).
- [Ada04] J. Adams et al., STAR Collaboration, Phys. Rev. Lett. **92** (2004) 062301.
- [Aff02] T. Affolder et al, CDF Collaboration, Phys. Rev. D **65** (2002) 092002
- [Aga05] G. Agakichiev et al., CERES Collaboration, Eur. Phys. J C **41** (2005) 475.
- [Ait04] Aitchison, I. J. R. and Hey, A.J.G. (2004) *Gauge Theories in Particle Physics* voll. 1 e 2. Institute of Physics Publishing, Bristol.
- [Aki03] A. Akindinov et al., *Space charge limited avalanche growth in Multigap Resistive Plate Chambers*, EPJdirect **A1**, (2003) 1-11.
- [Aki04] A. Akindinov et al., *Operation of the multigap resistive plate chamber using a gas mixture free of flammable components*, Nucl. Instrum. Meth. A **532**, (2004) 562.
- [Aki04a] A. Akindinov et al. [ALICE TOF Collaboration], *Particle identification with the ALICE TOF detector at very high particle multiplicity*, Eur. Phys. J. C **32S1**, (2004) 165.
- [Aki04b] A. Akindinov et al., *Study of gas mixtures and ageing of the multigap resistive plate chamber used for the Alice TOF*, Nucl. Instrum. Meth. A **533**, (2004) 93.
- [Aki04c] A. Akindinov et al., *Design aspects and prototype test of a very precise TDC system implemented for the Multigap RPC of the ALICE TOF*, Nucl. Instrum. Meth. A **533**, (2004) 178.

- [Aki04d] A. Akindinov et al., *Latest results on the performance of the multigap resistive plate chamber used for the ALICE TOF*, Nucl. Instrum. Meth. A **533**, (2004) 74.
- [Aki04e] A. V. Akindinov et al., *Results from a large sample of MRPC-strip prototypes for the ALICE TOF detector*, Nucl. Instrum. Meth. A **532**, (2004) 611.
- [Aki05] A. Akindinov et al., *Scintillator counter with MRS APD light readout*, Nucl. Instr. Meth. A **539**(2005) 172–176.
- [Aki06] A. Akindinov et al., *Study of QGP signatures with the  $\phi$ - $\eta$   $K+K^-$  signal in Pb-Pb ALICE events*, Eur. Phys. J. C **45**, 669 (2006).
- [Aki08] A. Akindinov et al., *Latest results from a mass-production sample of MRPCs for the ALICE TOF detector*, Proceedings of the 10th ICATPP 2007, (2008).
- [Aki09] A. Akindinov et al., *Final test of the MRPC production for the ALICE TOF detector*, Nucl. Instrum. Meth. A **602**, (2009) 709.
- [Ale05] B. Alessandro et al., NA50 Collaboration, Eur. Phys. J C**39** (2005) 335.
- [Ali05] A. Alici, *Realizzazione dei sistemi di qualità nella costruzione dei rivelatori basati sulle MRPC (Multigap Resistive Plate Chamber) per il sistema di Tempo di Volo (TOF) dell'esperimento ALICE ad LHC*, Tesi di Dottorato, Ciclo XVII, Univ. di Bologna.
- [Ang04] F. Anghinolfi, P. Jarron, A.N. Martemiyarov, E. Usenko, H. Wenninger, M.C.S. Williams and A. Zichichi, *NINO: an Ultra-Fast and Low-Power Front-End Amplifier/Discriminator ASIC Designed for the Multigap Resistive Plate Chamber*, Nucl. Instr. Meth. in Phys. Res. A **533**(2004) 183–187.
- [AN370] Altera Corporation, application note 370 <http://www.altera.com/literature/an/an370.pdf>, (2009)
- [Ant03] P. Antonioli and S. Meneghini, *A 20 ps TDC readout module for the ALICE Time of Flight system: design and test results*, Proceedings of 9th Workshop on electronics for LHC Experiments, 29 September - 3 October 2003, Amsterdam, CERN-LHCC-2003-055 (2003), p. 311-315.
- [Ant04] P. Antonioli and S. Meneghini, *Radiation tolerance tests for key components of the ALICE TOF Tdc Readout Module*, Proceedings of 10th Workshop on electronics for LHC and Future Experiments, Boston, 13-19 September 2004, CERN-LHCC-2004-030, (2004), p. 184-188.

- [Ant79] D. Antreasyan et al., Phys. Rev. D **19** (1979) 764.
- [Arn00] NA50 collaboration, *Evidence for Deconfinement of quarks and gluons from the  $J/\psi$  Suppression Pattern measured in Pb–Pb collision at the CERN–SPS*, Phys. Lett. B **477**(2000) 28–36.
- [Arn07] R. Arnaldi et al.,  *$J/\psi$  suppression in In-In collisions at 158 GeV/nucleon* Nucl. Phys. A**783** (2007), 261
- [ATP95] Alice Collaboration, *ALICE, Technical Proposal for A Large Ion Collider Experiment at CERN LHC*, CERN/LHCC/95-71 LHCC/P3, 1995
- [Bac05] B.B. Bach et al., PHOBOS Collaboration, Nucl. Phys. A**757** (2005) 28-101.
- [Bal08] A.J. Baltz et al., *The physics of ultraperipheral collisions at the LHC*, Physics Reports 458 (2008) 1-171.
- [Bas81] M. Basile et a., Nuovo Cimento Soc. Ital. Fis. **65A**, 421 (1981).
- [Bha05] R. S. Bhalerao et al., Phys. Rev. Lett. B627 (2005) 49.
- [Bjo83] J.D. Bjorken, *Highly relativistic nucleus-nucleus collisions: the central rapidity region*. Phys. Rev. D **27** (1983) 140-151
- [Bor01] N. Borghini, P.M. Dinh and J.Y. Ollitrault, Phys. Rev. C 63(2001) 054906.
- [Bor06] N. Borghini, J.Y. Ollitrault, Phys. Lett. B642 (2006) 227, [arXiv:nucl-th/0506045].
- [Bou] L. Bourhis, M. Fontannaz and J. P. Guillet, Eur. Phys. J. C2 (1998) 529-537.
- [Bro91] G.E. Brown and M. Rho, Phys. Rev. Lett. 66 (1991) 2720.
- [CER00] CERN press release 2000,  
  
<http://press.web.cern.ch/press/PressReleases/Releases2000/PR01.00EquarkGluonMatter.html>
- [Cer96] E. Cerron Zeballos, I. Crotty, D. Hatzifotiadou, J. Lamas Valverde, S. Neupane, M.C.S. Williams and A. Zichichi, *A New Type of Resistive Plate Chamber: the Multigap RPC*, Nucl. Instr. Meth. A **374**(1996) 132-135.
- [Chr00] J. Christiansen et al., *A data driven high resolution Time-to-Digital Converter*, Proceedings of the 6th Workshop on Electronics for LHC Experiments, September 2000.

- [Cro75] J.W. Cronin *et al.*, Phys. Rev. **D11** 3105 (1975).
- [CSTDR]  
<https://edms.cern.ch/document/456354/>
- [DAQ99] CERN ALICE DAQ Group, ALICE DATE User's Guide – DATE V3.5, ALICE/99–46, Internal Note DAQ
- [Dia05] A. Dainese, *Charm Quenching in Heavy-Ion Collisions at the LHC*, arXiv:hep-ph/0501292, 31–01–2005.
- [Eji04] S. Ejiri *et al.*, Prog. Theor. Phys. Suppl. **153** (2004) 118.
- [EMCTDR]  
[http://aliceinfo.cern.ch/static/Documents/EMCAL/TDR/All/alice\\_emcal.pdf](http://aliceinfo.cern.ch/static/Documents/EMCAL/TDR/All/alice_emcal.pdf)
- [Esk00] K. J. Eskola, P. V. Ruuskanen, S. S. Rasanen, K. Tuominen, Nucl. Phys. B **570** (2000) 379.
- [Fac04] P. Fachini, *Resonance Production*, J. Phys. G **30**, (2004) S735–S742.
- [FDTDR]  
<https://edms.cern.ch/document/498253/>
- [Fod04] Z. Fodorn, S.D. Katz, JHEP 0404 (2004) 50.
- [Foe09] A. Förster for the NA60 Collaboration, *Proceedings of the “Strangeness in Quark Matter 2006 (SQM2006)”* conference, arXiv:nucl-ex/0609039.
- [Fri05] R.J. Fries, B. Muller, C. Nonaka and S.A. Bass, Phys. Rev. Lett. **90** (2003) 202303.
- [Gla70] R.J. Glauber and G. Matthiae, Nucl. Phys. **B21** (1970) 135.
- [Gre03] V. Greco, C.M. Ko, P. Levai, Phys. Rev. Lett. **90** (2003) 202302.
- [Hag83] R. Hagedorn, Riv. Nuovo Cimento **6** (1983) 1.
- [Hei00] U. Heinz, M. Jacob, nucl-th/0002042, 16/02/2000.
- [Hei04] U. Heinz, [arXiv:hep-ph/0407360].
- [Hir05] T. Hirano, U.W. Heinz, D. Kharzeev, R. Lacey and Y. Nara, arXiv:nucl-th/0511046.

- [Huo03] P. Huovinen, [arXiv:nucl-th:/0305064].
- [Hwa04] R.C. Hwa, C.B. Yang, Phys. Rev. C **70** (2004) 024905.
- [ITSTDR]  
<https://edms.cern.ch/document/398932/>
- [Itz87] Itzykson C. and Zuber J. B., (1987) *Quantum Field Theory*, Mc Graw-Hill, Singapore.
- [Kar02] F. Karsch, *Lattice QCD at High Temperature and Density*, Lect. Notes Phys. **583** (2002) 209–249.
- [Kar022] F. Karsch, Lecture Notes in Phys. (Springer) **583** (2002) 209.
- [Kar06] F. Karsch,[arXiv:hep-ph/061002].
- [Kie99] W. Kienzle et al., TOTEM Collaboration, TOTEM, Total Cross Section, Elastic Scattering and Diffraction Dissociation at the LHC, Technical Proposal, CERN-LHCC-99-007, LHCC-P-5 (1999).
- [Kol00] P.F. Kolb, J. Sollfrank and U.W. Heinz, Phys. Rev. C **62** (2000) 054909.
- [Kol03] P. Kolb and U. Heinz,[arXiv:nucl-th:/0305084].
- [Kol90] E. Kolb and M.S. Turner, *The Early Universe* (Addison–wesley, Redwood City, 1990).
- [Lee03] M. van Leeuwen, for the NA49 collaboration, Nucl.Phys. A**715** (2003) 161, [arXiv: nucl-ex/0208014].
- [Lee90] K.S. Lee, U. Heinz, E. Schnedermann, Z. Phys. **C48** (1990) 525.
- [Len08] M. Lenti et al., *Construction and test of a RICH prototype the NA62 experiment*, Nucl. Instr. Meth. A **593** (2008) 314-318.
- [Leo94] W. R. Leo, *Techniques for Nuclear and Particle Physics Experiments*, Springer-Verlag 1994.
- [Man02] A. Mangiarotti and A. Gobbi, *On the Physical Origin of Tail in the Time Response of Spark Counters*, Nucl. Instr. Meth. in Phys. Res. A **482**(2002) 192–215.
- [Mat86] T. Matsui and H. Satz, Phys. Lett. **B178** (1986) 416.

- [McL01] For a review see L. McLerran *The Color Glass Condensate and Small  $x$  Physics*; 4 Lectures, arXiv:hep-ph/0104285v2.
- [Mor02] A. Morsch and B. Pastirčák, ALICE radiation levels, ALICE-INT-2002-028. A. Morsch and I. Pshenichnov, LHC experimental conditions, ALICE-INT-2002-034.
- [MUOTDR]  
<http://aliceinfo.cern.ch/Collaboration/Documents/TDR/tdr2-main.pdf>  
<https://edms.cern.ch/document/470838/>
- [N3484] NA34 collaboration, *Study of high-energy densities over extended nuclear volumes via nucleus-nucleus collisions at the SPS*, Research proposal CERN-SPSC-84-43 (June 1984)
- [Nag06] J. L. Nagle, Eur. Phys. J. C **49** (2007) 275 [arXiv:nucl-th/0608070].
- [Nan61] Y. Nambu and G. Jona-Lasinio, *Dynamical Model of Elementary Particles Based on an Analogy with Superconductivity*, Phys. Rev. **122**, 345 (1961); **124**, 246(1961).
- [Nar05] M. Nardi, J. Phys. Conf. Ser. 5 (2005) 148.
- [Nyi02] Ágnes Nyíri, *Neutron stars with and without strange matter core*, J.Phys. G:Nucl.Part.Phys. **28** (2002) 2073-2077
- [OFFTDR]  
[http://aliceinfo.cern.ch/static/Documents/TDR/Computing/All/alice\\_computing.pdf](http://aliceinfo.cern.ch/static/Documents/TDR/Computing/All/alice_computing.pdf)
- [Oll97] J.Y. Ollitrault, arXiv:nucl-ex/9711003.
- [PHE02] PHENIX collaboration, *Measurement of Single Electrons and Implications for Charm Production in Au–Au Collisions at  $\sqrt{s_{NN}} = 130$  GeV*, Phys. Rev. Lett. **88**, (2002).
- [PHE03] PHENIX collaboration, *Suppressed  $\pi^0$  Production at Large Transverse Momentum in Central Au+Au Collisions at  $\sqrt{s_{NN}} = 200$  GeV*, Phys. Rev. Lett. **91**, 072301 (2003).
- [PHE04] PHENIX collaboration, *High- $p_T$  Charged Hadron Suppression in Au–Au Collisions at  $\sqrt{s_{NN}} = 200$  GeV*, Phys. Rev. C **69**, 034910 (2004).

- [PHE05] PHENIX Collaboration, *Formation of dense partonic matter in relativistic nucleus-nucleus collisions at RHIC: Experimental evaluation by the PHENIX collaboration*, Nucl. Phys. A **757** (2005) 184, arXiv:nucl-ex/0410003 .
- [PHOSTDR]  
<https://edms.cern.ch/document/398934/>
- [Pis82] R. D. Pisarski, Phenomenology of the Chiral Phase Transition, Phys. Lett. B **110** (1982) 155.
- [PMDTDR]  
<https://edms.cern.ch/document/398931/>  
<https://edms.cern.ch/document/575585/>
- [PPR06] ALICE Collaboration, *ALICE: Physics Performance Report, Volume II*, J. Phys. G: Nucl. Part. Phys. **32** (2006) 1285–2040.
- [Pre09] R. Preghenella, *The Time-Of-Flight detector of ALICE at LHC: construction, test and commissioning with cosmic rays*, Ph.D. Thesis (2009).
- [Raf82] J. Rafelski and B. Muller, *Strangness production in the Quark-Gluon-Plasma*, Phys. Rev. Lett. **48**(1982) 1066.
- [Rap00] R. Rapp, J. Wambach, *Chiral Symmetry Restoration and Dileptons in Relativistic Heavy-Ion Collisions*, Adv.Nucl.Phys. 25 (2000) arXiv:hep-ph/9909229v1
- [RHI05] RHIC collaborations, *Hunting the Quark Gluon Plasma*, BNL-73847-2005, 2005
- [Rie03] W. Riegler, C. Lippmann and R. Veenhof, *Detector Physics and Simulation of Resistive Plate Chambers*, Nucl. Instr. Meth. in Phys. Res. A **500**(2003) 144–162.
- [Rie72] Rieke et al., Phys. Rev. Lett. **A 6**, (1972) 1507.
- [RPP09] S. Eidelman, et al., *Review of particle physics*. Physics Letters **B 592**, (2004) 1.
- [Sat03] H.Satz, Nucl. Phys. **A 715**, (2003) 3.
- [Sca05] E. Scaparrone et al., *A multiplicity trigger based on the Time of Flight detector for the ALICE experiment*, Proceedings of 11th Workshop on electronics for LHC and Future Experiments, Heidelberg, 12-16 September 2005, CERN-LHCC-2005-038, (2005), p. 302-306.

- [Sci04] G. Scioli, Ph.D. thesis, Alma Mater Studiorum - Università di Bologna (2005).
- A multiplicity trigger based on the Time of Flight detector for the ALICE experiment*, Proceedings of 11th Workshop on electronics for LHC and Future Experiments, Heidelberg, 12-16 September 2005, CERN-LHCC-2005-038, (2005), p. 302-306.
- [STA04] STAR collaboration, *Kaon Production and Kaon to Pion Ratio in Au + Au Collisions at  $\sqrt{s_{NN}} = 130$  GeV*, Phys. Rev. Lett. **89**(2004) 143.
- [STA04b] STAR collaboration, *Multi-Strange Baryon Production in Au-Au Collisions at  $\sqrt{s_{NN}} = 130$  GeV*, Phys. Rev. Lett. **92**(2004) 182301.
- [STA04t] STAR Collaboration, *Identified particle distributions in pp and Au+Au collisions at  $\sqrt{s_{NN}} = 200$  GeV*, Phys.Rev.Lett. **92** (2005) 112301, [arXiv:nucl-ex/0310004].
- [STA05] J. Adams et al., STAR Collaboration, Nucl. Phys. A757 (2005) 102-183, [arXiv :nucl-ex/0501009]
- [STA09] B.I. Abelev et al., STAR Collaboration,  *$\rho^0$  Photoproduction in Ultra-Peripheral Relativistic Heavy Ion Collisions with STAR*. LBNL Paper LBNL-2101E. (2009).
- [Tay00] J. R. Taylor, ,, 2000
- [Tec01] Texas Instruments Inc., SN65LVDM1677 Datasheets, (2001).
- [Tec03] Texas Instruments Inc., SN65LVDS348 Datasheets, (2003).
- [Tec09]  
<http://technologytransfer.web.cern.ch/TechnologyTransfer/en/Technology/NINO.html>
- [The01] R. L. Thews, M. Schroedter and J. Rafelski, *Enhanced  $j/\psi$  Production in Deconfined Quark Matter*, Phys. Rev. C **63**, 207 (2001).
- [TOF00] ALICE collaboration, *Time of Flight - Technical Design Report*, CERN/LHCC 2000-12.
- [TOF02] ALICE collaboration, *Time of Flight - Addendum to the Technical Design Report*, CERN/LHCC 2002-016.

[TPCTDR]

<https://edms.cern.ch/document/398930/>

[TRDTDR]

<https://edms.cern.ch/document/398057/>

[Vog91] U. Vogl and W. Weise, *The Nambu and Jona-Lasinio Model: Its Implications for Hadrons and Nuclei*, Prog. Part. Nucl. Phys. **27**, 195 (1991).

[Wan05] X.N. Wang, Phys. Lett. B **595** (2004) 165.

[Wan91] S. Wang et al., Phys. Rev. C **44** (1991) 1091.

[Wan95] X.N. Wang, M. Gyulassy and M. Plümer, Phys. Rev. D **51** (1995) 3436.

[Wei03] W. Weise, [arXiv:nucl-th/0306036].

[Zam06] C. Zampolli, *A study of hadron yields and spectra with ALICE experiment at LHC*, Ph.D. Thesis (2006).

[ZDCTDR]

<https://edms.cern.ch/document/398933/>

[Zic06] A. Zichichi, *Complexity at the fundamental level*, International School of Subnuclear Physics (44th course), Erice 2006, <http://www.ccsem.infn.it/issp2006/>



## Acknowledgements

It would not have been possible to write this Ph. D. thesis without the help of the people around me.

I am most grateful to my supervisor, Prof. Maurizio Basile for the continuous support and patience.

This few lines are not sufficient to express how much I owe to the advice and friendship of Eugenio Scapparone and Pietro Antonioli.

I would like to thank all the physicists that constantly encouraged me during my Ph. D. cycle:

Andrea Alici, Silvia Arcelli, Francesca Bellini, Davide Caffarri, Giovanni Cara Romeo, Prof. Luisa Cifarelli, Annalisa De Caro, Daniele De Gruttola, Barbara Guerzoni, Anselmo Margotti, Rosario Nania, Francesco Noferini, Paola Pagano, Ombretta Pinazza, Roberto Preghenella, Gilda Scioli and Chiara Zampolli.

I acknowledge excellent technical skills of the engineers at INFN Bologna: Daniele Cavazza, Michele Furini, Fernando Massera, Stefano Meneghini, Matteo Rizzi, Stefano Serra, Silvano Zagato, Andrea Zucchini and Mirco Zuffa.

I am most grateful to all the people that granted me the honor of working with them at CERN.

Above all, I would like to thank my parents and my brother for their constant care in these years.

Last, but by no means least, I thank my friends for their encouragement, some of whom have already been named.